UNIVERSIDAD CARLOS III DE MADRID
ESCUELA POLITÉCNICA SUPERIOR

BIOENGINEERING &
AEROSPACE ENGINEERING DEPARTMENT

BACHELOR THESIS

NUMERICAL SIMULATION OF FLOW OVER A FLAPPING AIRFOIL

AEROSPACE ENGINEERING

AUTHOR: Roberto Flores Ridao
TUTOR: Manuel García Villalba

June, 2016

Abstract

This project presents the study of the aerodynamic forces acting on a plunging and pitching airfoil by performing two-dimensional Direct Numerical Simulation to solve the Navier-Stokes equations for incompressible flow around an airfoil with an Immersed Boundary Method. This analysis is performed on NACA-0012 symmetric airfoils at reduced frequency of $k = 0.2\pi$ and plunging amplitude of $h/c = 1$. Different flapping configurations are considered by combining different mean pitch angles of $\theta_m = 0°$ and $10°$, pitching amplitude of $\theta_0 = 0°$, $10°$, $20°$ and $30°$ and Reynolds number of $Re = 3000$, 1000 and 500 at fixed phase shift $\phi = 90°$. The different simulated cases display diverse flow wake structures. The role of leading edge vortex and trailing edge vortex were found to be one key in the observed performance variation. For the analysed cases, it was noticed that the resulting wake structures are influenced by Re for flapping configuration with non-zero pitching amplitude, but they are independent of Re for zero pitching amplitude motions. Also, it was observed that increasing θ_0 results in lower effective angle of attack producing disappearance of vortex structures. Finally, this work evaluates the performance of a simplified model, developed in a parallel project [Moriche et al., 2016], to predict the aerodynamic forces acting on a flapping airfoil. It was noted that this model has an enormous potential to predict lift and thrust generation, even though it has a great simplicity.

Acknowledgements

First of all, I would like to express my deepest sense of gratitude to Prof. Manuel García-Villalba not only for trusting me and providing me the opportunity to realize this project but also for his continuous advice and encouragement throughout the course of this thesis. Also, I would like to thanks to Prof. Manuel Moriche for his extraordinary support and dedication and for his guidance during all the thesis process.

My very sincere thanks and appreciation to all the friends that I have met in the university and with whom I have shared the most part of the last four years. Thank you for converting all the hard working days in laughter and good times. Nothing would have been the same without your constant support and company and without your great sense of humour.

Last but not least, I would like to take this opportunity to express the profound gratitude from my deep heart to my parents and my elder brothers for their unconditional love and unfailing support throughout all my life. I will always be thankful to my parents for fighting tirelessly to ensure a better life for me and my brothers. Also, if my brothers had not led me the way forward I would not surely have arrived until here.

Contents

List of Tables

List of Figures

List of Symbols

C_L	lift coefficient
C_R	thrust coefficient
C_v	correction parameter of modelled fluid circulation
C_θ	correction parameter of modelled fluid circulation
c	chord
F_x	spanwise force component
F_z	vertical force component
$\vec{F}$	modelled aerodynamic forces
$\vec{F}^a$	modelled added-mass forces
$\vec{F}^c$	modelled circulatory forces
$\vec{F}^v$	modelled viscous forces
$\vec{F}_{KJ}$	circulatory force predicted by Kutta-Joukowsky theorem
f	flapping frequency
h	heaving motion
h_0	heaving amplitude
k	reduced frequency
M_y	aerodynamic moment
N_x	number of discretized domain cells in x-direction
N_z	number of discretized domain cells in z-direction
P	input power
p	fluid pressure
$p.c.$	points per chords
Re	Reynolds number
S_t	Strouhal number
T	oscillation period
T	thrust force
t	time
U_0	transitional velocity respect to center of gravity of airfoil in x-direction in reference frame fixed to the airfoil
U_∞	free stream velocity

u_i	velocity component
u_x	fluid velocity in x-direction
u_z	fluid velocity in z-direction
V_0	transitional velocity respect to center of gravity of airfoil in Z-direction of a reference frame fixed to the airfoil
$\vec{V}$	velocity of the fluid seen by the airfoil
X_0^a	modelled added mass force in x-direction in reference frame fixed to the airfoil
x	streamwise-direction axis
x_i	cartesian coordinates
x_p	distance from leading edge to pivoting point of airfoil
Z_0^a	modelled added mass force in z-direction in reference frame fixed to the airfoil
z	vertical-direction axis
α_e	effective angle of attack
β	tilting angle
Γ	modelled fluid circulation
η	propulsive efficiency
θ	pitching motion
θ_0	pitching amplitude
θ_m	mean pitch angle
ν	fluid kinematic viscosity
ξ	distance from leading edge to center of gravity of airfoil
ρ	fluid density
Ω	angular velocity respect to center of gravity of airfoil in reference frame fixed to the airfoil
ω	fluid vorticity

Abbreviations

2D	Two Dimensional
3D	Three Dimensional
BC	Boundary Conditions
CFD	Computational Fluid Dynamic
DNS	Direct Numerical Simulations
IBM	Immersed Boundary Method
LEV	Leading Edge Vortex
NACA	National Advisory Committee for Aeronautics
TEV	Trailing Edge Vortex

Chapter 1

Introduction

1.1 Background and motivation

From the dawn of time, the bird and insect flight has fascinated the human being. These flights have been observed by humans for many centuries trying to find the way to emulate them. As far back as the early of 16th century Leonardo Da Vinci made the first approximation of a conceptual sketch of a flying machine. The manned flights began in the 19th century thanks to brilliant minds such as Otto Lilienthal, the most dedicated and successful creator of flying machines at that time, designer of many hang gliders. Over the past century, significant advances in powered flights have been made, pushing away the technological boundaries of flight with the development of supersonic and rotary-wing aircraft. The recent efforts in aeronautical field are focusing on the increase of efficiency and performance of aircraft. Up to now, although the aeronautical technology has advanced rapidly over the past 100 years, the flapping wing flights are not yet properly understood.

Flapping wings are commonly found in nature. There are nearly a million species of small birds and flying insects using them to take the skies. The aerodynamics of flapping wings are used by these small animals to produce lift and propulsion and to control their position. The conventional fixed wings are relatively simple compared to flapping wings. In fixed wings, the forward motion relative to the air causes the wings to generate lift, with the thrust being produced by the engine (via either propellers or exhaust gas). However, in biological flights the wings not only move forward relative to the air but they also flap up and down, plunge and sweep, so that, both lift and thrust can be generated and balanced in accordance with the instantaneous flight conditions. In addition, birds and insects combine these movements with wing deformation, body contour and tail adjustment, to significantly enhance the manoeuvrability in the flight, allowing natural flyers to track targets precisely at amazing speeds.

The performance of nature's flyers is impressive. They are capable of flying at velocities of more than 120 body lengths per seconds, while human moves at top speeds of 4 body length per seconds, a cheetah accomplishes 18 and a supersonic aircraft as SR-71 "Blackbird" near Mach 3 covers about 32 body lengths per seconds. Also they can achieve roll rates of $5000°/s$ (highly acrobatic aircraft can reach to $720°/s$) and they can experiment routinely G-forces in excess of 12 G (military aircraft withstand 8-10 G).

Recently, with the advent of micro-aerial vehicles (MAVs) due to their commercial, research and military applications, the aerodynamics of flapping wings have attracted a relevant attention in the engineering and science community. MAVs are equipped with different sensors to perform surveillance and reconnaissance, targeting and biochemical sensing at remote otherwise hazardous locations. These vehicles have a maximum dimension of 15 cm and their cruising speed is in the order of 10-20 m/s. In contrast to civilian transport and many military flights vehicles, the MAVs operate at low Reynolds number (Re). The flight conditions of MAV flights are similar to that of small birds and insects. That is why the MAV design has been biologically inspired on them, because the flapping wings could provide higher manoeuvrability than fixed or rotary wings at those flying characteristics.

At low Reynolds numbers, flow separation and laminar-turbulent transition can result in substantial change in effective airfoil shape affecting the aerodynamic performance. Also, since they are lightweight and operate at low speeds, they are sensitive to wind gusts. Furthermore, their wing structures are flexible and tend to deform during flight. Consequently, the aero/fluid and structural dynamics of these flyers are closely linked to each other, making the entire flight vehicle difficult to analyse. There exist many challenges in the unsteady aerodynamics of flapping wings. Thus, it is crucial to improve the understanding of the unsteady aerodynamics and control mechanism that these flight animals employ. A key factor to achieve this target and to enhance the performance of bio-inspired MAVs, is to be able to predict the aerodynamic forces and moments as a function of the wing motion parameters with simplified models.

When insects and small birds flap their wings, they systematically twist them to produce the desired aerodynamic effects, in the same fashion as a conventional wing's aileron. They move their wings in a so-called stroke plane by combining wing rotation with respect to their wing-body junction and wing pitching with respect to a spanwise axis. In addition, the stroke plane is not fixed and might be tilted by the animal when performing manoeuvrings.

In this project, the aerodynamic forces of a flapping airfoil are analysed. The 3D motion of a flapping wing is too much complex, but assuming that the aspect ratio of the wing is large (in the limit of infinite aspect ratio) and the Reynolds number is low, it is possible to simplify the problem to a 2D airfoil configuration. Therefore, the complex 3D motion of the wing is reduced to a vertical oscillation, so-called heaving or plunging, and a rotation of the

airfoil with respect to a pivoting point, so-called pitching. Albeit, that still leaves us with a too large number of parameters to specify:

- Reynolds number of the flow.
- Airfoil geometry.
- Position of pivoting point.
- Frequency of oscillation.
- Temporal laws of evolution of plunging and pitching motions.

Thus, although the problem is considerably simpler in 2D, the task of generalize the acquired knowledge and obtain general laws to predict the aerodynamic forces and moments is still intimidating.

1.2 Literature Review

Because of their small size and high beat frequencies, it is often quite difficult to quantify the wing motions of free flying insects and small birds. Just the mere quantification of motion for such small and fast-moving wings continues to pose significant challenges to current technology. Over the years, the flapping wings have been the focus of many studies. Researchers have overcome the limitations of the knowledge of flapping wings with two strategies. The first method involves constructing dynamically scaled models on which it is easier to directly measure aerodynamic forces and visualize flows. And, a second approach is to construct Computational Fluid Dynamic (CFD) simulations of flapping wings. Since the beginning of 20th century, there are many numerical and experimental studies about oscillating airfoils, trying to understand the mechanisms responsible for the thrust and lift production. Also, the relation of the generated wake structures with the flapping configuration to generate them is a relevant matter of study. Although flapping refers to the combination of plunging and pitching motions, there are also many studies where the problem has been further simplify by considering only plunging or only pitching motions in order to extract information from a simpler problem.

1.2.1 Pure plunging airfoils

The studies of pure plunging airfoils have the objective of studying the thrust generation, usually by means of the qualitative analysis of the generated wake structures and their relation with the production of aerodynamic forces. The vertical motion of the airfoil produces

an effective angle of attack, so that, the resulting normal force vector has a component in the forward direction. This results in thrust generation.

[Anderson et al., 1998] analysed the principal characteristics of the flow around and in the wake of the airfoil, observing that high efficiency accompanied by significant thrust development is associated with the generation of moderately strong vortical structures. The main vortical structures are Leading Edge Vortices (LEV) and Trailing Edge Vortices (TEV).

[Young and Lai, 2004] shown that the wake structures and the thrust and lift forces are strongly dependent on both the reduced frequency and related Strouhal number of the plunging airfoil. [Lewin and Haj-Hariri, 2003] and [Wang, 2000] (numerical studies) observed that the separation of LEV at low frequencies leads to diminished thrust and efficiency. At high frequencies, the efficiency decreases similarly as in inviscid theory. The optimum heaving frequency in terms of efficiency should correspond to the period with which vortices are shed from impulsively started airfoils. For that, the timing of the LEV separation is crucial. Thus, a significant gain in efficiency occurs when the LEV remains attached for the duration of each stroke. [Lewin and Haj-Hariri, 2003] also found in the simulations that the wake patterns depends primarily on the fate of the LEV, whether or not it is shed, and how it interacts with the TEV. The high thrust coefficients and propulsive efficiencies correspond to positive reinforcement of the TEV by the LEV. Furthermore, they noted that large efficiency occurs at the transition from a shed LEV to one that is dissipated. [Martín-Alcántara et al., 2015] provided a quantitative description of some of these interactions using a vortex force decomposition.

There exist also many experimental studies about the wake structure formation of plunging airfoils as in [Lai and Platzer, 1999] and [Lua et al., 2007]. Also, the effects of specific flapping parameters, as the spanwise flexibility in [Heathcote et al., 2008], are experimentally studied.

1.2.2 Pure pitching airfoils

Some studies are focused only in pure pitching motion. Those studies have the objective to analyse the influence of pitching rate, pitching amplitude and Reynolds number on the pressure and vorticity fields generated in the vicinity of the airfoil.

[Walker et al., 1985] studied the surface pressure with an experimental investigation of energetic dynamic stall vortices. They found that increasing the pitch rate and Reynolds number results in inverse effects on the flow field in the immediate vicinity of the airfoil. However, the maintenance of a constant non-dimensional pitch rate produces very similar flow fields and pressure coefficients.

Furthermore, [Freymuth, 1988] and [Koochesfahani, 1989] demonstrated experimentally that an airfoil undergoing in pure pitching motion is capable of producing thrust. They also observed the existence of a axial flow in the cores of the wake vortices with a linear dependence on the frequency and amplitude of pitching oscillation.

1.2.3 Plunging and pitching airfoils

There exist also many studies of plunging and pitching airfoils. These studies focus on many different objectives. Some studies try to determine the optimum parametric combination for thrust production and others for both lift and thrust generation. But the required parametric combinations, and therefore the developed studies, are completely different. Nevertheless, as in the pure heaving motion, the relation between vortical structures and the resulting aerodynamic forces is of major interest.

For lift production, the important role played by LEV has long been recognized. The lift enhancement by spiral LEV bears several similarities to high-lift devices employed in certain man-made wings, where the potential of attached vortices in augment lift has been recognized in aerodynamics, but the spanwise flow component is essential for the stability of vortex. [Ellington et al., 1996] explained that this flow is generated either by the dynamic pressure gradient associated with the velocity gradient along the flapping wing by centrifugal acceleration in the boundary layer, or by the induced field of the spiral vortex lines. However, the exact conditions to establish an axial flow enabling a stable and persistent LEV in order to have a positive influence on the lift are not yet understood. This is a subject of current debate as in [Ford and Babinsky, 2013] or [Widmann and Tropea, 2015].

Other analyses have been focused in the discussion of the influence of some involved parameters on the flapping performance. [Miao and Ho, 2006] investigated the effect of chord-wise flexure amplitude on unsteady aerodynamic characteristics for a flapping airfoil with various combinations of Reynolds number and reduced frequency. [Ashraf et al., 2011] analysed numerically the Reynolds number, thickness and camber effects on flapping airfoil propulsion. [Isogai et al., 1999] studied the effects of dynamic stall phenomena on the behaviour of propulsive efficiency and thrust by examining each obtained flow pattern. Experimentally, [Fenercioglu and Cetiner, 2012] categorized the flow structures around a flapping airfoil depending on separated vorticity patterns and analysed the parameter spaces in which each flow structure category occurs.

1.3 Objectives of this project

The initial objective of this project was the comparison and validation of the results obtained in a numerical simulation of flow over a flapping airfoil with a experimental analysis in a companion project.

Due to the delay in the achievement of results of the experimental analysis, the objectives of this project were redefined. The final objectives of this project are briefly depicted below.

- Study the influence of some flapping parameters like the Reynolds number and the pitching configuration on the aerodynamic forces acting on a flapping airfoil.
- Evaluate the performance of a simplified model to predict the aerodynamic forces, developed in a parallel study [Moriche et al., 2016], for the simulations analysed in this work.
- Optimize the value of the free coefficients, of which the simplified model is dependent, in order to find the influence of flapping parameters as the Reynolds number and pitching configuration to improve the performance of the model.

1.4 Structure of this document

The core of the present document is constituted by eight chapters. This section exposes a brief outline of the contents of each chapter.

- Chapter 1 is composed of four sections. The background and motivation section serves as a general introduction to flapping airfoil and presents the studied problem. The literature review compiles the work performed by other authors. The objectives section describes the goals of this project. Finally, the present section summarizes the contents of this document.
- Chapter 2 describes the numerical method used to solve the unsteady aerodynamic problem. It defines the governing equation of fluid motion, the flow solver and the computational set-up.
- Chapter 3 defines the studied problem. This chapter is divided in four section. The first explains the kinematic of flapping airfoils. The second defines all the simulations performed in this project. And the third and forth sections explain the reason for the selection of their involved parameters and their resolutions, respectively.
- Chapter 4 shows the results for the analysed simulations. This chapter is composed of two different sections. The first shows and analyses the aerodynamic forces acting

on the airfoil. The second one defines, evaluates and optimizes a simplified model of forces developed in a parallel project [Moriche et al., 2016].

- Chapter 5 provides the project planning and work time distribution.
- Chapter 6 describes the socioeconomic impact and regulatory framework and includes an estimated budget to developed this project.
- Chapter 7 draws some conclusion and introduces a brief summary of the main ideas discussed in this project. Also states further considerations for future researches related to the work performed on this project.
- Additionally, an Appendix is added to Chapter 8 in order to collect complementary results to the ones analysed in Chapter 4.

Chapter 2

Numerical Method

This chapter explains the numerical method used to carry out the performed simulations. It is divided in three sections. The first section describes the governing equations for the fluid motion. The second defines the flow solver. It includes the explanation of the used numerical approach, the spatial discretization, the time marching and the method used to include the body on the mesh. The last section depicts the domain discretization and the imposed boundary conditions.

2.1 Governing equations

The fluid motion around a flapping airfoil is adequately described by the continuity and momentum Navier-Stokes equations for an incompressible flow, defined as:

$$\frac{\partial u_i}{\partial x_i} = 0 \tag{2.1}$$

$$\frac{\partial u_i}{\partial t} + u_i \frac{\partial u_i}{\partial x_i} = -\frac{1}{\rho}\frac{\partial p}{\partial x_i} + \nu \frac{\partial^2 u_i}{\partial x_i^2} \tag{2.2}$$

where u_i is the velocity component, x_i the cartesian coordinates, p the pressure, and ρ the fluid density.

2.2 Flow solver

2.2.1 Direct Numerical Simulations (DNS)

The flow method used to solve the Navier-Stokes equations for an incompressible flow is a two-dimensional Direct Numerical Simulations (DNS), carried out with an in-house code named TUCAN. The use of a DNS instead of a modelling involves a more precise analysis but also a higher computational cost, because the flow solutions are obtained solving the Navier-Stokes equations in all points of the mesh-grid instead of computing the solution by means of a theoretical model. TUCAN has been extensively validated with a collection of cases that include cannonical 2D laminar flows (Poiseuille flow, Taylor-Green vortices, stationary and moving cylinders), as well as fully-developed turbulent channel flow inside a channel and flow around a sphere [Moriche, 2016].

In order to fulfil the temporal-independent continuity (eq. 2.1) and temporal-dependent momentum (eq. 2.2) equations, a fractional step method is used to solve them as explained in [Brown et al., 2001]. This method consists of obtaining the velocity from the momentum equation and then introducing a correction to fulfil both continuity and momentum incompressible Navier-Stoke equations.

The spatial discretization is done with second-order, centred finite differences in a uniform staggered grid. Time marching is performed with a three-stage low-storage Runge-Kutta scheme, in which diffusion terms are treated implicitly and advective term explicitly. The coefficients of the Runge-Kutta as well as the detailed used method can be found in [Roma et al., 1999]. All simulations are run at constant Δt, which is chosen to ensure that during all the simulation the CFL $= u\Delta t/dx < 0.2$, for stability reasons.

2.2.2 Immersed Boundary Method (IBM)

The presence of the body is modelled using the Immersed Boundary Method (IBM). For this kind of analysis, a IBM is computationally more efficient than a body fitted grid method. In IBM the difficulty of the grid definition for complex geometries is highly reduced and, for moving bodies, it presents real computational resources savings, where remeshing and interpolation at the end of every time step is eliminated. On contrast, when Reynolds number increases, the boundary layer must be thinner (higher resolution) and the IBM needs to be fitted in the two directions.

The IBM implemented is the one described in [Uhlmann, 2005], a diffuse discrete forcing approach method using regularised delta functions with a 3 points stencil to interpolate from the Eulerian (fluid) mesh to the Lagrangian (body) mesh.

The body is considered as rigid and the interaction between fluid and solid is uni-directional, the kinematics of the body movement are known and imposed directly. In this method, the presence of a solid in the fluid is substituted by adding a forcing term (correction) in the momentum equation.

The followed steps to solve the Navier-Stokes equations are listed below.

1. Make an explicit estimation of the velocity in Eulerian mesh.
2. Interpolate that value to Lagrangian velocity using the regularized delta functions.
3. Calculate the volume force from estimated Lagrangian velocity and the desired one.
4. Transform this volume force from Lagrangian to Eulerian frame.
5. Introduce this forcing term in momentum equation.
6. Solve Navier-Stokes equations by means of the fractional step method.

With this method, due to the displacement of the airfoil, nodes belonging to solid mesh become fluid mesh nodes without historical data. This effect produces fluctuations in the results obtained from the DNS. These fluctuations are corrected by means of a low pass filter by replacing each data point with the average of the neighbouring data points defined within the span.

Figure 2.1 shows the highest signal fluctuations for all the performed simulations, and how they are corrected by the low pass filter.

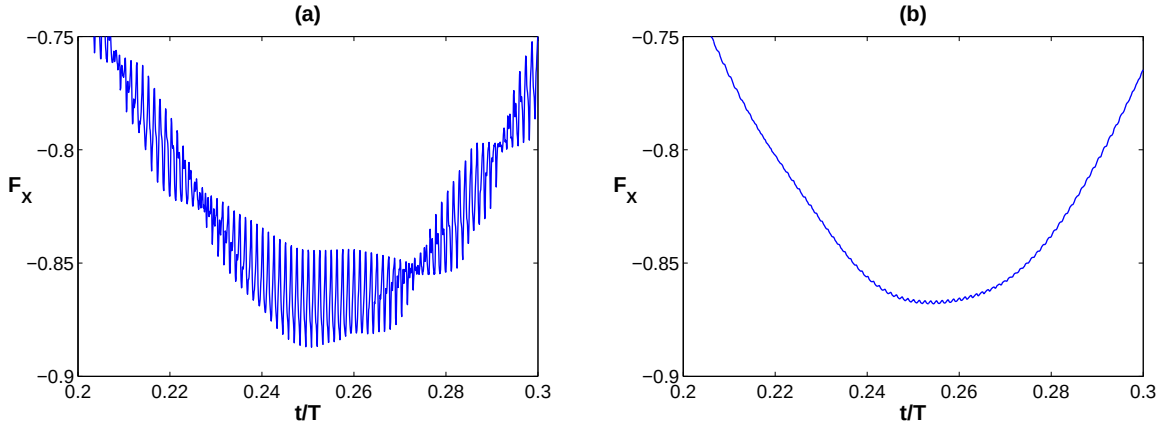

Figure 2.1: Example of the correction on the spanwise force response of one simulation by means of a low pass filter. a) Results without filter, b) Results using the low pass filter

All the results presented in chapter 3 and 4 and in the Appendix of Chapter 8 have been corrected by means of this smoothing filter before their presentations.

2.3 Computational set-up

2.3.1 Domain

For all the simulations presented in section 3, the computational domain is a rectangular box of $12c \times 8c$ in the streamwise and vertical direction, respectively. The reference length c is a chord, which will be described in section 3.1. To discretize that domain, a staggered grid with a uniform mesh width is used. The nodes position for the velocity components and for the pressure, as well as the dimensions of the rectangular box domain, can be seen in the Figure 2.2.

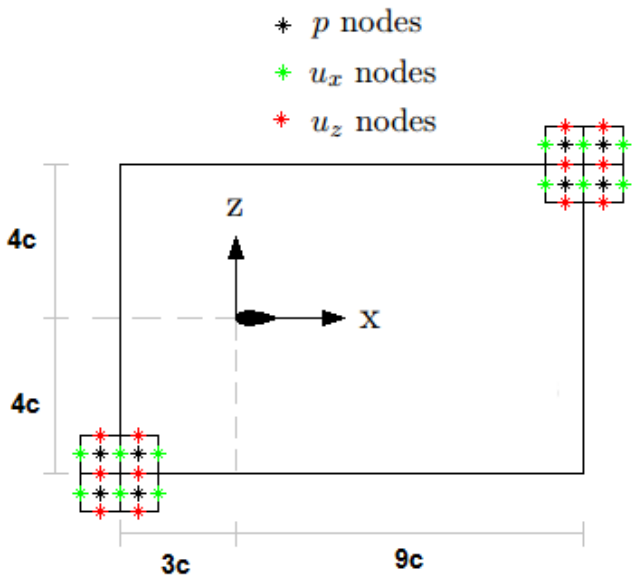

Figure 2.2: Sketch of the domain describing cartesian staggered grid of the fluid domain.

The mesh size is defined by N_x and N_z cells in x and z directions respectively, but these are reference values because the number of mesh points in each directions differs from one variable to another due to the staggered feature of the mesh.

The resolution used to discretize the domain (N_x, N_z) depends on the Reynolds number. The higher the Re, the higher the needed resolution to perform an accurate analysis. The chosen resolution for each of the performed simulations will be depicted in chapter 3.

2.3.2 Boundary Conditions (BC)

The boundary conditions for the 2D DNS are given by an uniform free-stream imposed at the inlet plane (located 3 chords upstream of the leading edge of the airfoil), convective boundary conditions at the outlet plane (8 chords downstream of the trailing edge), and free-slip boundary conditions on the vertical boundaries at z = ±4c. These BCs can be shown in Figure 2.3

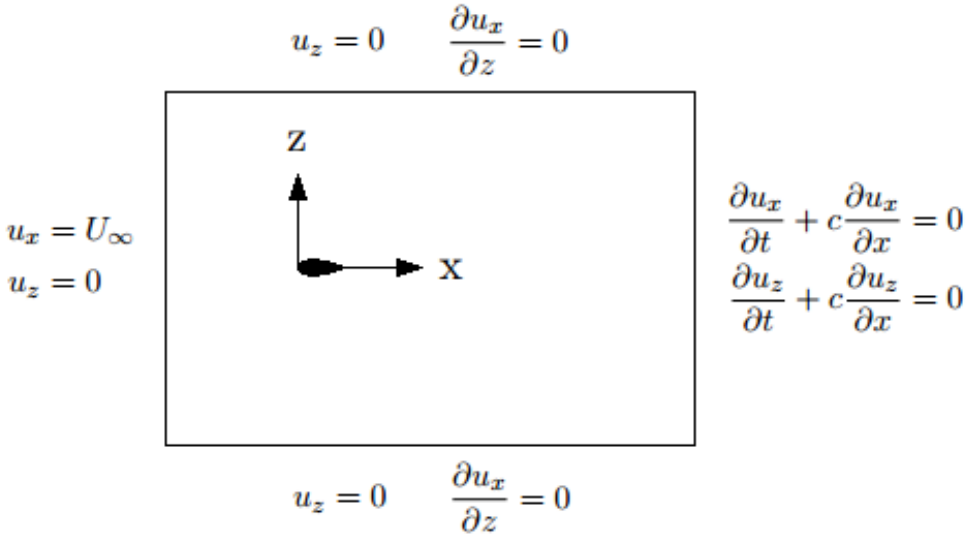

Figure 2.3: Sketch of the imposed boundary conditions.

Chapter 3

Problem definition

This chapter is composed of four sections. The first sections describes the kinematics of plunging and pitching airfoils. This description includes the identification of the temporal laws of the evolution of flapping motion and all their involved parameters. The second section defines all the performed simulations and their involved parameters. The third explains the reasons for the choice of the parametric range of the simulations. And the last section shows the analysis used to choose the required resolutions for each case.

3.1 Flapping motion

Figure 3.1 shows the main kinematic features of the flapping motion.

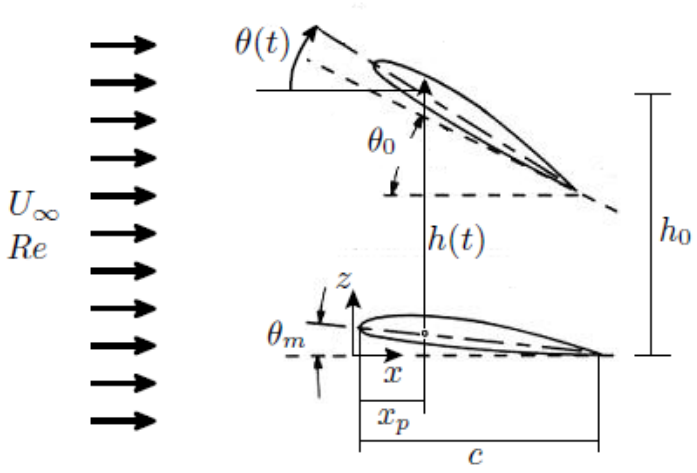

Figure 3.1: Sketch of the kinematics parameters of the flapping motion of the airfoil.

where x and z are the streamwise and vertical directions, respectively.

As it is described in Figure 3.1, the flow is defined by means of their stream velocity (U_∞) and Reynolds number (Re) which is defined as:

$$Re = \frac{U_\infty c}{\nu} \tag{3.1}$$

where c is the chord of the airfoil and ν is the kinematic viscosity of the flow.

The rest of parameters on Figure 3.1 are the mean pitch angle (θ_m), the pitching amplitude (θ_0), the plunging amplitude (h_0) and the distance from the leading edge to the pivoting point of the airfoil (x_p), point on which the airfoil does the plunging and pitching motions, which are given by:

$$h(t) = h_0 \cos(2\pi f t) \tag{3.2}$$

$$\theta(t) = \theta_m + \theta_0 \cos(2\pi f t + \phi) \tag{3.3}$$

where $h(t)$ is the vertical displacement of the pivoting point and $\theta(t)$ the pitching angle (angle between the chord and the free stream), both of them with the same frequency (f), but with a phase shift (ϕ) between them.

The frequency of the flapping motion can be also described by means of the reduced frequency (k) or with the Strouhal number (St), which relates the motion frequency with the heaving amplitude, key parameters in the developed wake structures of flapping motions. Those parameters are defined as:

$$k = \frac{2\pi f c}{U_\infty} \tag{3.4}$$

$$St = \frac{2h_0 f}{U_\infty} = \frac{k}{\pi}\frac{h_0}{c} \tag{3.5}$$

Finally, the period of oscillation of the airfoil can be expressed as:

$$T = \frac{1}{f} = \frac{2\pi}{k}\frac{c}{U_\infty} \tag{3.6}$$

Figure 3.2 displays the motion followed by the airfoil in one oscillation period.

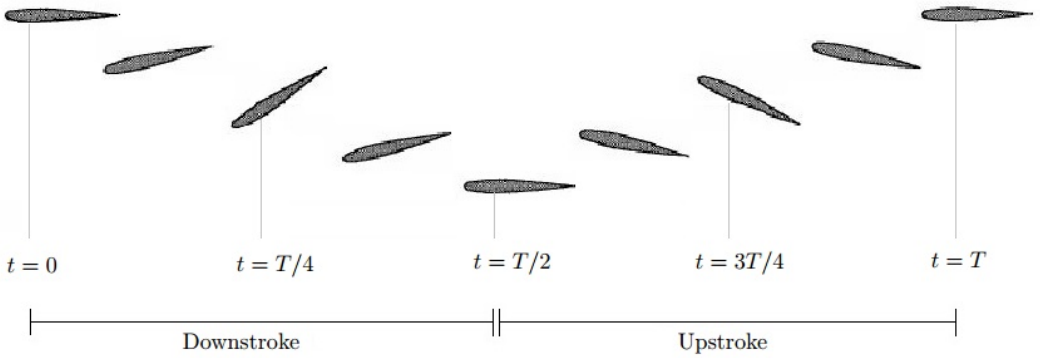

Figure 3.2: Sketch of the plunging and pitching motion in one period.

It is also important to define the effective angle of attack (α_e) during the oscillation period, which is the angle of attack relative to the locally deflected free stream.

$$\alpha_e(t) = \theta(t) + \arctan(-\frac{1}{U_\infty}\frac{dh}{dt}) \tag{3.7}$$

Therefore, the parameters that must be selected in order to define the desired flapping simulations are the following:

- Reynolds number of the flow, Re.
- Airfoil geometry.
- Position of pivoting point, x_p.
- Reduced frequency of oscillation, k.
- Plunging and pitching motion parameters, θ_m, θ_0, h_0 and ϕ.

3.2 Description of the simulations

In this project, 17 simulations have been performed in order to analyse different flapping motions at different Reynolds numbers.

Some parameters describing the airfoil motion have been fixed for all the developed simulations. These fixed parameter are:

Airfoil geometry:	NACA-00012
Plunging amplitude:	$h_0/c = 1$
Phase shift:	$\phi = 90°$
Pivoting point position:	$x_p/c = 0.25$

Table 3.1: Fixed parameters for all the developed simulations

The remaining parameters, θ_m, θ_0 and k, as well as Re, have been varied to configure all the cases described in the Table 3.2.

Case	θ_m	θ_0	Re	k	$p.c.$
B_{00a}	0°	0°	1000	0.2π	128
B_{00b}	0°	10°	1000	0.2π	128
A_{00c}	0°	20°	500	0.2π	72
B_{00c}	0°	20°	1000	0.2π	128
C_{00c}	0°	20°	3000	0.2π	192
B_{00d}	0°	30°	1000	0.2π	128
A_{10a}	10°	0°	500	0.2π	72
B_{10a}	10°	0°	1000	0.2π	128
C_{10a}	10°	0°	3000	0.2π	192
B_{10b}	10°	10°	1000	0.2π	128
A_{10c}	10°	20°	500	0.2π	72
B_{10c}	10°	20°	1000	0.2π	128
$C_{10c,1}$	10°	20°	3000	0.2π	192
$C_{10c,2}$	10°	20°	3000	0.4π	192
$C_{10c,3}$	10°	20°	3000	0.4π	160
$C_{10c,4}$	10°	20°	3000	0.4π	128
B_{10d}	10°	30°	1000	0.2π	128

Table 3.2: Summary table of simulated cases specifying their key parameters: mean pitch angle θ_m, pitching amplitude θ_0, Reynolds number Re, reduced frequency k and points per chord p.c.

The simulations are named according to the following rules:

- The first capital letter indicates the Reynolds number.
  A: $Re = 500$ — **B**: $Re = 1000$ — **C**: $Re = 3000$
- The two digits number of the sub-index indicate the mean pitch angle.
  00: $\theta_m = 00°$ — **10**: $\theta_m = 10°$
- The lower-case letter of the sub-index indicates the pitching amplitude.
  a: $\theta_0 = 00°$ — **b**: $\theta_0 = 10°$ — **c**: $\theta_0 = 20°$ — **d**: $\theta_0 = 30°$
- The final number in sub-index (it is present only in four cases) distinguishes the reduced frequency and the resolution of the case C_{10c}.

3.3 Selection of the parameters

As explained in section 1.4, the initial objective of this project was the numerical simulation of the flow over a flapping airfoil and the validation with the experimental data obtained in a companion project. For that reason, both project looked a intersection on the achievable parametric range of both analysis. Thus, in this numerical analysis the first chosen parameter was the higher possible Reynolds number with a assumable computational cost ($Re = 3000$), that was close to the minimum Re that the experiment could achieve. The rest of parameters were chosen to imitate the ones of the experimental analysis ($k = 0.4\pi$, $\theta_m = 10°$ and $\theta_0 = 20°$). Therefore, the first developed simulations were the cases $C_{10c,4}$, $C_{10c,3}$ and $C_{10c,2}$ (three cases in order to define the needed resolution as explained in next section). After these cases were computed, the experimental project had to reduce their flapping frequency. To adapt to this change, the case $C_{10c,1}$ was simulated with a new reduced frequency of $k = 0.2\pi$.

Finally, the objective of this project was changed to analyse the effect of certain flapping parameters on the aerodynamic forces. To perform this analysis, the following simulations were developed with different plunging configuration (θ_m, θ_0) and with different Reynolds numbers (Re) departing from the case $C_{10c,1}$. Therefore, three flapping motions were analysed at three Reynolds numbers (A_{10c}–B_{10c}–$C_{10c,1}$, A_{10a}–B_{10a}–C_{10a} and A_{00c}–B_{00c}–C_{00c}) and two mean pitch angles at $Re = 1000$ were analysed at four pitching amplitudes (B_{00a}–B_{00b}–B_{00c}–B_{00d} and B_{10a}–B_{10b}–B_{10c}–B_{10d})

3.4 Selection of the resolution

As explained in section 2.2.6, the resolution required to obtain an accurate solution is dependent of the Reynolds numbers. The higher the Re, the thinner the mesh in both directions of the grid (N_x, N_z). That is why, at $Re > 3000$ the computational cost is too excessive for a project like this one.

For the simulations with $Re = 3000$, the resolution analysis was made with the cases $C_{10c,4}$, $C_{10c,3}$, $C_{10c,2}$, with 128, 160 and 192 points per chord, respectively.

In order to analyse the accuracy of those simulations, Figure 3.3 shows the results obtained in one period for $F_x/\rho U_\infty^2 c$ and $F_z/\rho U_\infty^2 c$, the non-dimensional streamwise and vertical components of the force acting on the flapping airfoil. Furthermore, Table 3.3 shows the value of the errors (ϵ_{F_x}, ϵ_{F_z}) between the obtained force components on a oscillation period taking as reference the case $C_{10c,2}$ and the standard deviation of these errors ($\sigma_{\epsilon_{F_x}}$, $\sigma_{\epsilon_{F_z}}$).

The error (ϵ) can be quantified as root mean squared deviation between the forces, normalized with the amplitude of the reference case:

$$\epsilon = \frac{\sqrt{\frac{1}{n}\sum_{i=1}^{n}(F_{ref,i} - F_i)^2}}{A_{F_{ref}}} \tag{3.8}$$

where n is the number of measurements of the force for one oscillation period and the sub-index i represents each of them. The F_{ref} are the forces obtained in case $C_{10c,2}$ which are used as the reference and $A_{F_{ref}}$ are the amplitude values of the reference forces ($A_F = F_{max} - F_{min}$).

The standard deviation (σ_ϵ) measures the amount of variation in the obtained error. It is defined as:

$$\sigma_\epsilon = \sqrt{\frac{1}{n}\sum_{i=1}^{n}(\epsilon_i - \bar{\epsilon})^2} \tag{3.9}$$

where $\bar{\epsilon}$ is the average value of the error on a motion period:

$$\bar{\epsilon} = \frac{1}{n}\sum_{i=1}^{n}(\epsilon_i) \tag{3.10}$$

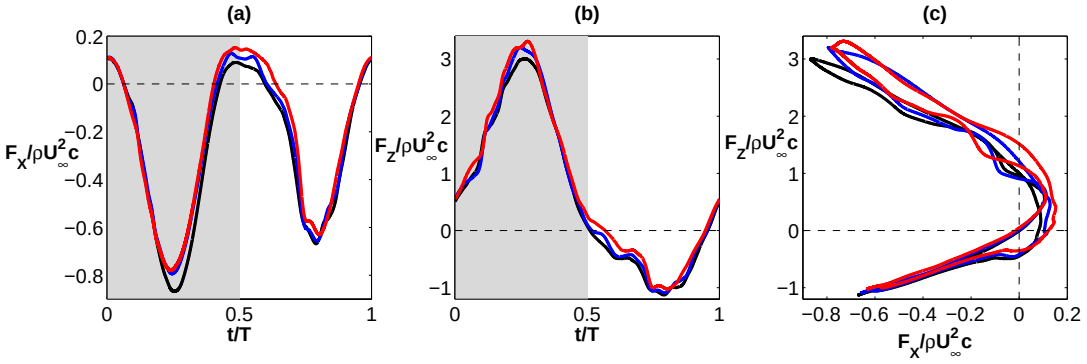

Figure 3.3: Variation with different resolutions of a) $F_x/\rho U_\infty^2 c$ b) $F_z/\rho U_\infty^2 c$ c) $\vec{F}$ direction. —— $C_{10c,4}$, —— $C_{10c,3}$, —— $C_{10c,2}$.

Case	$p.c.$	ϵ_{F_x}	$\sigma_{\epsilon_{F_x}}$	ϵ_{F_z}	$\sigma_{\epsilon_{F_z}}$
$C_{10c,2}$	192	-	-	-	-
$C_{10c,3}$	160	0.0398	0.0221	0.0277	0.0608
$C_{10c,4}$	128	0.0798	0.0412	0.0429	0.0894

Table 3.3: Errors in the measurement of force components (ϵ_{F_x}, ϵ_{F_z}) and their standard deviations ($\sigma_{\epsilon_{F_x}}$, $\sigma_{\epsilon_{F_z}}$) taking as the reference value the forces obtained in case $C_{10c,2}$.

From Figure 3.3 it can be noticed that the differences between the obtained results are minor for these three resolutions. Table 3.3 shows that between cases $C_{10c,2}$ and $C_{10c,3}$, the obtained errors for the streamwise and vertical force components are 3.98% and 2.77% respectively, relatively small errors.

Then, for a domain discretization of 192 point per chord, yielding a total of 2304×1536 grid points in streamwise and vertical directions, respectively, the obtained results are accurate enough taking into account the computational cost to continue increasing the resolution. Also, as the analysis was made for a case with higher frequency than for the rest of simulated cases, for those with lower frequency the required resolution will be lower and the grid of 2304×1536 points will be even more accurate.

A similar grid refinement study was performed in other project [Gonzalo, 2016] for cases with $Re = 1000$ and $Re = 500$. For the first ones, it was analysed a plunging NACA-0012 airfoil with $h_0/c = 1$ and reduced frequency $k = 1$, in a uniform free-stream with $Re = 1000$. Runs at different resolutions (between 32 and 256 points per chord) have been performed in a computational domain of $12c \times 8c$ in the streamwise and vertical direction respectively. The results of this study shows that the acceptable resolution was 96 points per chord or higher. At that Reynolds, the domain of the cases analysed in this work was discretized using a resolution of 128 point per chord, yielding a total of 1536×1024 of grid points in streamwise and vertical directions, respectively, corresponding to slightly over-resolved simulations. Also, it must be taken into account that, as for the cases with $Re = 3000$, the frequency of the simulations of this project is lower than the used one in the grid refinement study of [Gonzalo, 2016].

For the cases with $Re = 500$ the analysis was performed for a pure plunging motion with $h_0/c = 1$ and $k = 1$ at $Re = 500$, at different resolutions (from 32 to 192 points per chord). This study concludes that the use of a resolution of 72 point per chord is accurate enough. According to these results, the domain of the cases with $Re = 500$ was discretized using a resolution of 72 point per chord, yielding a total of 864×576 of grid points in streamwise and vertical directions, respectively. As for the cases with $Re = 1000$ and $Re = 3000$, the frequency used in this project is lower than the used for the mesh refinement study, and for that, the reliability of the results with this resolution will be even higher.

Chapter 4

Results

This chapter is focused on the analysis of the simulations of Table 4.1. This analysis covers 14 of the 17 simulated cases. The cases which are not analysed in this chapter are the cases $C_{10c,2}$, $C_{10c,3}$ and $C_{10c,4}$. These cases were simulated in order to find the proper resolution for simulations with $Re = 3000$ as explained in section 3.2.

Case	θ_m	θ_0	Re	k	$p.c.$	Case	θ_m	θ_0	Re	k	$p.c.$
B_{00a}	0°	0°	1000	0.2π	128	B_{10a}	10°	0°	1000	0.2π	128
B_{00b}	0°	10°	1000	0.2π	128	C_{10a}	10°	0°	3000	0.2π	192
A_{00c}	0°	20°	500	0.2π	72	B_{10b}	10°	10°	1000	0.2π	128
B_{00c}	0°	20°	1000	0.2π	128	A_{10c}	10°	20°	500	0.2π	72
C_{00c}	0°	20°	3000	0.2π	192	B_{10c}	10°	20°	1000	0.2π	128
B_{00d}	0°	30°	1000	0.2π	128	$C_{10c,1}$	10°	20°	3000	0.2π	192
A_{10a}	10°	0°	500	0.2π	72	B_{10d}	10°	30°	1000	0.2π	128

Table 4.1: Summary table of analysed cases specifying their key parameters: mean pitch angle θ_m, pitching amplitude θ_0, Reynolds number Re, reduced frequency k and points per chord $p.c.$

This chapter is formed of two sections. The first studies the aerodynamic force coefficients. This analysis is performed studying the influence of the Reynolds number (Re) and the pitching motion (θ_m, θ_0) on the their mean and amplitude values and on their evolution over a motion period. All the analysed cases have the same reduced frequency ($k = 0.2\pi$).

The second section introduces a simplified model to predict the aerodynamic forces, developed in a parallel project [Moriche et al., 2016]. This model is applied to the analysed simulations in order to evaluate it performance with the flapping configurations presented in this work. This reduced order model depends on two coefficients. Firstly, in the evaluation of the model, the coefficients given from parallel project are used. Then, the values of those free parameter are optimized to analyse the influence of Re, θ_m and θ_0 in the value of these coefficients.

4.1 Analysis of aerodynamic forces coefficients

This section is divided in three parts. The first shows and compares the mean and amplitude values of the aerodynamic force coefficients obtained in DNS for the different analysed cases. The second part provides a detailed analysis of the influence of Re in the evolution of aerodynamic forces and in the developed wake structures. The last part of this section gives a similar study for the influence of θ_0 in one motion period.

The performance of the flapping motion will be analysed in terms of non-dimensional coefficients of lift and thrust, defined as:

$$C_L(t) = \frac{2F_z(t)}{\rho U_\infty^2 c} \tag{4.1}$$

$$C_T(t) = -\frac{2F_x(t)}{\rho U_\infty^2 c} \tag{4.2}$$

where F_z and F_x are the forces in vertical and streamwise directions respectively, consequently with Figure 3.1.

Also the propulsive efficiency will be examined. It is defined as the ratio of useful power over the input power, or in other words, the ability of the airfoil to generate thrust related with the needed flapping motion. This parameter can be computed as:

$$\eta = \frac{UT}{P} = \frac{U_\infty \int_0^T F_x dt}{\int_0^T (F_z \dot{h} + M_y \dot{\theta}) t} \tag{4.3}$$

where M_y is the aerodynamic moment on the pivoting point, and $\dot{h}$ and $\dot{\theta}$ are the first time derivatives of heaving and pitching motions described in eq. 3.2 and eq. 3.3 respectively. These first time derivatives are defined as:

$$\dot{h} = -2\pi f h_0 \sin(2\pi f t) \tag{4.4}$$

$$\dot{\theta} = -2\pi f \theta_0 \sin(2\pi f t + \phi) \tag{4.5}$$

4.1.1 Mean and standard deviation of force coefficients and propulsive efficiency

The forces obtained in all the cases have a periodical behaviour. However, there exists a slight difference between consequent motion periods for each case. For that, the values of the lift and thrust coefficients for all the cases have been computed as the average of the last four simulated motion periods.

Table 4.2 shows the variation of the mean ($\overline{C_L}$, $\overline{C_T}$) and the standard deviation (σ_{C_L}, σ_{C_T}) of the force coefficients, and the propulsive efficiency (only for thrust producing cases) for three different flapping motions. Table 4.3 displays the variation of these studied parameters with θ_0, at fixed Re for two different θ_m.

$\overline{C_L}$ and $\overline{C_T}$ represent the mean value of the aerodynamic force coefficients over a motion period. A positive $\overline{C_L}$ means that, in a complete motion period, the flapping motion is generating lift, and a positive $\overline{C_T}$ that it is generating thrust. These values are computed as:

$$\overline{C_X} = \frac{1}{T}\int_0^T C_X(t) \tag{4.6}$$

where C_X stands for lift (C_L) or thrust (C_T) coefficients.

On the other hand, σ_{C_L} and σ_{C_T} represent the amplitude of the values of the force coefficients in one motion period, defined as:

$$\sigma_{C_X} = \sqrt{\frac{1}{T}\int_0^T (C_X(t) - \overline{C_X})^2} \tag{4.7}$$

Case	θ_m	θ_0	Re	$\overline{C_L}$	σ_{C_L}	$\overline{C_T}$	σ_{C_T}	η
$C_{10c,1}$	10°	20°	3000	0.8679	0.9104	-0.0307	0.2456	-
B_{10c}	10°	20°	1000	0.6506	0.8608	-0.0649	0.2167	-
A_{10c}	10°	20°	500	0.5008	0.7341	-0.1294	0.1650	-
C_{10a}	10°	0°	3000	0.3855	1.9897	-0.1061	0.3555	-
B_{10a}	10°	0°	1000	0.2534	2.0122	-0.1186	0.3516	-
A_{10a}	10°	0°	500	0.3374	1.9410	-0.2004	0.3353	-
C_{00c}	0°	20°	3000	0.0384	1.0462	0.1925	0.2327	0.4220
B_{00c}	0°	20°	1000	0.0000	0.8367	0.0834	0.2033	0.2413
A_{00c}	0°	20°	500	-0.0001	0.7252	0.0061	0.1467	0.0198

Table 4.2: Kinematic parameters of the cases analysed with different Reynolds numbers. Mean ($\overline{C_L}$, $\overline{C_T}$) and standard deviation (σ_{C_L}, σ_{C_T}) of force coefficients and propulsive efficiency (η).

Case	θ_m	θ_0	Re	$\overline{C_L}$	σ_{C_L}	$\overline{C_T}$	σ_{C_T}	η
B_{00a}	0°	0°	1000	0.0010	1.9832	-0.0882	0.2097	-
B_{00b}	0°	10°	1000	-0.0004	1.5507	0.0867	0.2927	0.1267
B_{00c}	0°	20°	1000	0.0000	0.8367	0.0834	0.2033	0.2413
B_{00d}	0°	30°	1000	-0.0001	0.2523	-0.0765	0.0766	-
B_{10a}	10°	0°	1000	0.2534	2.0122	-0.1186	0.3516	-
B_{10b}	10°	10°	1000	0.6999	1.3852	-0.0787	0.2562	-
B_{10c}	10°	20°	1000	0.6506	0.8606	-0.0649	0.2167	-
B_{10d}	10°	30°	1000	0.9641	0.4953	-0.1460	0.2125	-

Table 4.3: Kinematic parameters of the cases analysed with different pitching amplitude. Mean ($\overline{C_L}$, $\overline{C_T}$) and standard deviation (σ_{C_L}, σ_{C_T}) of force coefficients and propulsive efficiency (η)

First of all, it is known that the flapping motion without mean pitch angle ($\theta_m = 0°$) does not generate lift as it will be explained further on. However, these cases have a small value different from zero. It is because the obtained results are the mean of four motion periods, which have slight differences between them. For that, the results obtained in mean lift coefficient for cases with zero θ_m are not exactly equals to zero.

From Table 4.2 and Table 4.3 it can be noticed that the case with better performance with respect to lift generation is the case B_{10d}, the one with the highest analysed pitching amplitude ($\theta_0 = 30°$) and with non-zero mean pitch ($\theta_m = 10°$) at a Re of 1000. Regarding thrust generation, only cases with zero mean pitch generate thrust, and the better performance is obtained in case C_{00c} at the highest analysed Reynolds number ($Re = 3000$) with a $\theta_0 =$ of 20°. For the propulsive efficiency, the case C_{00c} also exhibits the better performance.

Additionally, it must be pointed out that the standard deviations are of the same or even higher order of magnitude than the mean values. That is an indicative of the highly oscillatory behaviour of the aerodynamic forces over a flapping airfoil.

The variation of the mean force coefficients ($\overline{C_L}$, $\overline{C_T}$) and propulsive efficiency (η) is presented graphically in Figure 4.1 and Figure 4.2:

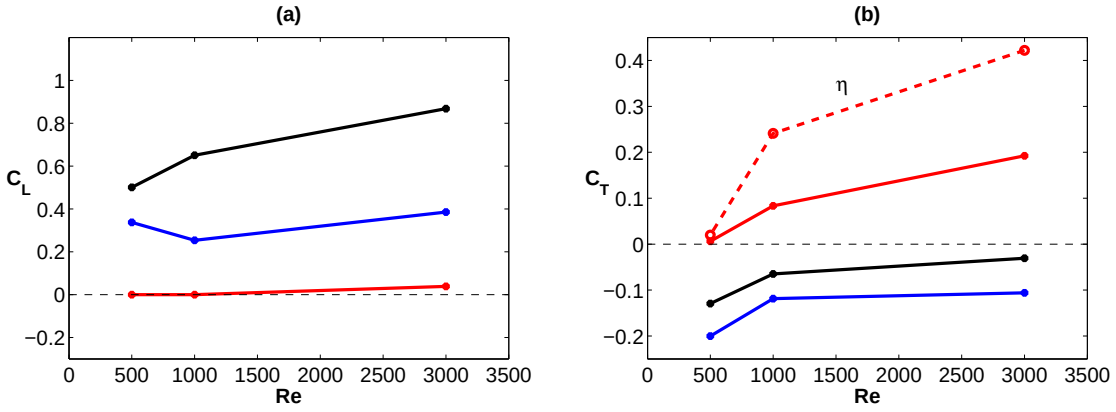

Figure 4.1: Variation with Reynolds number for the cases with fixed θ_m and θ_0 of a) $\overline{C_L}$ b) $\overline{C_T}$. $\theta_m = 10°$, $\theta_0 = 20°$, $\theta_m = 10°$, $\theta_0 = 0°$, $\theta_m = 0°$, $\theta_0 = 20°$, η [$\theta_m = 0°$, $\theta_0 = 20°$].

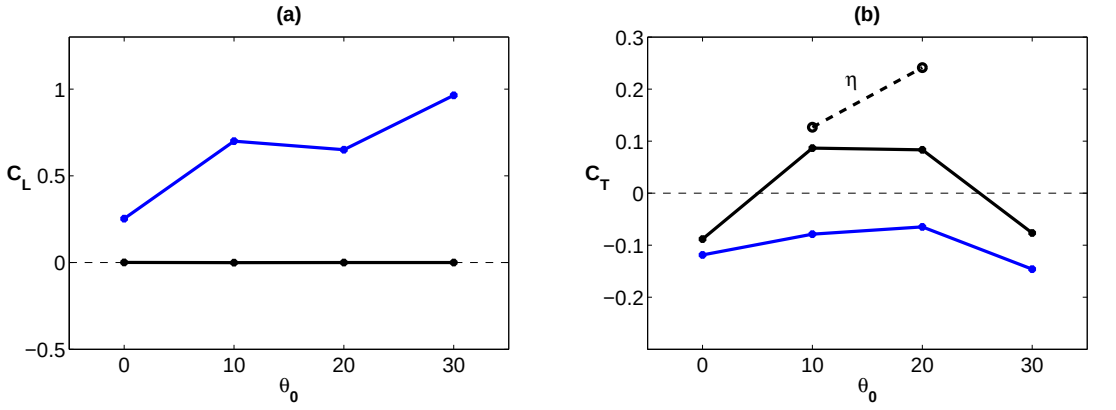

Figure 4.2: Variation with pitching amplitude for cases with $Re = 1000$ at different θ_m of a) $\overline{C_L}$ b) $\overline{C_T}$ $\theta_m = 0°$, $\theta_m = 10°$, η [$\theta_m = 10°$].

From Table 4.2 and Figure 4.1 it can be noticed that increasing the Re results in higher $\overline{C_T}$ and σ_{C_T}. In addition, note how, for the cases with $\theta_m = 0°$ and $\theta_0 = 20°$, at $Re = 500$ the $\overline{C_T} \approx 0$ and only by increasing the Re, $\overline{C_T} \approx 0.2$ at $Re = 3000$. However, for the evolution of C_L with Re does not exist a clear trend. While for the cases with non-zero pitching amplitude, increasing the Re leads to higher mean and standard deviation of lift coefficient, for the cases with zero pitching amplitude there are not a clear tendency. In the case of η, the only cases with positive propulsive efficiency have zero mean pitch angle but non-zero pitching amplitude. For the cases with $\theta_m = 0°$ and $\theta_0 = 20°$, just like for $\overline{C_T}$, the value of η increases significantly by increasing the Reynolds numbers, from just 2% at $Re = 500$ to 42% at $Re = 3000$.

On the other hand, from Table 4.3 and Figure 4.2 it is appreciated that at a fixed θ_m and Re, there exists an optimum pitching amplitude maximizing the thrust generation in the range from $\theta_0 = 0°$ to $\theta_0 = 30°$. The propulsive efficiency also has a maximum value in the θ_0 range producing thrust with $\theta_m = 10°$. Also, it is interesting to see that at fixed $Re = 1000$ and $\theta_m = 10°$, while the obtained $\overline{C_T}$ is approximately equal with a θ_0 of 10° or 20°, the propulsive efficiency doubles from 12.7% with $\theta_0 = 10°$ to 24.1% with $\theta_0 = 20°$. Regarding to lift generation, in cases with zero mean pitch angle there are not production of lift because the one generated downstroke is counteracted by the negative one generated in upstroke. This occurs due to the opposite value of the effective angle of attack in both segments as it can be seen in Figure 4.3a. But, with the introduction of a mean pitch angle of $\theta_m = 10°$, lift is generated. In those cases, increasing θ_0 from 0° to 10°, $\overline{C_L}$ increases 176%, conversely from $\theta_0 = 10°$ to $\theta_0 = 20°$, $\overline{C_L}$ decreases a 7%, but again from $\theta_0 = 20°$ to $\theta_0 = 30°$, $\overline{C_L}$ increases 48%. Finally, it can be seen that the higher the pitching amplitude, the lower the amplitude value of lift coefficient (σ_{C_L}).

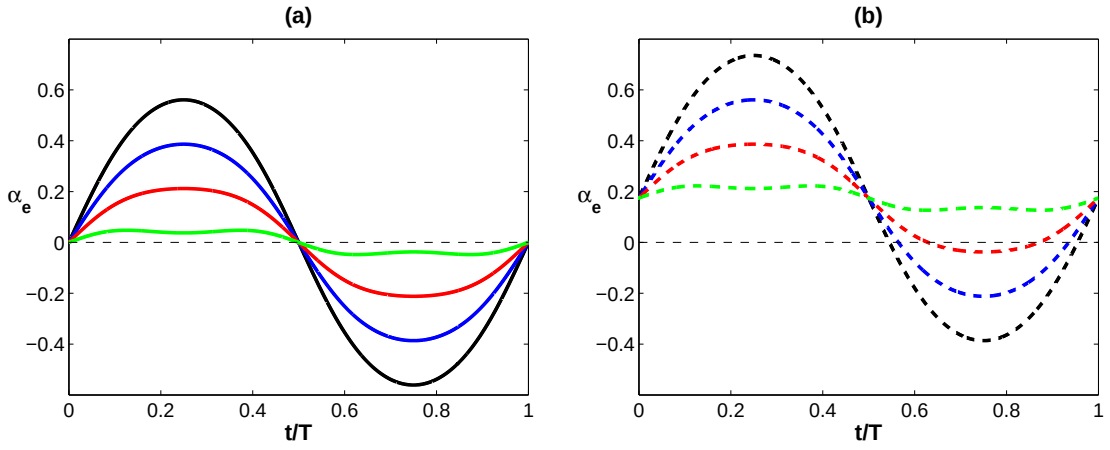

Figure 4.3: Evolution in one oscillation period of effective angle of attack (α_e) in cases a) —— B_{00a}, —— B_{00b}, —— B_{00c}, —— B_{00d}; b) - - - B_{10a}, - - - B_{10b}, - - - B_{10c}, - - - B_{10d}.

4.1.2 Evolution of force coefficients in one oscillation period. Variation with Reynolds number (Re)

This section analyses the variations with Re of the aerodynamic force coefficients (C_L, C_T). This analysis involves the comparison between the coefficients over a period at different Reynolds number at three flapping configurations and the study of the flow characteristics at the vicinity of the airfoil at certain moments of interest. As the results obtained for all the analysed cases have a periodical behaviour, the figures show only one motion period.

Cases with $\theta_m = 10°$ and $\theta_0 = 20°$

The first analysis is performed on cases $C_{10c,1}$, B_{10c} and A_{10c}. As described in Table 4.1, those simulations have the same flapping configuration ($\theta_m = 10°$, $\theta_0 = 20°$ and $k = 0.2\pi$) but different Re, being 3000, 1000 and 500 respectively.

Figure 4.4 displays the results for C_L and C_T over one period for these three simulations, and Figure 4.5 shows the vorticity and pressure fields at the vicinity of the airfoil at $t/T = 0.4375$.

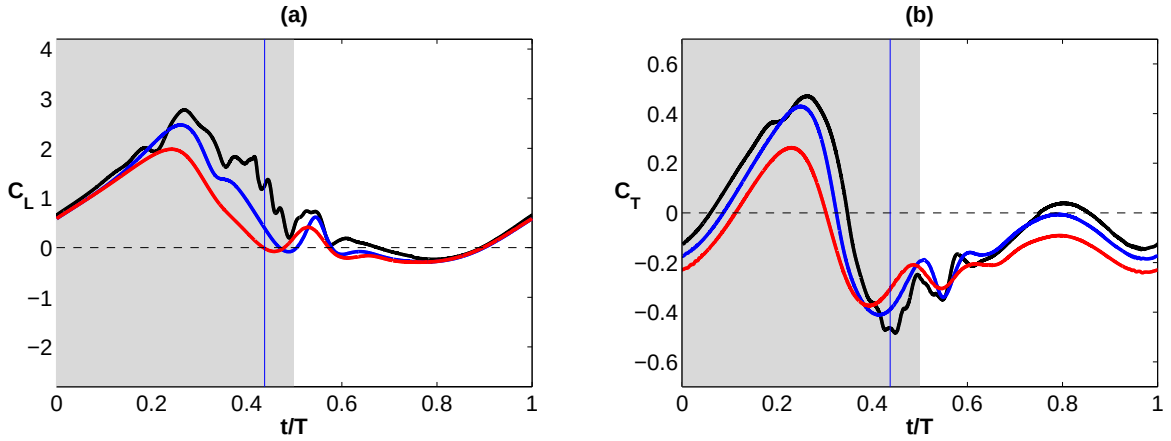

Figure 4.4: Results in one period for cases with fixed $\theta_m = 10°$ and $\theta_0 = 20°$ at different Re of a) C_L b) C_T. Grey region represent the downstroke and white region the upstroke. Vertical line represents the time instant studied in flow visualization figure. —— $C_{10c,1}$ [$Re = 3000$], —— B_{10c} [$Re = 1000$], —— A_{10c} [$Re = 500$].

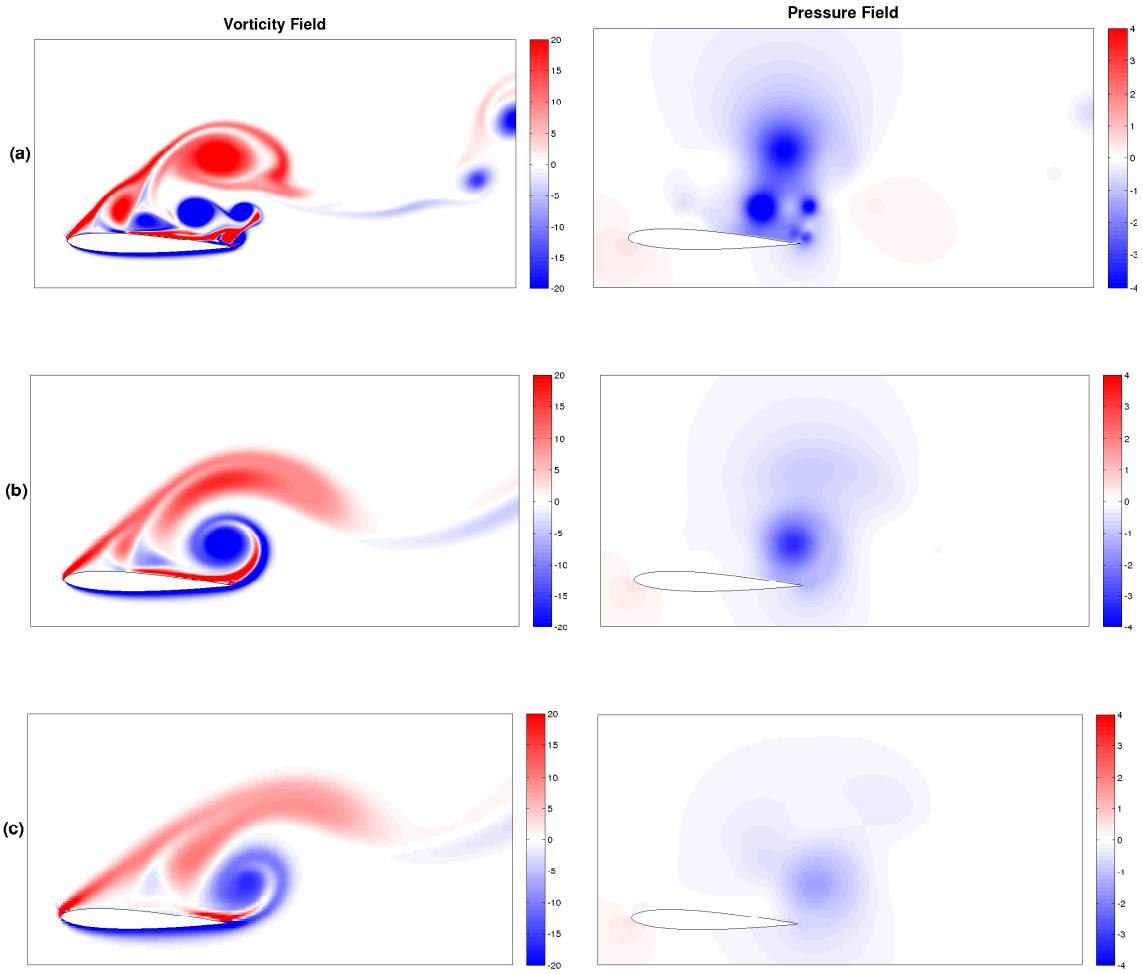

Figure 4.5: Flow visualization of vorticity (left) and pressure (right) fields near the airfoil at the end of the downstroke (t/T = 0.4375) for case with fixed $\theta_m = 10°$ and $\theta_0 = 20°$ at different Re. In vorticity field, blue indicates $\omega c/U_\infty = -20$ (anticlockwise) and red $\omega c/U_\infty = 20$ (clockwise). In pressure field, blue indicates $p/\rho U_\infty^2 = -4$ and red $p/\rho U_\infty^2 = 4$. a) $C_{10c,1}$ [$Re = 3000$] b) B_{10c} [$Re = 1000$] c) A_{10c} [$Re = 500$].

First of all, as it is shown in Figure 4.4, the flapping motion can be divided in two parts, the downstroke (grey background) from $t/T = 0$ to $t/T = 0.5$ and the upstroke (white background) from $t/T = 0.5$ to $t/T = 1$.

Figure 4.4 shows that the lift is generated during the downstroke and no lift is produced during upstroke. This is an expected results since the effective angle of attack is almost zero during upstroke (Figure 4.3b). On the other hand, thrust is created during the middle of the downstroke, but during the rest of the oscillation the flapping generates drag. The differences in lift production due to the Reynolds number take place in downstroke motion, specifically in the last part. The higher the Reynolds number, the higher the lift created during this part of the period. This higher lift is reflected in the integrated values shown in Figure 4.1.

Those differences can be explained in Figure 4.5 by plotting the vorticity (ω) and pressure (p) fields at $t/T = 0.4375$. This time instant is selected because the differences in both lift and thrust are more noticeable.

The vorticity of the flow is defined as:

$$\omega = \frac{\partial u_x}{\partial z} - \frac{\partial u_z}{\partial x}, \tag{4.8}$$

where u_x and u_z are the velocity component of the flow in the streamwise and vertical directions, respectively.

In Figure 4.5 it can be appreciated clearly the difference between lift generation in the last part of downstroke ($t/T = 0.4375$). At that time instant, in the case $C_{10c,1}$ ($Re = 3000$) there are created one LEV and two TEV, while in cases B_{10c} ($Re = 1000$) and A_{10c} ($Re = 500$) the LEV is blurred and only one TEV is formed. These flow structures generate a negative pressure difference producing a suction effect on the upper surface of the airfoil, near to the trailing edge. This suction is translated to a lift and drag generation. Also, decreasing the Re results in significantly lower intensity of the vorticity and the associated pressure. Those effects explain the differences in the lift generation of this flapping motion with the Re.

Cases with $\theta_m = 10°$ and $\theta_0 = 0°$

The second analysis is performed on cases C_{10a}, B_{10a} and A_{10a}, having the same flapping configuration ($\theta_m = 10°$, $\theta_0 = 0°$ and $k = 0.2\pi$) but different Re (3000, 1000 and 500, respectively). Figure 4.6 and Figure 4.7 show the results for C_L and C_T over one period and the vorticity and pressure fields at $t/T = 0.4375$, respectively.

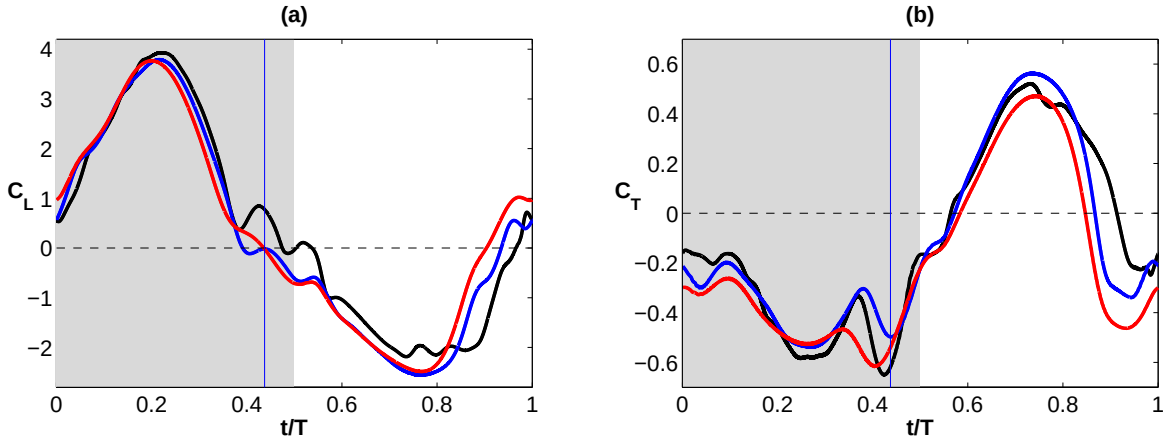

Figure 4.6: Results in one period for cases with fixed $\theta_m = 10°$ and $\theta_0 = 0°$ at different Re of a) C_L b) C_T. Grey region represent the downstroke and white region the upstroke. Vertical line represents the time instant studied in flow visualization figure. —— C_{10a} [$Re = 3000$], —— B_{10a} [$Re = 1000$], —— A_{10a} [$Re = 500$].

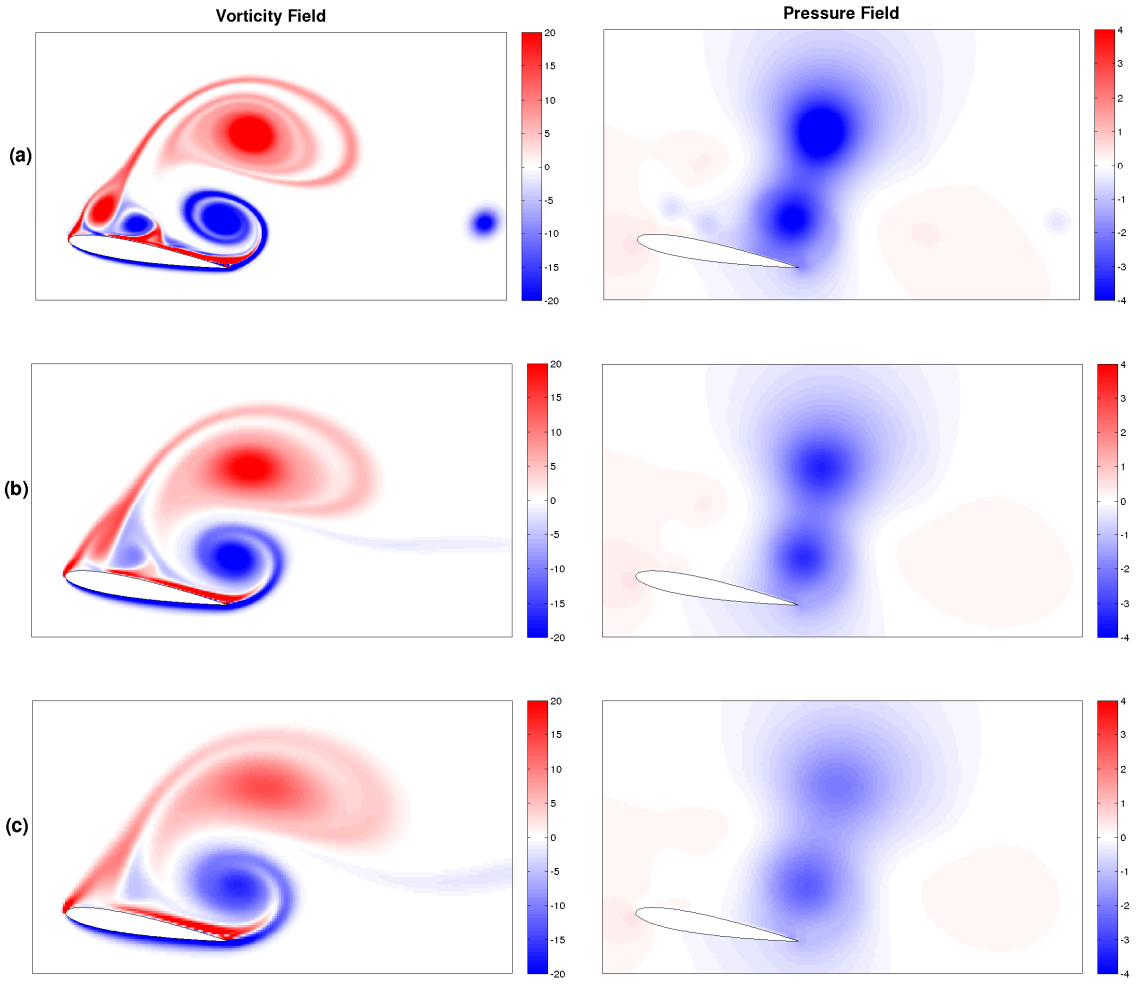

Figure 4.7: Flow visualization of vorticity (left) and pressure (right) fields near the airfoil at the end of the downstroke (t/T = 0.4375) for case with fixed $\theta_m = 10°$ and $\theta_0 = 0°$ at different Re. In vorticity field, blue indicates $\omega c/U_\infty = -20$ (anticlockwise) and red $\omega c/U_\infty = 20$ (clockwise). In pressure field, blue indicates $p/\rho U_\infty^2 = -4$ and red $p/\rho U_\infty^2 = 4$. a) C_{10a} [$Re = 3000$] b) B_{10a} [$Re = 1000$] c) A_{10a} [$Re = 500$].

In those cases, as it can be seen in Figure 4.6, the upstroke counteracts many part of the lift created during downstroke. Furthermore, the only part of this flapping motion creating thrust is at the middle of upstroke.

The differences in lift production at different Reynolds number are smaller compared to the previous cases. The results differ during upstroke and at the end of downstroke. In Figure 4.7 can be appreciated the differences of flow vorticity and pressure fields at this part of the period ($t/T = 0.4375$). In contrast to previous cases, the Re has not a significant influence in the flow structures created during this flapping motion, but it can still be seen that the intensity of the LEV created at the end of downstroke is slightly higher by increasing Re. Also, the differences in the associated pressure field vary in a similar way.

Cases with $\theta_m = 0°$ and $\theta_0 = 20°$

The last analysis of this section is performed on cases C_{00c}, B_{00c} and A_{00c}, having the same flapping configuration ($\theta_m = 0°$, $\theta_0 = 20°$ and $k = 0.2\pi$) but different Re, (3000, 1000 and 500, respectively). Figure 4.9 shows the results for C_L and C_T over one period for the three simulations at different Re, and Figure 4.8 shows the vorticity and pressure fields at the vicinity of the airfoil at the time instant $t/T = 0.4375$.

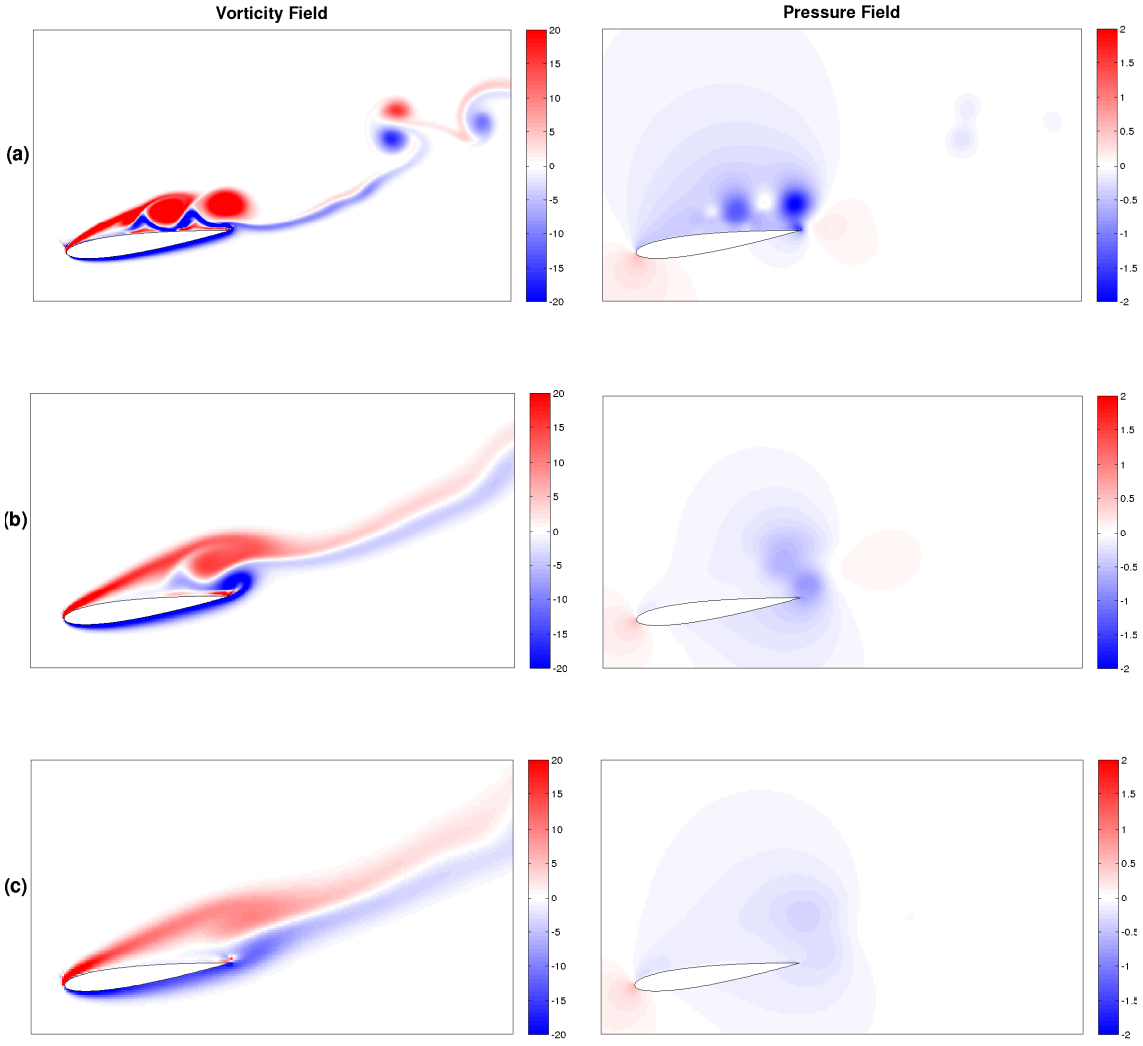

Figure 4.8: Flow visualization of vorticity (left) and pressure (right) fields near the airfoil at the end of the downstroke (t/T = 0.4375) for case with fixed $\theta_m = 0°$ and $\theta_0 = 20°$ at different Re. In vorticity field, blue indicates $\omega c/U_\infty = -20$ (anticlockwise) and red $\omega c/U_\infty = 20$ (clockwise). In pressure field, blue indicates $p/\rho U_\infty^2 = -2$ and red $p/\rho U_\infty^2 = 2$. a) C_{00c} [$Re = 3000$] b) B_{00c} [$Re = 1000$] c) A_{00c} [$Re = 500$].

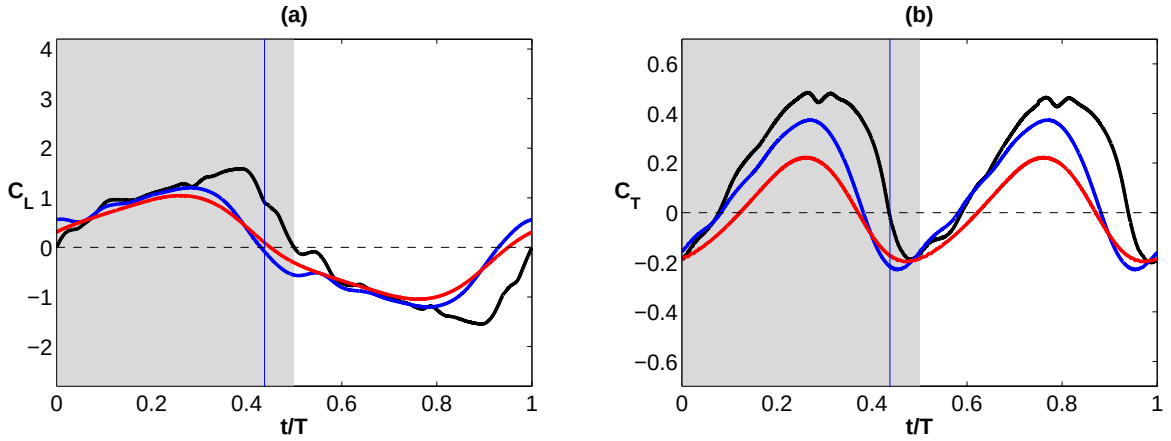

Figure 4.9: Results in one period for cases with fixed $\theta_m = 0°$ and $\theta_0 = 20°$ at different Re of a) C_L b) C_T. Grey region represent the downstroke and white region the upstroke. Vertical line represents the time instant studied in flow visualization figure. —— C_{00c} [$Re = 3000$], —— B_{00c} [$Re = 1000$], —— A_{00c} [$Re = 500$].

Figure 4.9 shows that in those cases, as explained in previous section, the lift created during downstroke is completely counteracted in the upstroke because the flapping motion is symmetric. Conversely, regarding thrust generation, the thrust created during downstroke is exactly equal to the one created in upstroke (asymmetric behaviour).

For those cases, as in the first ones, the Re influences in the flow structures generated as it can be seen in Figure 4.8. At $Re = 3000$ two LEV attached to the airfoil are formed, while at lower Re those LEV are blurred. This produces that increasing Re leads to higher lift created by the negative pressure of these vortex structures. Also as in all the previous analysed cases, the higher the Re the higher the intensity of vorticity and associated pressure of the fluid.

In conclusion, for all the analysed cases, at a flapping reduced frequency of $k = 0.2\pi$, the higher the Re of the flow, the higher the intensity of the vorticity and associated pressure generated by the flapping motion. This effect can suppose an increase or decrease of thrust and lift depending on the flapping configuration. Regarding the flow structure generation, it has been appreciated that for cases with non-zero pitching amplitude ($A_{10c} - B_{10c} - C_{10c,1}$ and $A_{00c} - B_{00c} - C_{00c}$) the Re has an important influence in the generation of vortex structures. For those cases, increasing Re results in higher amount of generated vortex structures. Nevertheless, for cases with zero pitching amplitude ($A_{10a} - B_{10a} - C_{10a}$), apparently the Re does not influence in the creation of LEV and TEV.

4.1.3 Evolution of force coefficients in one oscillation period. Variation with pitching amplitude (θ_0)

This section studies the variations with θ_0 of the aerodynamic force coefficients (C_L, C_T). This analysis involves the comparison between the coefficients over a period changing the value of θ_0 but maintaining the Re and θ_m. Also, as in previous section, it will be studied the vorticity and pressure fields at the vicinity of the airfoil at certain moments of interest.

Cases with $\theta_m = 0°$ and $Re = 1000$

The first analysis of this section is performed on cases B_{00a}, B_{00b}, B_{00c} and B_{00d}. As described in Table 4.1, those simulations have the same θ_m, Re and k ($\theta_m = 0°$, $Re = 1000$ and $k = 0.2\pi$) but different θ_0, being 0°, 10°, 20° and 30°, respectively.

Figure 4.10 displays the results for C_L and C_T over one period for these four simulations, and Figure 4.11 shows the vorticity and pressure fields at the vicinity of the airfoil at the time instant $t/T = 0.71875$.

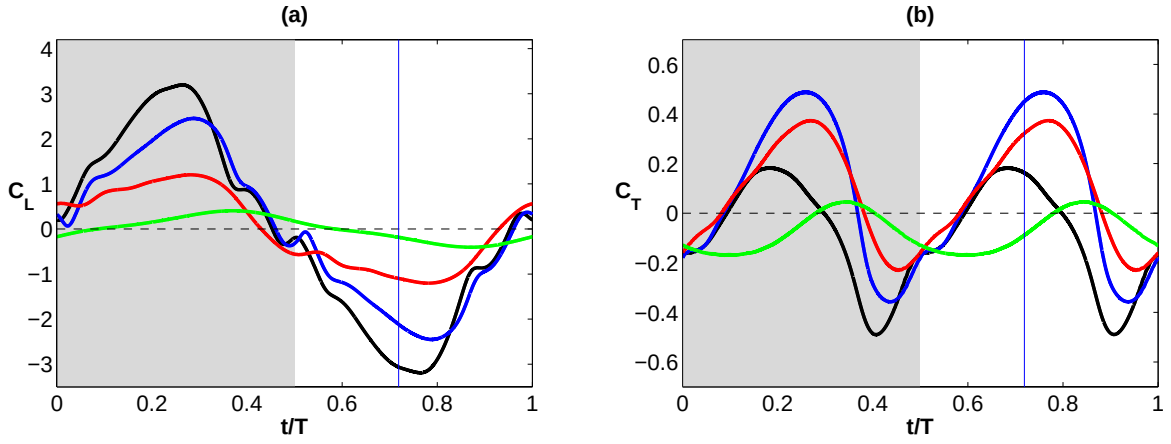

Figure 4.10: Results in one period for cases with fixed $Re = 1000$ and $\theta_m = 0°$ at different θ_0 of a) C_L b) C_T. Grey region represent the downstroke and white region the upstroke. Vertical line represents the time instant studied in flow visualization figure. —— B_{00a} [$\theta_0 = 0°$], —— B_{00b} [$\theta_0 = 10°$], —— B_{00c} [$\theta_0 = 20°$], —— B_{00d} [$\theta_0 = 30°$].

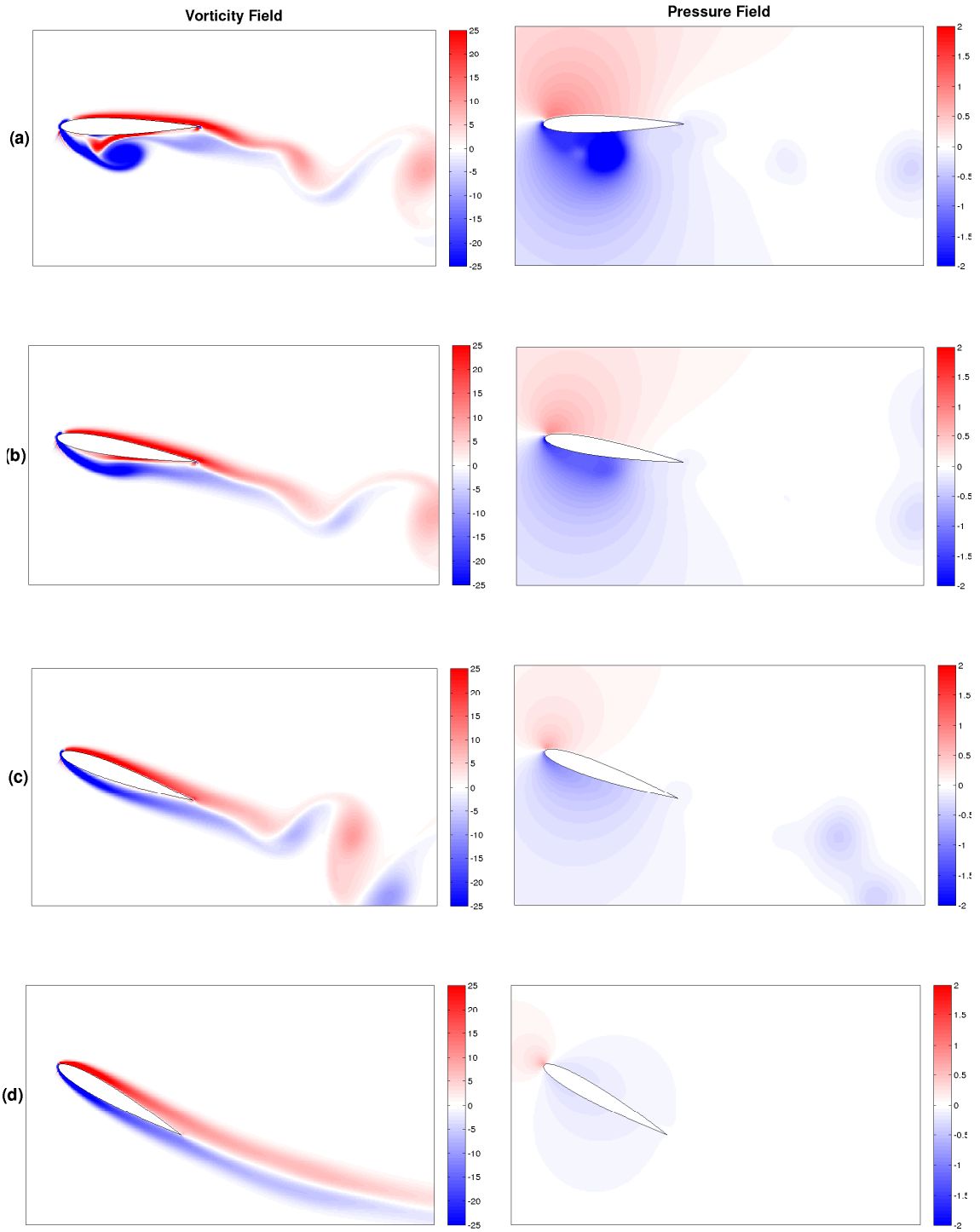

Figure 4.11: Flow visualization of vorticity (left) and pressure (right) fields near the airfoil at the middle of upstroke (t/T = 0.71875) for case with fixed $Re = 1000$ and $\theta_m = 0°$ at different θ_0. In vorticity field, blue indicates $\omega c/U_\infty = -25$ (anticlockwise) and red $\omega c/U_\infty = 25$ (clockwise). In pressure field, blue indicates $p/\rho U_\infty^2 = -2$ and red $p/\rho U_\infty^2 = 2$. a) B_{00a} $[\theta_0 = 0°]$ b) B_{00b} $[\theta_0 = 10°]$ c) B_{00c} $[\theta_0 = 20°]$ d) B_{00d} $[\theta_0 = 30°]$.

First of all, as it can be seen in Figure 4.9 and as it was explained in section 4.1.1, the lift created during downstroke is counteracted with the upstroke because the two motions are symmetric (Figure 4.3a). Conversely, the thrust created during downstroke is exactly equal to the one created in upstroke. Also, as explained in Table 4.3, increasing θ_0 results in lower amplitude of the generated lift. By increasing the pitching amplitude from 0° to 30° results in an increase of the lift coefficient amplitude of 700%.

Regarding the flow characteristic, and taking into account the symmetric behaviour of downstroke and upstroke, the case B_{00a} ($\theta_0 = 0°$) generates a LEV detached before the middle of upstroke and a TEV at the end of upstroke. The case B_{00b} ($\theta_0 = 10°$) generates the same TEV but the LEV is detached just after the middle of upstroke. However, the case B_{00c} ($\theta_0 = 20°$) generates only a weak TEV at the end of upstroke, and the case B_{00d} ($\theta_0 = 30°$) does not create any vortex flow structure. These features explain the evolution of lift and thrust coefficients. Figure 4.11 shows the flow vorticity and pressure fields just before the middle of the upstroke at $t/T = 0.71875$. At that time instant, the LEV starts to be detached in case B_{00a} and it is attached in case B_{00b}. However, cases B_{00a} and B_{00a} does not create any LEV. These flow structures generate the displayed associated pressure field.

Cases with $\theta_m = 10°$ and $Re = 1000$

The second analysis of this section is performed on cases B_{10a}, B_{10b}, B_{10c} and B_{10d}, having the same θ_m, Re and k ($\theta_m = 10°$, $Re = 1000$ and $k = 0.2\pi$) but different θ_0 (0°, 10°, 20° and 30°, respectively). Figure 4.12 displays the results for C_L and C_T over one period for these four simulations, and Figure 4.13 shows the flow vorticity and pressure fields at $t/T = 0.71875$.

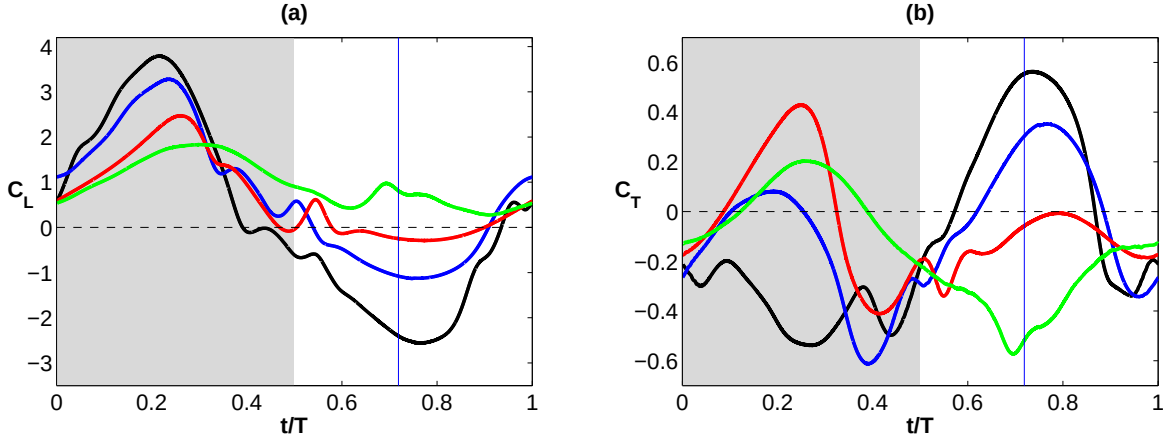

Figure 4.12: Results in one period for cases with fixed $Re = 1000$ and $\theta_m = 10°$ at different θ_0 of a) C_L b) C_T. Grey region represent the downstroke and white region the upstroke. Vertical line represents the time instant studied in flow visualization figure. —— B_{10a} [$\theta_0 = 0°$], —— B_{10b} [$\theta_0 = 10°$], —— B_{10c} [$\theta_0 = 20°$], —— B_{10d} [$\theta_0 = 30°$].

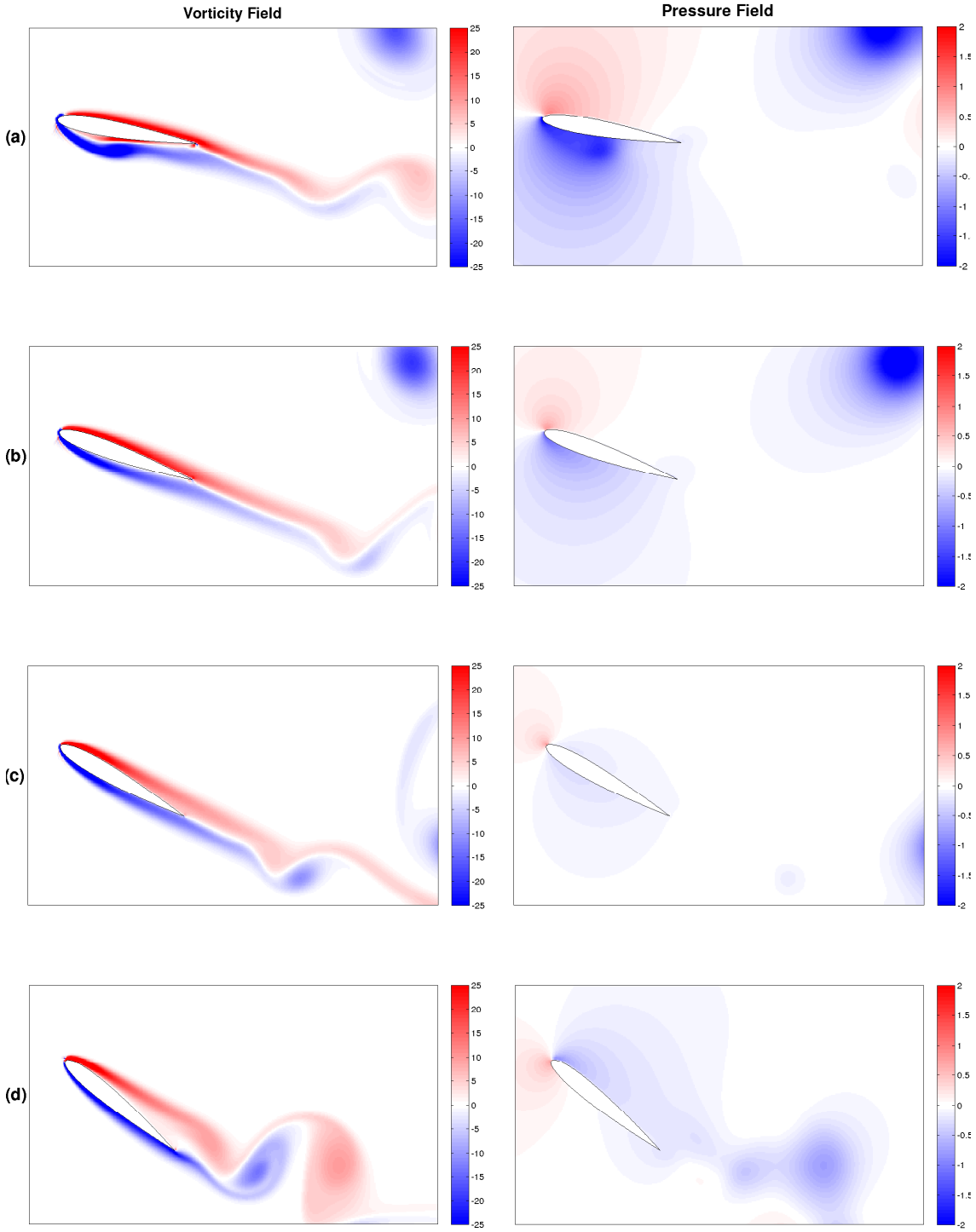

Figure 4.13: Flow visualization of vorticity (left) and pressure (right) fields near the airfoil at the middle of upstroke (t/T = 0.71875) for case with fixed $Re = 1000$ and $\theta_m = 10°$ at different θ_0. In vorticity field, blue indicates $\omega c/U_\infty = -25$ (anticlockwise) and red $\omega c/U_\infty = 25$ (clockwise). In pressure field, blue indicates $p/\rho U_\infty^2 = -2$ and red $p/\rho U_\infty^2 = 2$. a) B_{10a} [$\theta_0 = 0°$] b) B_{10b} [$\theta_0 = 10°$] c) B_{10c} [$\theta_0 = 20°$] d) B_{10d} [$\theta_0 = 30°$].

Figure 4.13 shows that by increasing the θ_m to 0° results in lift generation for all the cases. Also, it must be pointed out that case B_{10d} ($\theta_0 = 30°$) generates lift during all the flapping motion. Regarding thrust generation, the asymmetry in thrust creation of upstroke and downstroke of previous cases disappears by introducing a mean pitch value.

Concerning the flow characteristics, the vortex structures created during downstroke vary slightly with respect to the previous analysis. Cases B_{10a} ($\theta_0 = 0°$) and B_{10b} ($\theta_0 = 10°$) generate a LEV at the beginning of downstroke of greater intensity than in cases without mean pitch. This LEV is detached sooner than previous cases. Conversely, cases B_{10c} ($\theta_0 = 20°$) and B_{10d} ($\theta_0 = 30°$), as opposite to cases B_{00c} and B_{00d}, generate both a LEV and TEV during upstroke. Albeit, these flow structures are weak.

However, during upstroke different performance are observed. Case B_{10a} generates one LEV and one TEV, but the rest of the cases does not generate any vortex structure. Indeed, for case B_{10d} the suction over the airfoil is higher than the suction under the airfoil, meaning lift generation. Those features can be appreciated in Figure 4.13. This figure shows the vorticity and pressure fields at the middle of upstroke ($t/T = 0.71875$), when the LEV of case B_{10b} starts to be attached.

In conclusion, for the analysed flapping configurations, by increasing θ_0 results in lower effective angle of attack. This reduction of α_e produces a disappearance of vortex structures, resulting in lower lift generation. The introduction of a mean pitch angle of $\theta_m = 10°$ produces the elimination of the symmetric behaviour of the wake structure created during upstroke and downstroke of cases without mean pitch. Also, it is highlighted that the case with $\theta_m = 10°$ and $\theta_0 = 30°$ at $Re = 1000$ generates lift during all the motion period.

4.2 Modelling of Forces

One of the key factor to understand the unsteady aerodynamic and control mechanism of flapping wings is to develop a simplified model predicting the aerodynamic forces as a function of the airfoil motion parameters.

This section is divided in three parts. The first part defines a simplified model of forces developed in a parallel project [Moriche et al., 2016]. The second part evaluates the performance of this model for the analysed cases under this work. And the last part of this project varies the value of the coefficient, of which the model is dependent, to optimize the results for each case to find the influence of the key parameters Re, θ_m and θ_0 on these free parameters.

4.2.1 Definition of the model

The model studied in this section was developed in the parallel project [Moriche et al., 2016], which introduces a modification on the model proposed in [Pesavento and Wang, 2004]. Firstly, this simplified model is defined. It tries to replicate the unsteady aerodynamic problem with a quasi-stationary model of forces acting on the airfoil.

The force predicted by the model ($\vec{F}$) is divided in three terms, the added mass forces ($\vec{F}^a$), the circulatory forces ($\vec{F}^c$) and the viscous forces ($\vec{F}^v$). The viscous forces ($\vec{F}^v$) can be neglected because they are small in comparison with the other terms. So to define the model, the added mas forces and the circulatory forces must be modelled.

$$F_x = F_x^a + F_x^c + F_x^v \approx F_x^a + F_x^c \tag{4.9a}$$
$$F_z = F_z^a + F_z^c + F_z^v \approx F_z^a + F_z^c \tag{4.9b}$$

Added-mass Forces

The added mass forces in the global coordinate system are:

$$F_x^a = X_0^a \cos(\theta) + Z_0^a \sin(\theta) \tag{4.10a}$$
$$F_z^a = -X_0^a \sin(\theta) + Z_0^a \cos(\theta) \tag{4.10b}$$

where X_0^a and Y_0^a are the added mass force components normal to the wing as defined in [Sane and Dickinson, 2002]:

$$X_0^a = -\lambda_x \frac{dU_0}{dt} - \lambda_{xz} \frac{dV_0}{dt} - \lambda_{xw} \frac{d\Omega}{dt} + \Omega(\lambda_{xz} U_0 + \lambda_z V_0 + \lambda_{zw} \Omega) \tag{4.11a}$$
$$Z_0^a = -\lambda_{xz} \frac{dU_0}{dt} - \lambda_z \frac{dV_0}{dt} - \lambda_{zw} \frac{d\Omega}{dt} - \Omega(\lambda_x U_0 + \lambda_{xz} V_0 + \lambda_{xw} \Omega) \tag{4.11b}$$

where λ_* are the given coefficients for the virtual masses from [Sedov et al., 1965] and U_0, V_0 and Ω are the transitional velocity components and angular velocity respectively of the center of gravity of the airfoil in a reference frame fixed to the airfoil.

For a symmetric Joukowsky airfoil, the λ_* coefficients are:

$$\lambda_{xz} = \lambda_{xw} = 0 \tag{4.12a}$$

$$\lambda_x = \phi\pi\frac{a^2}{4}(l-2)(l+1) \tag{4.12b}$$

$$\lambda_z = \phi\pi\frac{a^2}{4}[4+(l-2)(l+1)] \tag{4.12c}$$

$$\lambda_{zw} = \phi\pi\frac{a^3}{16}l(2l^2-l+2) \tag{4.12d}$$

$$\lambda_w = \phi\pi\frac{a^4}{32}l^2(2l^2+1) \tag{4.12e}$$

where ξ is the position of the center of gravity from the leading edge and l and a are geometric quantities depending on the airfoil. For similarity with this work, the selected parameter are the ones that generate an airfoil of $e_{MAX}/c = 0.12$:

$$a = 0.4499c \tag{4.13a}$$

$$l = c/a \tag{4.13b}$$

$$\xi = c - \frac{al}{4}(1+\frac{l^2}{l^2-l+2}) \tag{4.13c}$$

On the other hand, the local velocity and rotation are given by:

$$U_0 = -U_\infty\cos(\theta) - \dot{h}\sin(\theta) \tag{4.14a}$$

$$V_0 = -U_\infty\sin(\theta) + \dot{h}\cos(\theta) - \dot{\theta}(\xi - x_p) \tag{4.14b}$$

$$\Omega = -\dot{\theta} \tag{4.14c}$$

And their time derivatives:

$$\frac{dU_0}{dt} = U_\infty\dot{\theta}\sin(\theta) - \ddot{h}\sin(\theta) - \dot{h}\dot{\theta}\cos(\theta) \tag{4.15a}$$

$$\frac{dV_0}{dt} = -U_\infty\dot{\theta}\cos(\theta) + \ddot{h}\cos(\theta) - \dot{h}\dot{\theta}\sin(\theta) - \ddot{\theta}(\xi - x_p) \tag{4.15b}$$

$$\frac{d\Omega}{dt} = -\ddot{\theta} \tag{4.15c}$$

where θ and h are the pitching and heaving motions defined in eq 3.3 and eq 3.2, $\dot{\theta}$ and $\dot{h}$ are their first time derivatives defined in eq 4.17 and eq 4.16 and $\ddot{\theta}$ and $\ddot{h}$ are their second

time derivatives:

$$\ddot{h} = -h_0(2\pi f)^2 \cos(2\pi f t) \tag{4.16}$$

$$\ddot{\theta} = -\theta_0(2\pi f)^2 \cos(2\pi f t + \phi) \tag{4.17}$$

Circulatory Forces

The circulatory component of the force is reconstructed from the circulation according to Kutta-Joukowsky theorem:

$$\vec{F}_{KJ} = \rho \vec{V} \times \Gamma \vec{e_j} \tag{4.18}$$

where V_x and V_z are the components of the velocity of the fluid seen by the airfoil:

$$V_x = U_\infty \tag{4.19a}$$

$$V_z = -\dot{h} \tag{4.19b}$$

and where the circulation Γ is estimated from the modelization of [Pesavento and Wang, 2004] as follows:

$$\Gamma = \frac{1}{2} C_v c \mid \vec{V} \mid \sin(2\alpha_e) + \frac{1}{2} C_\theta c^2 \dot{\theta} \tag{4.20}$$

leaving C_θ and C_v as free parameters.

Therefore, the circulation force components can be expressed as:

$$F_{KJx} = \rho \dot{h} \Gamma \tag{4.21a}$$

$$F_{KJz} = \rho U_\infty \Gamma \tag{4.21b}$$

However in [Moriche et al., 2016] is proposed that the circulatory component of the force predicted by Kutta-Joukowsky theorem is tilted by an angle $\beta = \alpha_e$, which means that the force is normal to the airfoil instead of normal to the stream seen by the airfoil, leaving the previous equations in:

$$F_x^c = F_{KJx} \cos(\alpha_e) + F_{KJz} \sin(\alpha_e) \tag{4.22a}$$

$$F_z^c = F_{KJx} \sin(\alpha_e) + F_{KJz} \cos(\alpha_e) \tag{4.22b}$$

In [Moriche et al., 2016], the free parameter are selected by means of the optimization of the results for simulations with $Re = 1000$, $k = 1.41$, $\theta_0 = 30°$ and $h/c = 1$ varying θ_m and ϕ. Their values are $C_v = 1.6$ and $C_\theta = 3.5$.

For this selection of parameters, it must be taken into account that:

- The effects of Re are not reflected in this model, neither in modelled added mass forces nor in modelled circulatory forces.
- For a flapping motion with zero pitching amplitude ($\theta_0 = 0°$), the free parameter C_θ has not influence in the modelled circulation.
- For a pure heaving motion ($\theta(t) = 0°$), the modelled total force is normal to the airfoil, so the modelled streamwise force component is always zero.

4.2.2 Evaluation of model

This section evaluates the performance of the model described in the previous section for the cases studied in this work by means of a comparison with the results obtained in DNS. Two options of the simplified model are examined, the first defining the circulatory term of forces by means of the Kutta-Joukowski model [Pesavento and Wang, 2004] and the second one defining this term with the correction in the circulatory force direction [Moriche et al., 2016] with $C_v = 1.6$ and $C_\theta = 3.5$.

The following figures show the comparison between the results obtained from DNS and the ones obtained from the two models for both lift and thrust coefficients. This comparison is analysed only for four cases (B_{00a}, B_{00c}, B_{10b} and B_{10d}). The comparison for the remaining cases is shown in the Appendix of Chapter 8.

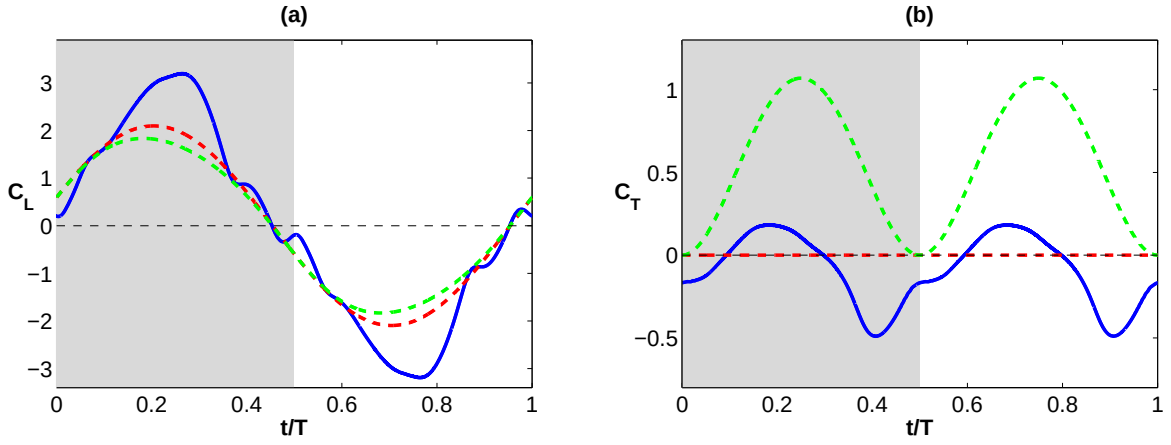

Figure 4.14: Results in one period of a) C_L b) C_T for case B_{00a} [$Re = 1000$, $\theta_m = 0°$, $\theta_0 = 0°$]. —— $\vec{F}_{DNS}$, - - - $\vec{F}^a + \vec{F}_{KJ}$, - - - $\vec{F}^a + \vec{F}^c$

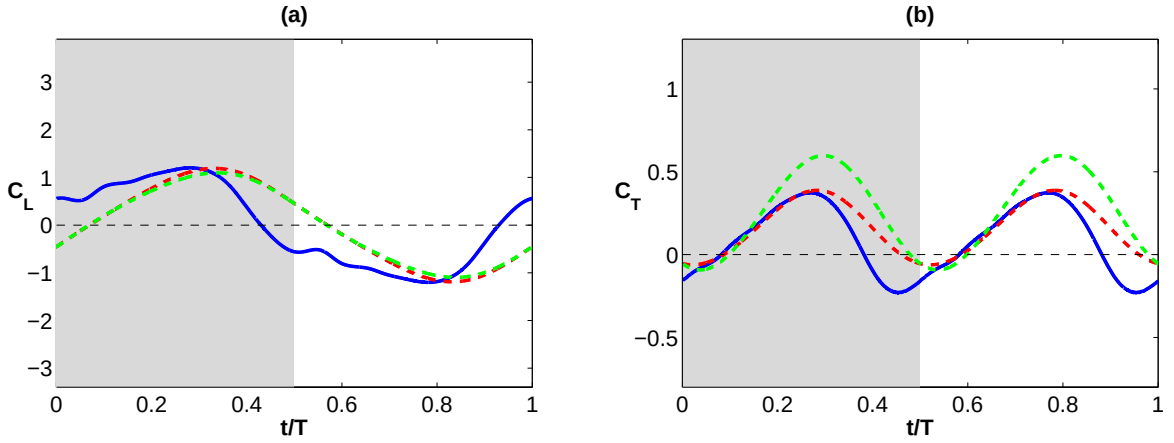

Figure 4.15: Results in one period of a) C_L b) C_T for case B_{00c} [$Re = 1000$, $\theta_m = 0°$, $\theta_0 = 20°$]. — $\vec{F}_{DNS}$, - - - $\vec{F}^a + \vec{F}_{KJ}$, - - - $\vec{F}^a + \vec{F}^c$

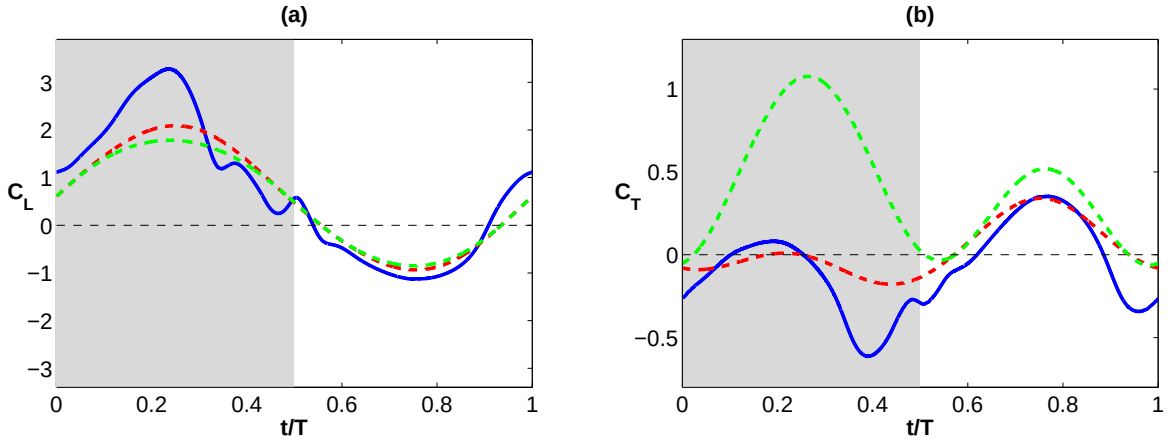

Figure 4.16: Results in one period of a) C_L b) C_T for case B_{10b} [$Re = 1000$, $\theta_m = 10°$, $\theta_0 = 10°$]. — $\vec{F}_{DNS}$, - - - $\vec{F}^a + \vec{F}_{KJ}$, - - - $\vec{F}^a + \vec{F}^c$

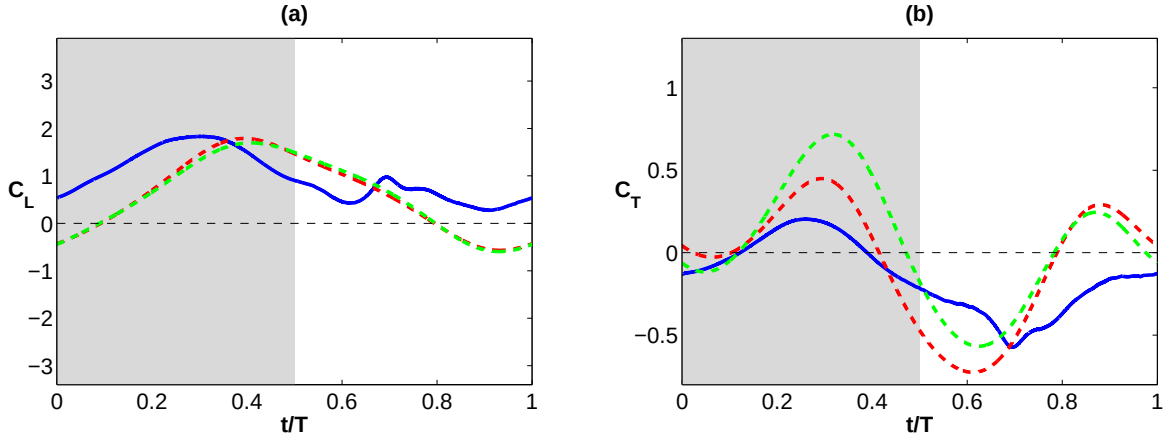

Figure 4.17: Results in one period of a) C_L b) C_T for case B_{10d} [$Re = 1000$, $\theta_m = 10°$, $\theta_0 = 30°$]. — $\vec{F}_{DNS}$, - - - $\vec{F}^a + \vec{F}_{KJ}$, - - - $\vec{F}^a + \vec{F}^c$

First of all, it can be seen that assuming that the circulatory forces are normal to the airfoil [Moriche et al., 2016] instead of normal to stream flow [Pesavento and Wang, 2004], the simplified model is more accurate to the DNS results for all the analysed cases.

Focusing in the model proposed by [Moriche et al., 2016], depending on the flapping configuration, different performances of this model are obtained. In Figure 4.14, for a pure heaving motion, the modelled forces are normal to the airfoil so the modelled thrust coefficient is always zero, a result completely different to the obtained in DNS. So, for pure heaving motion, the simplified model is not useful at all. Also, there exist another flapping configurations in which the performance of the simplified model is inadequate. For example, it can be appreciated in case B_{10d} (Figure 4.17), with $Re = 1000$, $\theta_m = 10°$, and $\theta_0 = 30°$, that the results are very imprecise, where the predicted thrust forces double the obtained in DNS and the lift forces have a large phase shift. It must be highlighted that this flapping configuration is exactly the same to the used one for the optimization in [Moriche et al., 2016] except for the reduced frequency, which is less than half. It follows that the flapping frequency has an important influence on the selection of the coefficients C_v and C_θ.

However, for some of the analysed cases the model is considerably precise. In case B_{00c} (Figure 4.15), with $Re = 1000$, $\theta_m = 0°$, and $\theta_0 = 20°$, the predicted thrust forces are very close to the obtained from DNS while the lift forces have a small phase shift. Also, in case B_{10b} (Figure 4.16), with $Re = 1000$, $\theta_m = 10°$, and $\theta_0 = 10°$, both the predicted lift and thrust forces follow closely the DNS results in the most part of the motion period.

Also, as it was seen in previous section, the lift and thrust coefficients obtained from DNS varying with Re. In these models the effects of Re are not included. Therefore, the predicted aerodynamic forces will not change by varying the Reynolds numbers, as it can be seen in the the following figure:

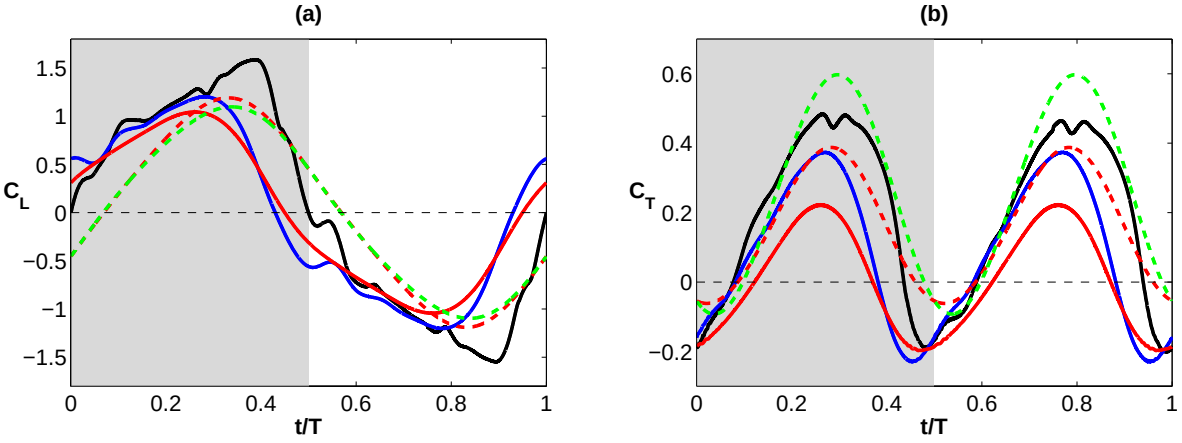

Figure 4.18: Results in one period for the cases with fixed $\theta_m = 0°$ and $\theta_0 = 20°$ at different Re of a) C_L b) C_T. — F_{DNS} $[C_{00c}]$, — F_{DNS} $[B_{00c}]$, — F_{DNS} $[A_{00c}]$, - - - $\vec{F}^a + \vec{F}_{KJ}$, - - - $\vec{F}^a + \vec{F}^c$

The following tables display the results for the mean ($\overline{C_{L_{DNS}}}$, $\overline{C_{L_{mod}}}$) and standard deviation ($\sigma_{C_{L_{DNS}}}$, $\sigma_{C_{L_{mod}}}$) of the lift and thrust coefficients obtained from DNS and simplified model of [Moriche et al., 2016], respectively. In addition, the error of the results obtained with the model (ϵ_{C_L}, ϵ_{C_T}) and their standard deviations ($\sigma_{\epsilon_{C_L}}$, $\sigma_{\epsilon_{C_T}}$) are included. The error is quantified as the root mean squared deviation between the force coefficients, normalized with the amplitude of the reference case:

$$\epsilon_{C_X} = \frac{\sqrt{\frac{1}{n}\sum_{i=1}^{n}(C_{Xref,i} - C_{Xi})^2}}{A_{C_{Xref}}} \tag{4.23}$$

where the sub-index x stands for lift or thrust coefficient. The force coefficients obtained in DNS are the references C_{Xref}, and $A_{C_{Xref}}$ are their amplitude values ($A_{C_{Xref}} = C_{Xmax} - C_{Xmin}$).

On the other hand, the standard deviation is defined as:

$$\sigma_{\epsilon_{C_X}} = \sqrt{\frac{1}{n}\sum_{i=1}^{n}(\epsilon_{C_{Xi}} - \overline{\epsilon_{C_X}})^2} = \sqrt{\frac{1}{n}\sum_{i=1}^{n}\left(\epsilon_{C_{Xi}} - \frac{1}{n}\sum_{i=1}^{n}(\epsilon_{C_{Xi}})\right)^2} \tag{4.24}$$

Case	$\overline{C_{L_{DNS}}}$	$\sigma_{C_{L_{DNS}}}$	$\overline{C_{L_{mod}}}$	$\sigma_{C_{L_{mod}}}$	ϵ_{C_L}	$\sigma_{\epsilon_{C_L}}$
$C_{10c,1}$	0.8679	0.9104	0.6160	0.7887	0.1523	0.2555
B_{10c}	0.6506	0.8608	0.6160	0.7887	0.1921	0.2648
A_{10c}	0.5008	0.7341	0.6160	0.7887	0.2687	0.3449
C_{10a}	0.3855	1.9897	0.4325	1.3796	0.1345	0.5028
B_{10a}	0.2534	2.0122	0.4325	1.3796	0.1245	0.4204
A_{10a}	0.3374	1.9410	0.4325	1.3796	0.1143	0.3926
C_{00c}	0.0384	1.0462	0.0000	0.8091	0.1175	0.1704
B_{00c}	0.0000	0.8367	0.0000	0.8091	0.2487	0.3223
A_{00c}	-0.0001	0.7252	0.0000	0.8091	0.2420	0.2484

Table 4.4: Comparison between lift coefficient mean ($\overline{C_{L_{DNS}}}$, $\overline{C_{L_{mod}}}$) and standard deviation ($\sigma_{C_{L_{DNS}}}$, $\sigma_{C_{L_{mod}}}$) of the results of DNS and model and mean (ϵ_{C_L}) and standard deviation (ϵ_{C_L}) of error of the cases analysed with different Reynolds numbers.

Case	$\overline{C_{L_{DNS}}}$	$\sigma_{C_{L_{DNS}}}$	$\overline{C_{L_{mod}}}$	$\sigma_{C_{L_{mod}}}$	ϵ_{C_L}	$\sigma_{\epsilon_{C_L}}$
B_{00a}	0.0010	1.9832	0.0000	1.4821	0.0973	0.4243
B_{00b}	-0.0004	1.5507	0.0000	1.1262	0.0967	0.2735
B_{00c}	0.0000	0.8367	0.0000	0.8091	0.2487	0.3223
B_{00d}	-0.0001	0.2523	0.0000	0.7883	0.7242	0.2587
B_{10a}	0.2534	2.0122	0.4325	1.3796	0.1245	0.4204
B_{10b}	0.6699	1.3852	0.5551	1.0573	0.1166	0.3054
B_{10c}	0.6506	0.8608	0.6160	0.7887	0.1921	0.2648
B_{10d}	0.9641	0.4953	0.6052	0.7838	0.4407	0.2772

Table 4.5: Comparison between lift coefficient mean ($\overline{C_{L_{DNS}}}$, $\overline{C_{L_{mod}}}$) and standard deviation ($\sigma_{C_{L_{DNS}}}$, $\sigma_{C_{L_{mod}}}$) of the results of DNS and model and mean (ϵ_{C_L}) and standard deviation ($\sigma_{\epsilon_{C_L}}$) of error of the cases analysed with different pitching amplitude.

Case	$\overline{C_{T_{DNS}}}$	$\sigma_{C_{T_{DNS}}}$	$\overline{C_{T_{mod}}}$	$\sigma_{C_{T_{mod}}}$	ϵ_{C_T}	$\sigma_{\epsilon_{C_T}}$
$C_{10c,1}$	-0.0307	0.2456	0.0413	0.1867	0.1678	0.0851
B_{10c}	-0.0649	0.2167	0.0413	0.1867	0.2164	0.1059
A_{10c}	-0.1294	0.1650	0.0413	0.1867	0.3470	0.1310
C_{10a}	-0.1061	0.3555	-0.0763	0.2402	0.1592	0.0982
B_{10a}	-0.1186	0.3516	-0.0763	0.2402	0.1722	0.0985
A_{10a}	-0.2004	0.3353	-0.0763	0.2402	0.2055	0.1277
C_{00c}	0.1925	0.2327	0.1571	0.1588	0.1398	0.0413
B_{00c}	0.0834	0.2033	0.1571	0.1588	0.2086	0.0931
A_{00c}	0.0061	0.1467	0.1571	0.1588	0.3893	0.0635

Table 4.6: Comparison between thrust coefficient mean ($\overline{C_{T_{DNS}}}$, $\overline{C_{T_{mod}}}$) and standard deviation ($\sigma_{C_{T_{DNS}}}$, $\sigma_{C_{T_{mod}}}$) of the results of DNS and model and mean (ϵ_{C_T}) and standard deviation ($\sigma_{\epsilon_{C_T}}$) of error of the cases analysed with different Reynolds numbers.

Case	$\overline{C_{T_{DNS}}}$	$\sigma_{C_{T_{DNS}}}$	$\overline{C_{T_{mod}}}$	$\sigma_{C_{T_{mod}}}$	ϵ_{C_T}	$\sigma_{\epsilon_{C_T}}$
B_{00a}	-0.0882	0.2097	0.0000	0.0000	0.3381	0.1347
B_{00b}	0.0867	0.2927	0.1332	0.1067	0.2329	0.0996
B_{00c}	0.0834	0.2033	0.1571	0.1588	0.2086	0.0931
B_{00d}	-0.0765	0.0766	0.0539	0.2443	0.9852	0.1265
B_{10a}	-0.1186	0.3516	-0.0763	0.2402	0.1722	0.0985
B_{10b}	-0.0787	0.2562	0.0292	0.1566	0.1845	0.1200
B_{10c}	-0.0649	0.2167	0.0413	0.1867	0.2164	0.1059
B_{10d}	-0.1460	0.2125	-0.0553	0.3658	0.3456	0.1440

Table 4.7: Comparison between thrust coefficient mean ($\overline{C_{T_{DNS}}}$, $\overline{C_{T_{mod}}}$) and standard deviation ($\sigma_{C_{T_{DNS}}}$, $\sigma_{C_{T_{mod}}}$) of the results of DNS and model and mean (ϵ_{C_T}) and standard deviation ($\sigma_{\epsilon_{C_T}}$) of error of the cases analysed with different pitching amplitude.

First of all, although this model is not useful for some flapping configurations as pure heaving, the results for the majority of cases are accurate. Also, it must be taken into account that the model was optimized for different flapping configurations. For that, the accuracy obtained for this simplified model is much more higher than the expected one.

From previous tables, it can be drawn some conclusions about the performance of the simplified model. As it was explained before, the model does not take into account the Re, so it should be adjusted to the variation of Re. With respect to thrust generation, by decreasing the Re results in higher error in the model. For example, with fixed $\theta_m = 0°$ and $\theta_0 = 20°$, at $Re = 3000$ the error is 14%, at $Re = 1000$ it increases up to 21% and at $Re = 500$ it increases up to 39%. Therefore, in term of thrust generation, the model is more precise at higher Re. It must be noticed that the values of C_v and C_θ are optimized in [Moriche et al., 2016] for cases with $Re = 1000$. Another interesting point is that, the results of both DNS and model show that there exists an optimum value of θ_0 maximizing the integrated value of the thrust coefficient in a motion period as it can be seen in Figure 4.19

Regarding the lift coefficient, apparently, there is not a clear tendency in the variation of the error with the value of Re. However, it can be appreciated that increasing θ_0 results in higher error in lift coefficient. For the cases with fixed $Re = 1000$ and $\theta_m = 10°$, with a θ_0 of $0°$ and $10°$ the error is conserved around 12%, but increasing θ_0 to $20°$ the error increases up to 19%, and for $\theta_0 = 30°$ the error increases up to 44%. Therefore, in term of lift generation, the model is more precise at lower θ_0.

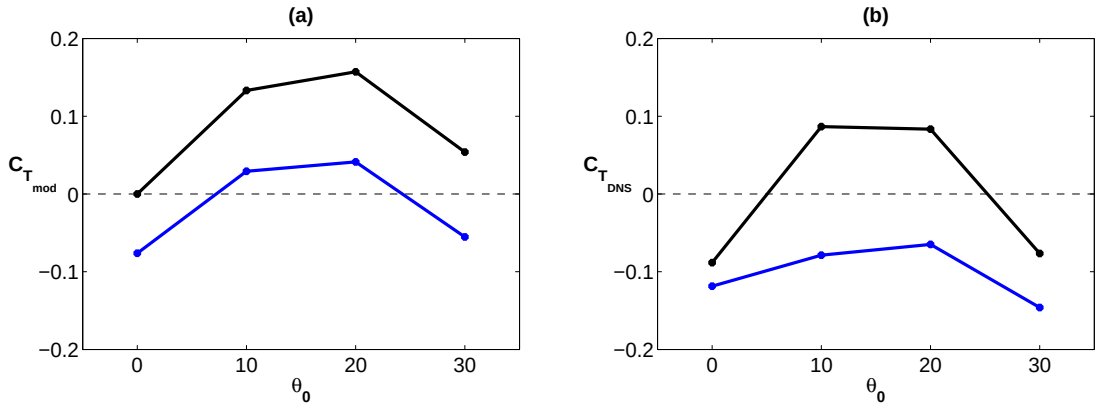

Figure 4.19: Variation with pitching amplitude for cases with $Re = 1000$ at different θ_m of a) $\overline{C_{T_{mod}}}$ b) $\overline{C_{T_{DNS}}}$. $\theta_m = 0°$, $\theta_m = 10°$.

4.2.3 Optimization of model

At this section, the objective is to vary the value of coefficients (C_T, C_R) to optimize the results for each case to find the influence of the Re, θ_m and θ_0 on those free parameters. The selected coefficients are those that give the lower error magnitude (ϵ_T), defined as the square root of the sum of the error in lift and thrust coefficients to square:

$$min(\epsilon_T) = min\left(\sqrt{[\epsilon_{C_L}]^2 + [\epsilon_{C_T}]^2}\right) \tag{4.25}$$

Firstly, the variation of the influence of C_v and C_θ on the error (ϵ_T) is analysed to find the influence of Re, θ_m and θ_0 on them.

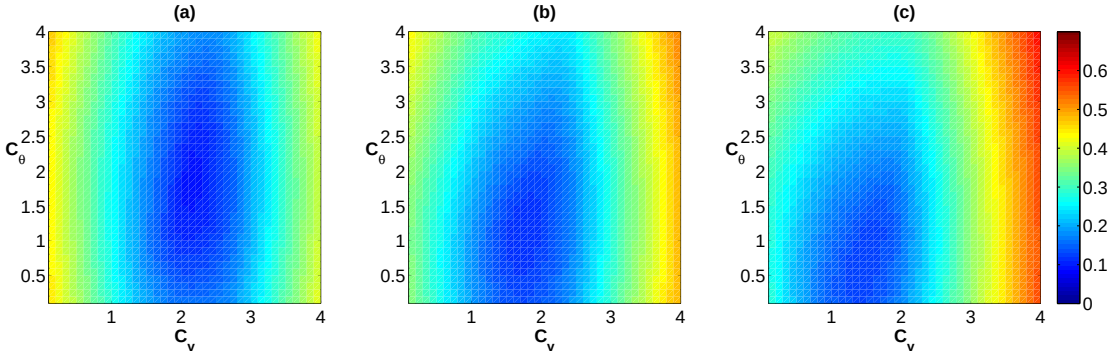

Figure 4.20: Influence of C_v and C_θ values on the total magnitude error between the results of DNS and model (ϵ_T) for cases with different Re at fixed $\theta_m = 10°$ and $\theta_0 = 20°$.
a) $C_{10c,1}$ [$Re = 3000$], b) B_{10c} [$Re = 1000$], c) A_{10c} [$Re = 500$].

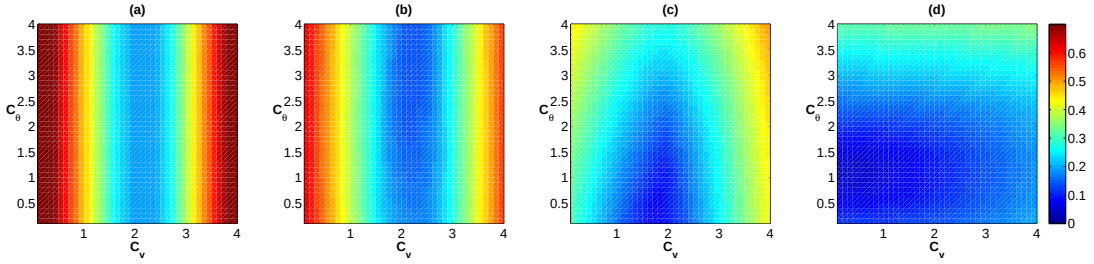

Figure 4.21: Influence of C_v and C_θ values on the total magnitude error between the results of DNS and model (ϵ_T) for cases with different θ_0 at fixed $Re = 1000$ and $\theta_m = 0°$.
a) B_{00a} [$\theta_0 = 0°$], b) B_{00b} [$\theta_0 = 10°$], c) B_{00c} [$\theta_0 = 20°$], d) B_{00d} [$\theta_0 = 30°$].

In Figure 8.14 is analysed the influence of C_θ and C_v on the error for the cases $C_{10c,1}$, B_{10c} and A_{10c}. From this figure it can be appreciated that increasing the Re the influence of C_θ increase, but the C_v influence remains the same. In Figure 8.16 the analysed cases are B_{00a}, B_{00b}, B_{00c} and B_{00d}. From this figure it can be noticed that for pure heaving (B_{00a}) C_θ does not influence in the results. Albeit, increasing the pitching amplitude, the influence of C_θ increases significantly while the influence of C_v decreases substantively.

Secondly, it is analysed the influence of Re, θ_m and θ_0 in the value of the obtained optimum coefficients. Figure 4.22 shows the variation of those parameters with Re at different flapping configurations and Figure 4.23 displays the variations with θ_0.

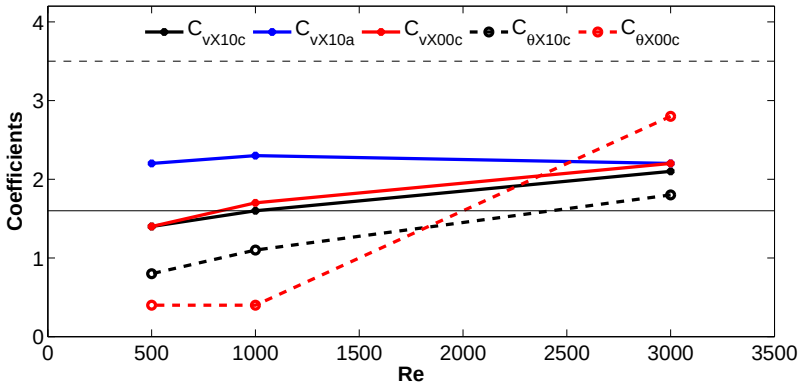

Figure 4.22: Variation of optimum value of free parameters C_v and C_θ with Re at fixed θ_m and θ_0. C_v $[\theta_m = 10°, \theta_0 = 20°]$, C_v $[\theta_m = 10°, \theta_0 = 0°]$, C_v $[\theta_m = 0°, \theta_0 = 20°]$, C_θ $[\theta_m = 10°, \theta_0 = 20°]$, C_θ $[\theta_m = 10°, \theta_0 = 0°]$, C_θ $[\theta_m = 0°, \theta_0 = 20°]$, —— C_v fixed, - - - C_θ fixed.

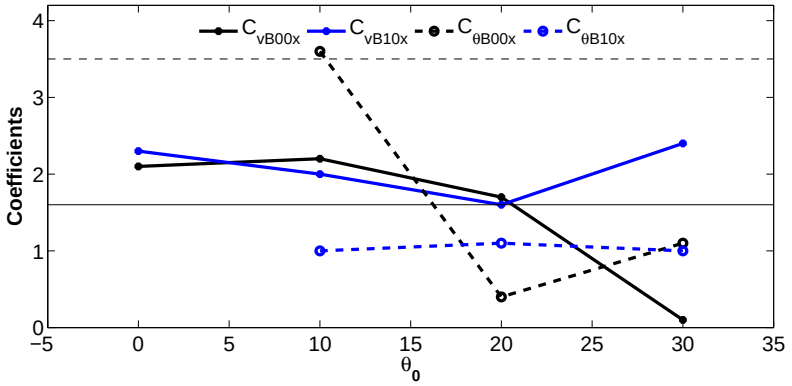

Figure 4.23: Variation of optimum value of free parameters C_v and C_θ with θ_0 at fixed $Re = 1000$ and θ_m. C_v $[\theta_m = 0°]$, C_v $[\theta_m = 10°]$, C_θ $[\theta_m = 0°]$, C_θ $[\theta_m = 10°]$, —— C_v fixed, - - - C_θ fixed.

The results obtained are not conclusive. From Figure 4.22 it can be appreciated that for the cases with non-zero pitching amplitude, by increasing Re the value of C_θ must apparently be increased to optimize the model, but the value of optimum C_v varies slightly. Similarly, from Figure 4.22, by increasing θ_0 there are not a clear trend in the evolution of the coefficients.

Thirdly, in the following figures the lift and thrust coefficients obtained from the model with the optimized coefficients are compared to the ones for the model with fixed parameters and the ones obtained from DNS. This comparison is performed on the cases analysed in previous section (B_{00a}, B_{00c}, B_{10b}, B_{10d}). The comparison of the remaining cases is displayed in Appendix of Chapter 8.

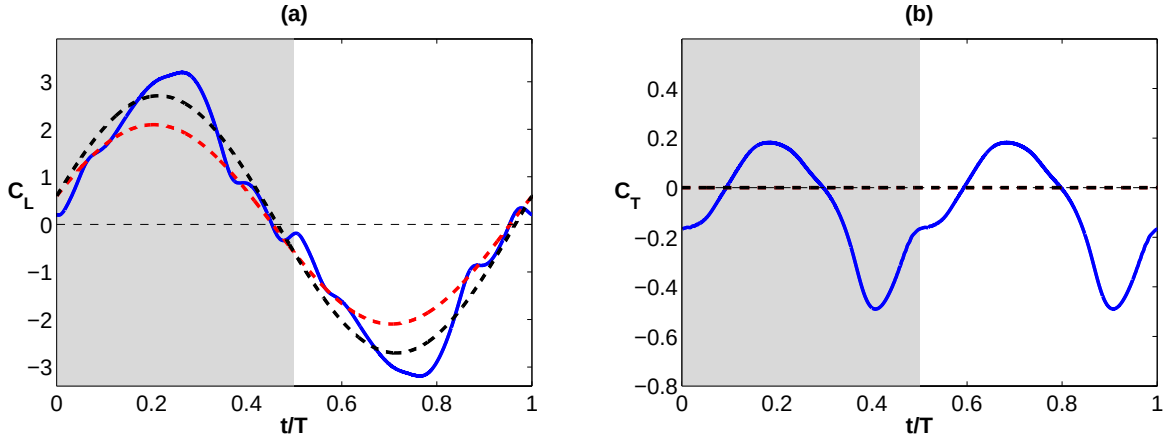

Figure 4.24: Results in one period of a) C_L b) C_T for case B_{00a} [$Re = 1000$, $\theta_m = 0°$, $\theta_0 = 0°$]. —— $\vec{F}_{DNS}$, - - - $\vec{F}_{mod}$, - - - $\vec{F}_{opt}$

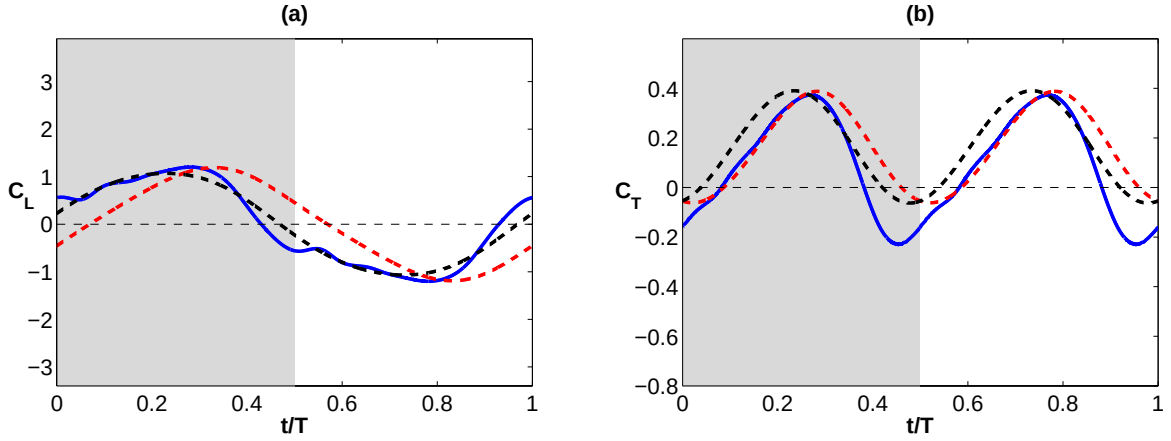

Figure 4.25: Results in one period of a) C_L b) C_T for case B_{00c} [$Re = 1000$, $\theta_m = 0°$, $\theta_0 = 20°$]. —— $\vec{F}_{DNS}$, - - - $\vec{F}_{mod}$, - - - $\vec{F}_{opt}$

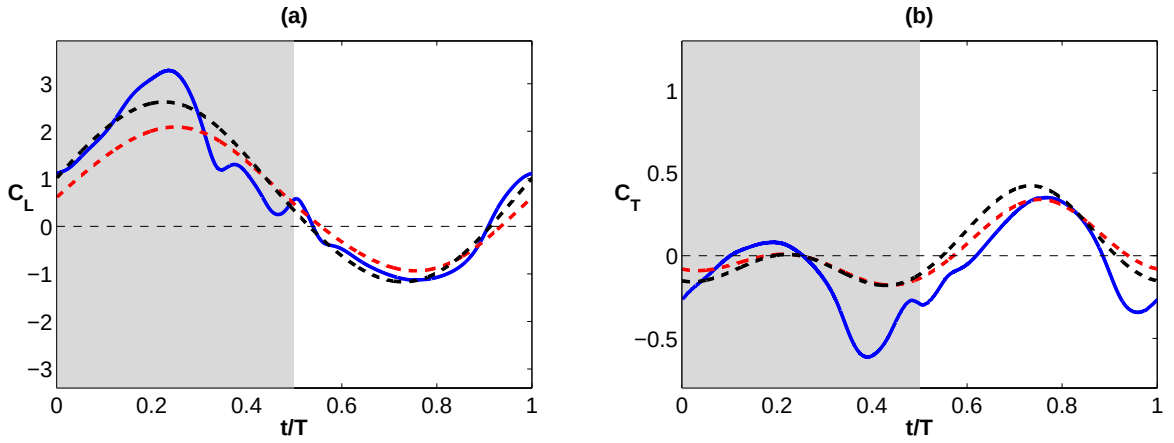

Figure 4.26: Results in one period of a) C_L b) C_T for case B_{10b} [$Re = 1000$, $\theta_m = 10°$, $\theta_0 = 10°$]. —— $\vec{F}_{DNS}$, - - - $\vec{F}_{mod}$, - - - $\vec{F}_{opt}$

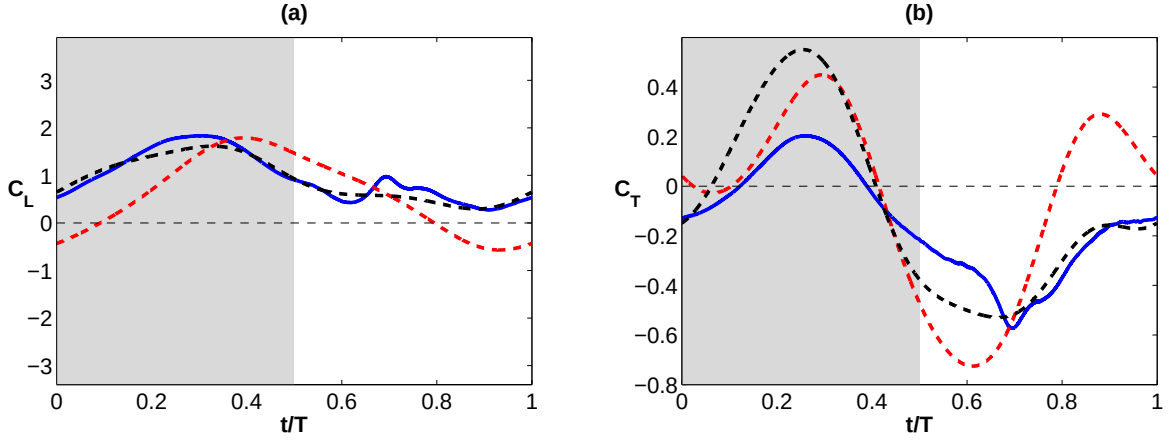

Figure 4.27: Results in one period of a) C_L b) C_T for case B_{10d} [$Re = 1000$, $\theta_m = 10°$, $\theta_0 = 30°$]. —— $\vec{F}_{DNS}$, - - - $\vec{F}_{mod}$, - - - $\vec{F}_{opt}$

First of all, it can be noticed that the value of the coefficients C_v and C_θ has not influence on the fact that for a pure heaving motion the force predicted by the model are normal to the airfoil, so the predicted thrust is always zero, a completely wrong result.

Also, it must be taken into account that in the optimization, the minimized error is weighted in the value of both lift and thrust errors. For that, as the values of lift coefficients are much higher than the thrust coefficients, and consequently the error magnitude in lift is higher than in thrust, the correction in lift coefficient error predominates. This can be appreciated in all the previous results. The accuracy in the predicted lift coefficients is extremely high for all the analysed cases even though the thrust coefficient is not properly adjusted.

Although the simplicity of this model makes that some cases like pure heaving motion cannot be predicted, those results highlights that the potential of this simplified model is very high. It has been shown that the model can achieve very close results to the obtained in DNS.

Finally, the following tables show the results for the mean ($\overline{C_{L_{DNS}}}$, $\overline{C_{L_{opt}}}$) and standard deviation ($\sigma_{C_{L_{DNS}}}$, $\sigma_{C_{L_{opt}}}$) of the lift and thrust coefficients obtained from DNS and optimized model, respectively. In addition, the error of the results obtained with the optimized model (ϵ_{C_L}, ϵ_{C_T}) and their standard deviations ($\sigma_{\epsilon_{C_L}}$, $\sigma_{\epsilon_{C_T}}$) are included.

Case	$\overline{C_{L_{DNS}}}$	$\sigma_{C_{L_{DNS}}}$	$\overline{C_{L_{opt}}}$	$\sigma_{C_{L_{opt}}}$	ϵ_{C_L}	$\sigma_{\epsilon_{C_L}}$
$C_{10c,1}$	0.8679	0.9104	0.8085	0.8994	0.0667	0.1299
B_{10c}	0.6506	0.8608	0.6160	0.7088	0.1065	0.2353
A_{10c}	0.5008	0.7341	0.5390	0.6379	0.1240	0.2154
C_{10a}	0.3855	1.9897	0.5947	1.8574	0.1034	0.3617
B_{10a}	0.2534	2.0122	0.6217	1.9379	0.1041	0.4464
A_{10a}	0.3374	1.9410	0.5946	1.8575	0.1010	0.4199
C_{00c}	0.0384	1.0462	0.0000	0.9878	0.0678	0.1225
B_{00c}	0.0000	0.8367	0.0000	0.7762	0.0766	0.1197
A_{00c}	-0.0001	0.7252	0.0000	0.6627	0.0442	0.0539

Table 4.8: Comparison between lift coefficient mean ($\overline{C_{L_{DNS}}}$, $\overline{C_{L_{opt}}}$) and standard deviation ($\sigma_{C_{L_{DNS}}}$, $\sigma_{C_{L_{opt}}}$) of the results of DNS and optimized model and mean ($\overline{\Delta_{CL}}$) and standard deviation ($\sigma_{\Delta_{CL}}$) of error of the cases analysed with different Reynolds number.

Case	$\overline{C_{L_{DNS}}}$	$\sigma_{C_{L_{DNS}}}$	$\overline{C_{L_{OPT}}}$	$\sigma_{C_{L_{OPT}}}$	ϵ_{C_L}	$\sigma_{\epsilon_{C_L}}$
B_{00a}	0.0010	1.9832	0.0000	1.9125	0.0581	0.1776
B_{00b}	-0.0004	1.5507	0.0000	1.5276	0.0516	0.1314
B_{00c}	0.0000	0.8367	0.0000	0.7762	0.0766	0.1197
B_{00d}	-0.0001	0.2523	0.0000	0.2372	0.0452	0.0166
B_{10a}	0.2534	2.0122	0.6217	1.9379	0.1041	0.4464
B_{10b}	0.6699	1.3852	0.6938	1.3275	0.0728	0.2057
B_{10c}	0.6506	0.8608	0.6160	0.7088	0.1065	0.2353
B_{10d}	0.9641	0.4953	0.9078	0.4435	0.0997	0.0906

Table 4.9: Comparison between lift coefficient mean ($\overline{C_{L_{DNS}}}$, $\overline{C_{L_{opt}}}$) and standard deviation ($\sigma_{C_{L_{DNS}}}$, $\sigma_{C_{L_{opt}}}$) of the results of DNS and optimized model and mean ($\overline{\Delta_{CL}}$) and standard deviation ($\sigma_{\Delta_{CL}}$) of error of the cases analysed with different pitching amplitude.

Case	$\overline{C_{T_{DNS}}}$	$\sigma_{C_{T_{DNS}}}$	$\overline{C_{T_{opt}}}$	$\sigma_{C_{T_{opt}}}$	ϵ_{C_T}	$\sigma_{\epsilon_{C_T}}$
$C_{10c,1}$	-0.0307	0.2456	0.0542	0.1849	0.1464	0.0852
B_{10c}	-0.0649	0.2167	0.0413	0.1468	0.1831	0.0838
A_{10c}	-0.1294	0.1650	0.0361	0.1327	0.2931	0.0878
C_{10a}	-0.1061	0.3555	-0.1049	0.3252	0.1324	0.0901
B_{10a}	-0.1186	0.3516	-0.1096	0.3395	0.1536	0.0991
A_{10a}	-0.2004	0.3353	-0.1048	0.3252	0.1898	0.1332
C_{00c}	0.1925	0.2327	0.2160	0.1938	0.1109	0.0415
B_{00c}	0.0834	0.2033	0.1669	0.1602	0.1692	0.0515
A_{00c}	0.0061	0.1467	0.1375	0.1399	0.3229	0.0350

Table 4.10: Comparison between thrust coefficient mean ($\overline{C_{T_{DNS}}}$, $\overline{C_{T_{opt}}}$) and standard deviation ($\sigma_{C_{T_{DNS}}}$, $\sigma_{C_{T_{opt}}}$) of the results of DNS and optimized model and mean ($\overline{\Delta_{CT}}$) and standard deviation ($\sigma_{\Delta_{CT}}$) of error of the cases analysed with different Reynolds number.

Case	$\overline{C_{T_{DNS}}}$	$\sigma_{C_{T_{DNS}}}$	$\overline{C_{T_{OPT}}}$	$\sigma_{C_{T_{OPT}}}$	ϵ_{C_T}	$\sigma_{\epsilon_{C_T}}$
B_{00a}	-0.0882	0.2097	0.0000	0.0000	0.3381	0.1347
B_{00b}	0.0867	0.2927	0.1831	0.1422	0.2218	0.1140
B_{00c}	0.0834	0.2033	0.1669	0.1602	0.1692	0.0515
B_{00d}	-0.0765	0.0766	0.0034	0.1050	0.4547	0.0575
B_{10a}	-0.1186	0.3516	-0.1096	0.3395	0.1536	0.0991
B_{10b}	-0.0787	0.2562	0.0365	0.1923	0.1883	0.1092
B_{10c}	-0.0649	0.2167	0.0413	0.1468	0.1831	0.0838
B_{10d}	-0.1460	0.2125	-0.0829	0.3509	0.2259	0.1110

Table 4.11: Comparison between thrust coefficient mean ($\overline{C_{T_{DNS}}}$, $\overline{C_{T_{opt}}}$) and standard deviation ($\sigma_{C_{T_{DNS}}}$, $\sigma_{C_{T_{opt}}}$) of the results of DNS and optimized model and mean ($\overline{\Delta_{CT}}$) and standard deviation ($\sigma_{\Delta_{CT}}$) of error of the cases analysed with different pitching amplitude.

From previous tables it can be seen that the errors in lift coefficients are significantly reduced. In the most cases the error is lower than 10% in lift coefficient, and for example in cases B_{00d} and A_{00c} the differences are reduced to only 4%.

However, as explained before, the optimization is more weighted in the correction of lift coefficient error, therefore the corrections in thrust coefficient are smaller. Also, it must be taken into account that the optimization is made to minimize the differences between the time history results in lift and thrust coefficients. For that, although the results obtained can be closer, the integrated value of the force coefficients (the mean value) can be worst. For example, the $\overline{C_L}$ obtained in DNS for case B_{10a} is 0.3855 and the result for the optimized model is 0.5947. However for the model with fixed parameters, the predicted $\overline{C_L}$ is 0.4325, a closer result.

In conclusion, it has been checked that the model proposed by [Moriche et al., 2016] obtains more accurate results than the model of [Pesavento and Wang, 2004] for the analysed cases under this work. Note that the model is non useful for some flapping configurations as pure heaving, where the predicted forces are normal to the airfoil being the predicted thrust always zero, a completely wrong result. However, even though the model has a great simplicity, for the most cases the obtained results are close to the obtained ones in DNS. Also when this model is optimized, it is highlighted the enormous potential of this simplified model especially in lift generation, where the differences are reduced even up to 4%. However, the results obtained regarding the influence of Re, θ_m and θ_0 on the optimized coefficients C_v and C_θ are not conclusive. To strengthen understanding of this influence it must be performed a more specific analysis than the developed in this work. Also, the optimization should be more sophisticated.

Chapter 5

Project Planning

This chapter shows the followed planning for the development of this project. The elaboration of this project can be divided in four working phases. Figure 5.1 presents the Gantt chart of this project showing the work time distribution of those phases.

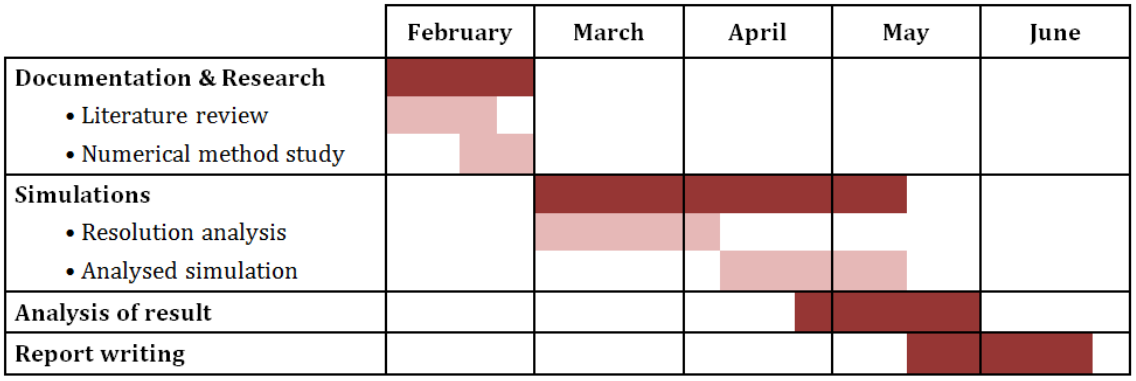

Figure 5.1: Gantt Chart of this project

- **Documentation and research**. This first phase, developed during the first month, is divided in two stages:
  - A literature review to acquire the needed information concerning flapping airfoils.
  - A study of the used numerical method in order to understand the background of flow solvers of unsteady aerodynamic problems.
- **Computation of simulations**. Once the numerical method had been understood, the first flapping motions were simulated with the in-house code TUCAN. This second phase, performed during the following two and a half months, is divided in two stages:
  - The computation of the first three simulations to perform a resolution analysis for cases with $Re = 3000$.

  - The simulation of the remaining cases to analyse the aerodynamic forces at different flapping configurations.

- **Analysis of results**. At the same time that the last cases were simulated, the resulting data of the cases already computed started to be analysed. This analysis was completed once all the cases was developed.

- **Report writing**. In the final phase the present report was written, collecting all the work performed in previous stages. This phase spanned until the end of the project.

Chapter 6

Regulatory and socioeconomic framework

6.1 Socioeconomic impact

The development of small autonomous flying machine used as aerial reconnaissance robots for inside buildings and confined spaces has focused many efforts in last years. Industry, commerce and the military have all identified potential roles for such micro-aerial vehicles (MAVs). Research on MAVs, conducted by aerodynamic and robotic engineers, are attempting to develop a design similar to those with much better aerodynamic performance than conventional wings and rotors; the small birds and insects.

However, the flapping wing flight of those animals is not yet properly understood. The main objective of this work is to contribute to the understanding of the unsteady aerodynamics of flapping wings and to the development of a simplified model predicting the aerodynamic forces as a function of the wing motion parameters. These are key factors to better understand the flapping wing flights to enhance the performance of bio-inspired MAVs.

This progress has the potential to bring about a huge impact in the aeronautical field resulting in a positive social, economic and industrial impact. MAVs applications span a very wide range, and the majority of them are military. MAVs are equipped with different sensors to perform intelligence, surveillance and reconnaissance missions in very challenging environments. This implies a positive impact in the aerospace industry and it economy as well as an important advance on military technology.

But also, those application involve a beneficial contribution to society. The development of very small robotic flying machines with the performance of an insect and equipped with cameras would be very helpful in rescue works for inspect unsafe or collapsed buildings after

disaster cases, such as earthquakes, hurricanes or collapsed mines. In these cases, locating survivors faster increases the probability of saving lives and the use of MAVs would decrease considerably the time necessary to explore those areas.

6.2 Regulatory framework

Regarding regulatory framework, no regulations apply for this project since actually it does not exist any specific rule on the creation, development, manufacture or use of micro-aerial vehicles. Furthermore, this project is a computational analysis with the objective to acquire a better understanding of the unsteady aerodynamics involving flapping airfoils. For that, even though there exists a current debate on the legal operating places for MAVs, these regulations most probably would not affect to this work.

6.3 Budget

This section shows the budget describing all the cost associated to this project. The cost attributed to this project are splitted into personnel, material and software costs. Table 6.1 displays each of them.

PERSONNEL EXPENSES

Item	Cost per hour [€/h]	Time [h]	Cost [€]
Engineering hours	20	500	**10000**

MATERIAL COSTS

Item	Price [€]	Use [h]	Lifespan [h]	Cost [€]
Laptop	650	2928	35064	**54.28**

SOFTWARE COSTS

Item	Use [h]	Cost per hour [€/h]	Cost [€]
CPU Costs	2820	0.2	**564**
MATLAB License	-	-	**500**

Table 6.1: Breakdown of the budget. Personnel, material and software costs.

- **Personnel expenses** reduce to the engineering hours, which have been estimated to be covered with a hourly salary of 20 €/h for the duration of this project.
- **Material costs** set the amortization cost of a needed laptop assuming a straight line depreciation. The laptop has been used 4 months and the estimated lifespan is 4 years.

$$Cost = \frac{Use}{Lifespan} \times Price \tag{6.1}$$

- **Software costs** are composed by the needed MATLAB Academic License [MATLAB] and the costs derived from the use of a computational center to perform the DNS. The last ones are estimated taking as reference the pricing of CESGA (Centro de Supercomputación de Galicia) [CESGA].

Finally, Table 6.2 summarizes the budget of this project showing the total costs.

TOTAL COST	
Personnel Expenses	10000 €
Material Costs	54.28 €
Software Costs	1064 €
Total Cost	11118.28 €

Table 6.2: Summary of the budget of this project.

Chapter 7

Conclusions

The main objective of this work is to contribute to the understanding of the unsteady aerodynamic of flapping wings. It is presented a numerical analysis of the flow around a plunging and pitching airfoil by means of Direct Numerical Simulation (DNS).

Firstly, it has been studied the aerodynamic performance of different flapping motions. This study shows the influence of three parameters, Re, θ_m and θ_0, on the mean and standard deviation and on the time history results of the aerodynamic force coefficients. Also the different formed wake structures are examined.

In this analysis, it was observed that for the analysed cases, by increasing Re leads to higher produced thrust. Cases with $\theta_m = 0°$ and $\theta_0 = 20°$, only with the increase of Re from 500 to 3000, the $\overline{C_T}$ increases from 0.01 to 0.19 and the η from 2% to 42%. Also, it was found that, for the analysed flapping configurations, there exists an optimum pitching amplitude in the θ_0 range from 0° to 30° maximizing the thrust generation. In addition, for cases with $\theta_m = 10°$ and $Re = 1000$, while the thrust is approximately the same with a θ_0 of 10° and 20°, the propulsive efficiency doubles from 12.7% with $\theta_0 = 10°$ to 24.1% with $\theta_0 = 20°$.

The intensity of the vorticity and associated pressure in the wake structures generated by the flapping motion increases considerably by increasing Re. Also, while in cases with zero pitching amplitude, the Re apparently has no influence in the creation of LEV and TEV, in cases with non-zero pitching amplitude, by increasing Re results in greater vortex structures generation. On the other hand, it was noticed that, for the flapping configurations analysed under this work, by increasing θ_0 results in lower effective angle of attack. This reduction in α_e produces the disappearance of vortex structures, resulting in lower lift generation. Also, it is highlighted that the case with $\theta_m = 10°$ and $\theta_0 = 30°$ at $Re = 1000$ generates lift both in upstroke and downstroke.

Finally, it was evaluated the performance of a simplified model for the simulated cases under this project. This model was developed in [Moriche et al., 2016] and it is used to predict the aerodynamic forces acting on the flapping airfoil. It was noticed that the model is non useful for some flapping motions like pure heaving, where the predicted forces are normal to the airfoil being the thrust component always zero, a completely wrong result. However, even though the model has a great simplicity, it is highlighted its enormous potential where, after the optimization, the differences in the most analysed cases are lower than 10% in lift generation. However, the results obtained regarding the influence of Re, θ_m and θ_0 on the model coefficients C_v and C_θ are not conclusive. To strengthen understanding of this influence it must be performed a more specific analysis than the developed in this work.

It must be taken into account that all the cases have the same reduced frequency ($k = 0.2\pi$), same plunging amplitude ($h/c = 1$) and same phase shift between pitching and plunging motions ($\phi = 90°$) for a NACA-0012 airfoil. It means that all the results obtained and the conclusions drawn from them are useful for similar parametric combinations than the used ones. Also, it must be noted that for cases with $Re = 3000$, a 3D study should be performed in order to check whether or not there are instabilities. However, the computational cost of these simulations would be too large for a project like this one. Albeit, the results obtained in this work are treated in order to analyse the tendencies with the variation of Re. For that, the possible presence of 3D instabilities does not affect to the analysis developed in this document.

For future projects, it would be important to realize the initial objective of this work, to validate the results obtained in DNS with the experimental analysis in a companion project. Even so, this project can be a starting point for future researches. Those studies can be focused in the analysis of the influence of other flapping parameters that are fixed in this work, like the flapping frequency or heaving amplitude. With these complementary analyses it will be possible to obtain a better understanding of the flapping parameter influences. Also, it would be interesting to perform a deeper study of the influence of a specific parameter in the aerodynamic forces. Regarding to the simplified model, it would be more conclusive to research the influence of a specific flapping parameter on the model coefficients C_v and C_θ, including a more sophisticated optimization precess.

Chapter 8

Appendix

8.1 Additional results for the evaluation of model

This section includes the comparison for all the analysed cases between the results obtained in DNS and in the two models, [Pesavento and Wang, 2004] and [Moriche et al., 2016], for the lift and thrust coefficients to complement the result shown in section 4.2.2.

8.1.1 Comparison varying the Reynolds number

Cases with $\theta_m = 10°$ and $\theta_0 = 20°$

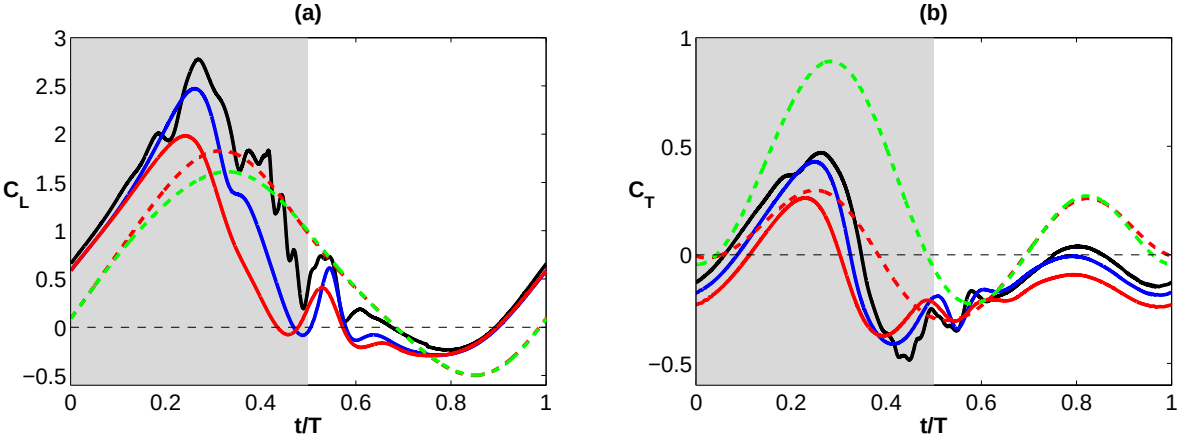

Figure 8.1: Results in one period for the cases with fixed $\theta_m = 10°$ and $\theta_0 = 20°$ at different Re of a) C_L b) C_T — F_{DNS} $[C_{10c,1}]$, — F_{DNS} $[B_{10c}]$, — F_{DNS} $[A_{10c}]$, - - - $\vec{F}^a + \vec{F}_{KJ}$, - - - $\vec{F}^a + \vec{F}^c$

Cases with $\theta_m = 10°$ and $\theta_0 = 0°$

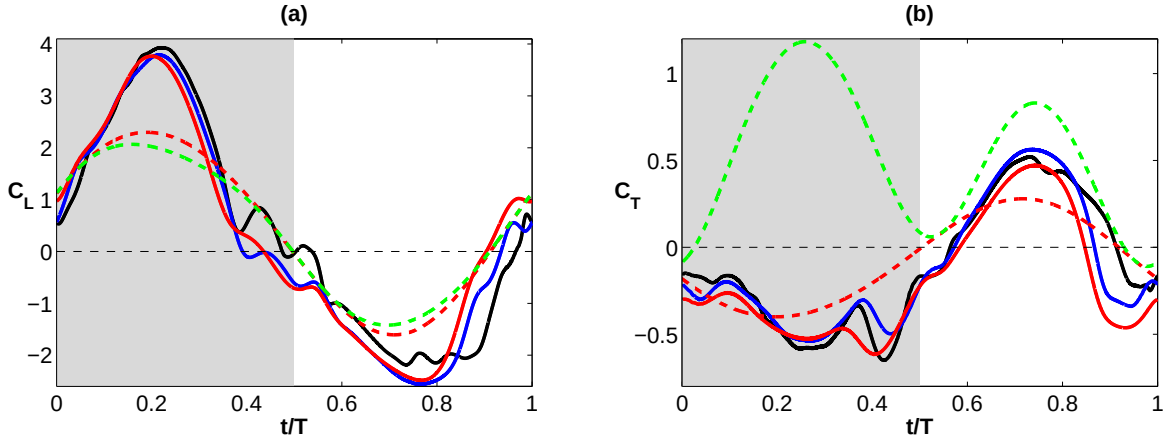

Figure 8.2: Results in one period for the cases with fixed $\theta_m = 10°$ and $\theta_0 = 0°$ at different Re of a) C_L b) C_T. — F_{DNS} $[C_{10a}]$, — F_{DNS} $[B_{10a}]$, — F_{DNS} $[A_{10a}]$, - - - $\vec{F}^a + \vec{F}_{KJ}$, - - - $\vec{F}^a + \vec{F}^c$

Cases with $\theta_m = 0°$ and $\theta_0 = 20°$

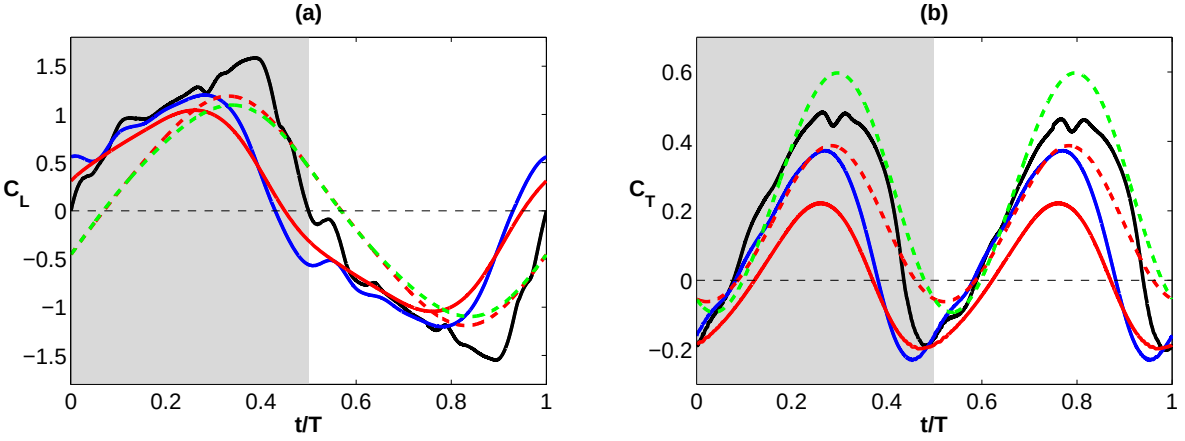

Figure 8.3: Results in one period for the cases with fixed $\theta_m = 0°$ and $\theta_0 = 20°$ at different Re of a) C_L b) C_T. — F_{DNS} $[C_{00c}]$, — F_{DNS} $[B_{00c}]$, — F_{DNS} $[A_{00c}]$, - - - $\vec{F}^a + \vec{F}_{KJ}$, - - - $\vec{F}^a + \vec{F}^c$

8.1.2 Comparison varying the pitching amplitude

Cases with $\theta_m = 0°$ and $Re = 1000$

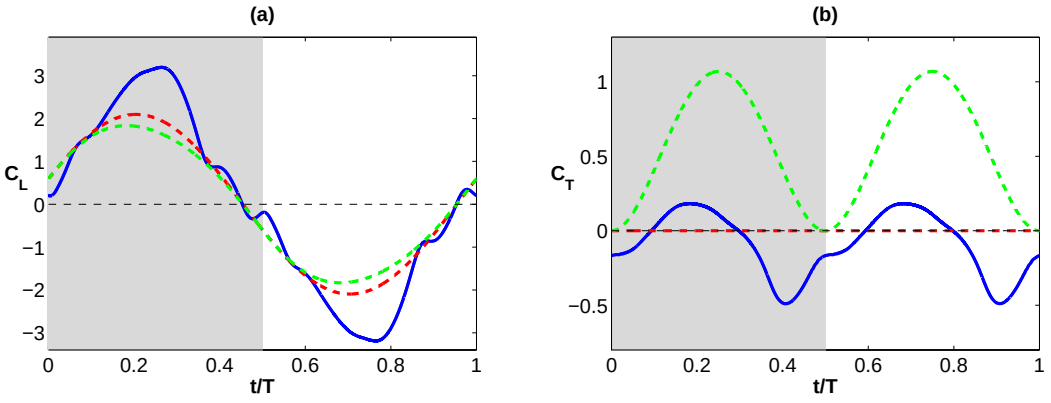

Figure 8.4: Results in one period of a) C_L b) C_T for case B_{00a} [$Re = 1000$, $\theta_m = 0°$, $\theta_0 = 0°$]. —— $\vec{F}_{DNS}$, - - - $\vec{F}^a + \vec{F}_{KJ}$, - - - $\vec{F}^a + \vec{F}^c$

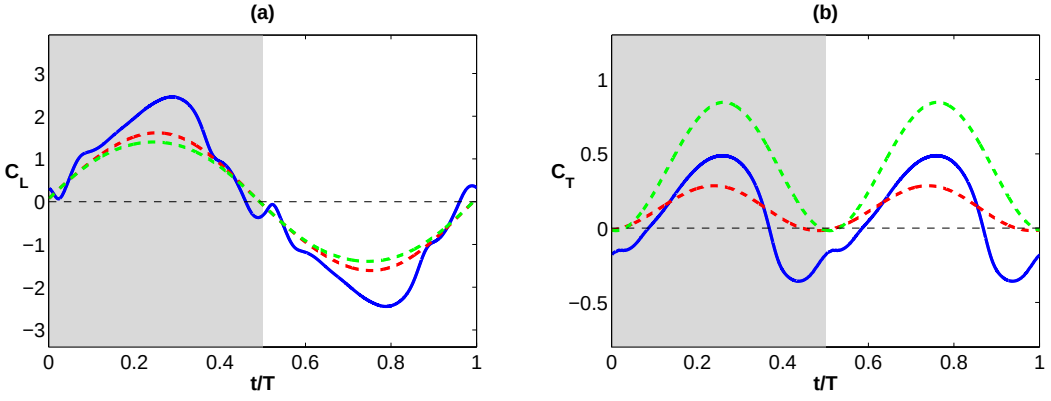

Figure 8.5: Results in one period of a) C_L b) C_T for case B_{00b} [$Re = 1000$, $\theta_m = 0°$, $\theta_0 = 10°$]. —— $\vec{F}_{DNS}$, - - - $\vec{F}^a + \vec{F}_{KJ}$, - - - $\vec{F}^a + \vec{F}^c$

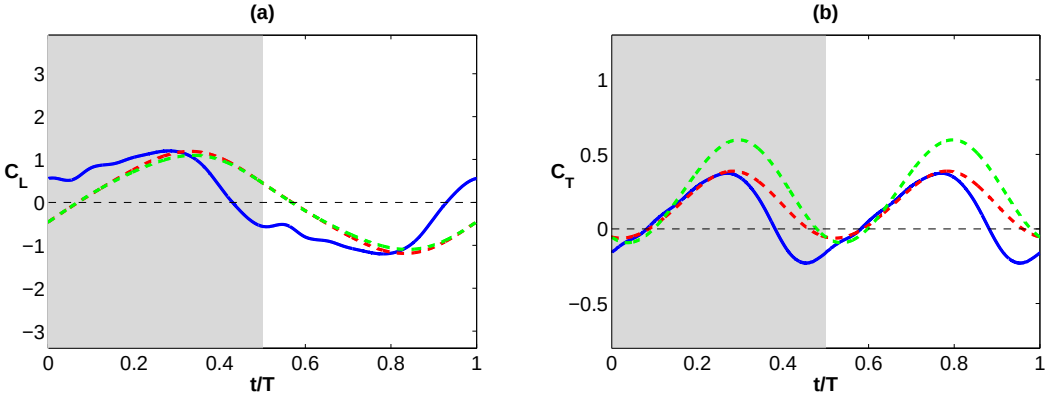

Figure 8.6: Results in one period of a) C_L b) C_T for case B_{00c} [$Re = 1000$, $\theta_m = 0°$, $\theta_0 = 20°$]. —— $\vec{F}_{DNS}$, - - - $\vec{F}^a + \vec{F}_{KJ}$, - - - $\vec{F}^a + \vec{F}^c$

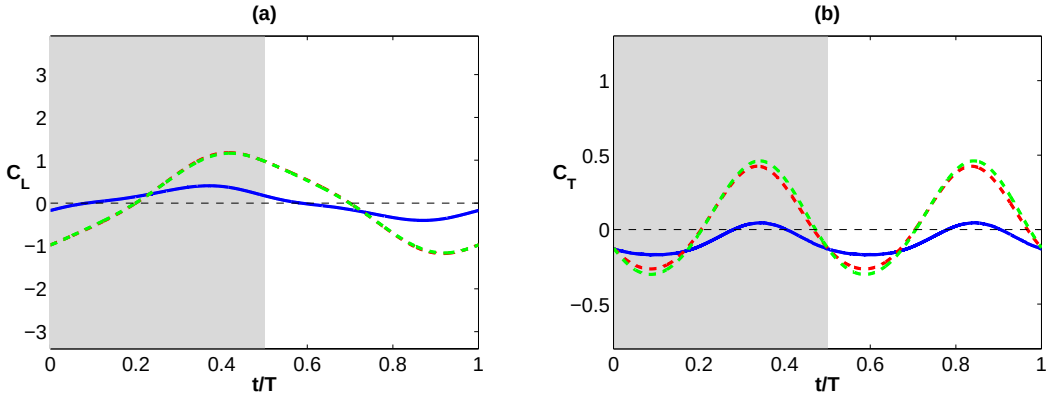

Figure 8.7: Results in one period of a) C_L b) C_T for case B_{00d} [$Re = 1000$, $\theta_m = 0°$, $\theta_0 = 30°$]. —— $\vec{F}_{DNS}$, - - - $\vec{F}^a + \vec{F}_{KJ}$, - - - $\vec{F}^a + \vec{F}^c$

Cases with $\theta_m = 10°$ and $Re = 1000$

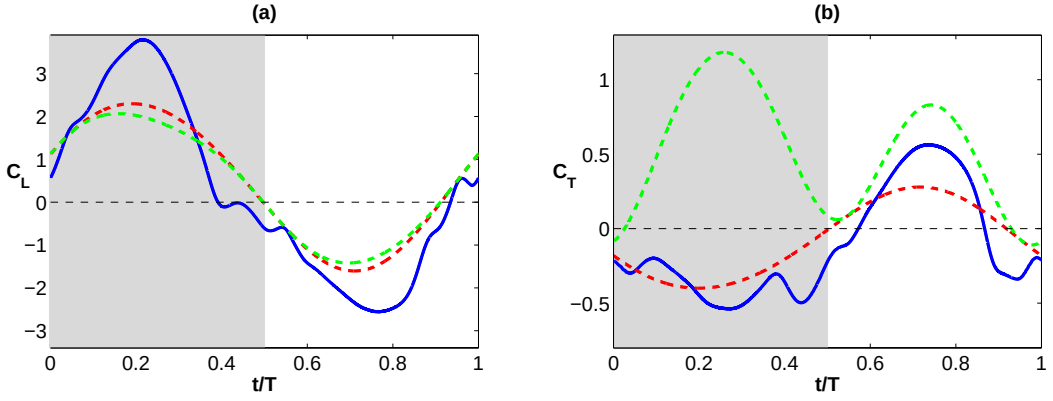

Figure 8.8: Results in one period of a) C_L b) C_T for case B_{10a} [$Re = 1000$, $\theta_m = 10°$, $\theta_0 = 0°$]. —— $\vec{F}_{DNS}$, - - - $\vec{F}^a + \vec{F}_{KJ}$, - - - $\vec{F}^a + \vec{F}^c$

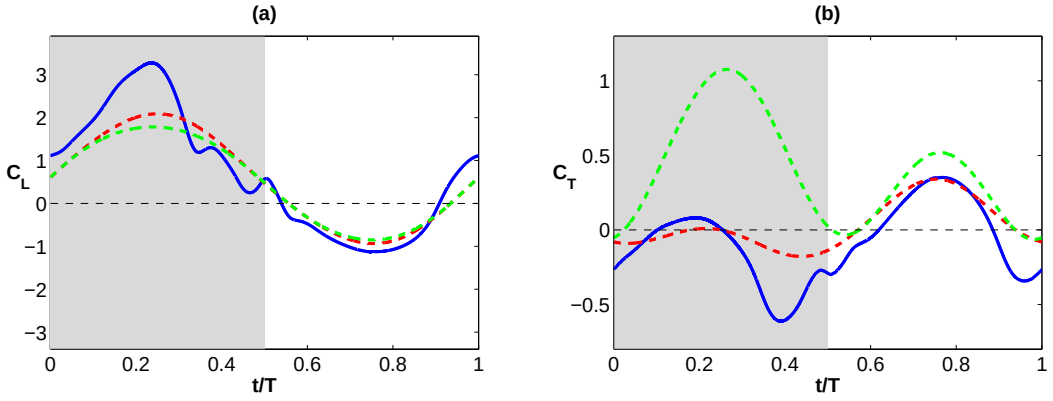

Figure 8.9: Results in one period of a) C_L b) C_T for case B_{10b} [$Re = 1000$, $\theta_m = 10°$, $\theta_0 = 10°$]. —— $\vec{F}_{DNS}$, - - - $\vec{F}^a + \vec{F}_{KJ}$, - - - $\vec{F}^a + \vec{F}^c$

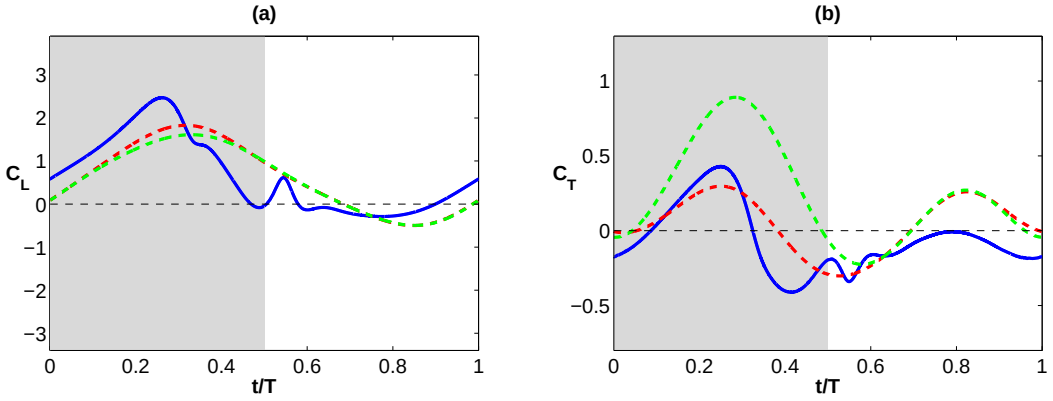

Figure 8.10: Results in one period of a) C_L b) C_T for case B_{10c} [$Re = 1000$, $\theta_m = 10°$, $\theta_0 = 20°$]. —— $\vec{F}_{DNS}$, - - - $\vec{F}^a + \vec{F}_{KJ}$, - - - $\vec{F}^a + \vec{F}^c$

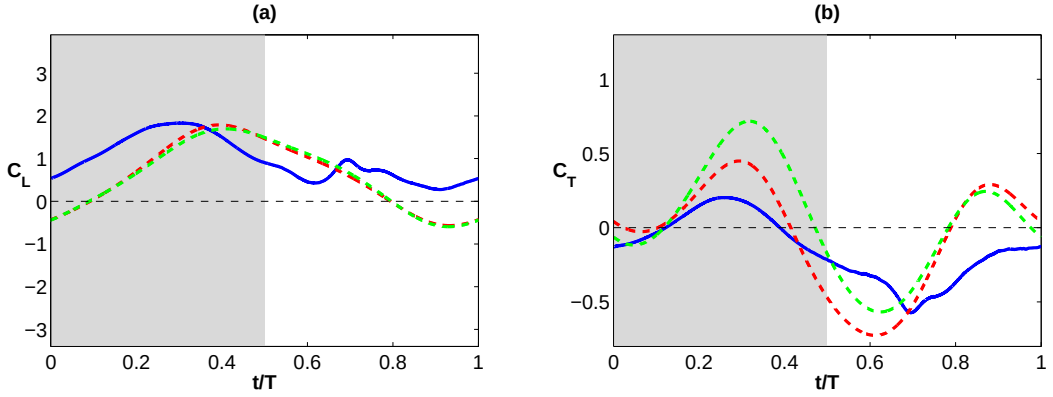

Figure 8.11: Results in one period of a) C_L b) C_T for case B_{10d} [$Re = 1000$, $\theta_m = 10°$, $\theta_0 = 30°$]. —— $\vec{F}_{DNS}$, - - - $\vec{F}^a + \vec{F}_{KJ}$, - - - $\vec{F}^a + \vec{F}^c$

8.2 Additional results for the optimization of model

This section includes the additional results obtained from the optimization of the model proposed by [Moriche et al., 2016] to complement the result shown in section 4.2.3. Firstly, it is displayed the results obtained for the variation of influence of C_v and C_θ on the error (ϵ_T) for all the analysed cases. Secondly, it is shown the comparison between the results of lift and thrust coefficients obtained in DNS and [Moriche et al., 2016] model with both fixed and optimized coefficients C_v and C_θ.

8.2.1 Influence of coefficients on error varying the Reynolds number

Cases with $\theta_m = 10°$ and $\theta_0 = 20°$

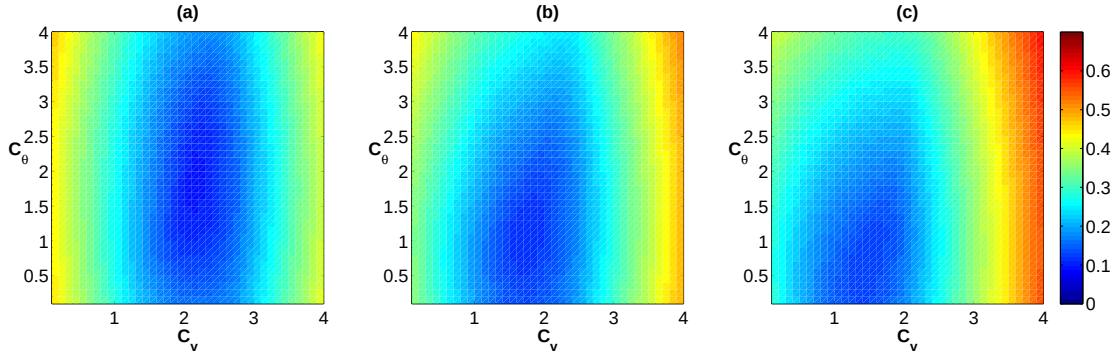

Figure 8.12: Influence of C_v and C_θ values on the total magnitude error between the results of DNS and model (ϵ_T) for cases with different Re at fixed $\theta_m = 10°$ and $\theta_0 = 20°$.
a) $C_{10c,1}$ [$Re = 3000$], b) B_{10c} [$Re = 1000$], c) A_{10c} [$Re = 500$].

Cases with $\theta_m = 10°$ and $\theta_0 = 0°$

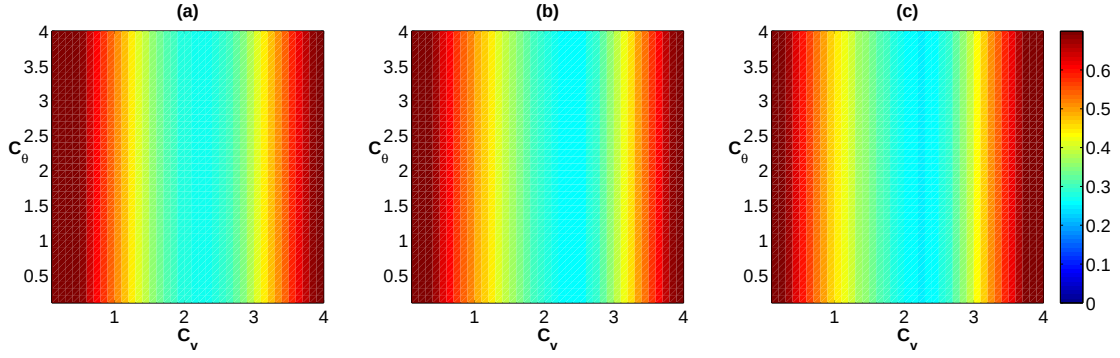

Figure 8.13: Influence of C_v and C_θ values on the total magnitude error between the results of DNS and model (ϵ_T) for cases with different Re at fixed $\theta_m = 10°$ and $\theta_0 = 0°$.
a) C_{10a} [$Re = 3000$], b) B_{10a} [$Re = 1000$], c) A_{10a} [$Re = 500$].

Cases with $\theta_m = 0°$ and $\theta_0 = 20°$

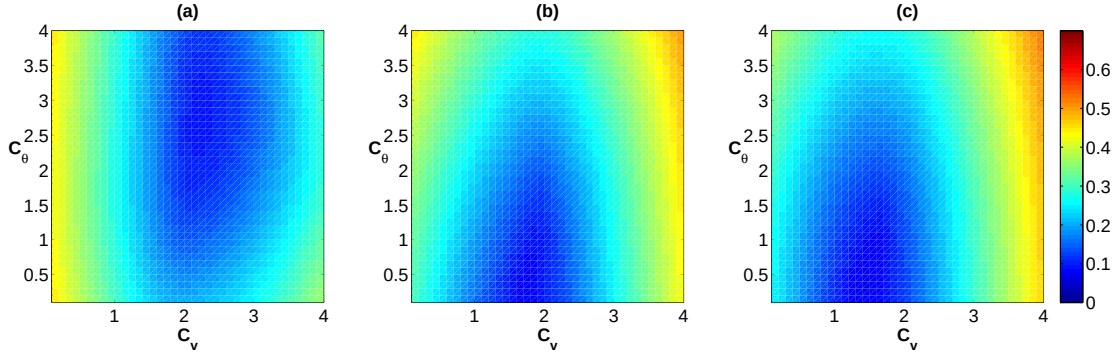

Figure 8.14: Influence of C_v and C_θ values on the total magnitude error between the results of DNS and model (ϵ_T) for cases with different Re at fixed $\theta_m = 0°$ and $\theta_0 = 20°$.
a) C_{00c} [$Re = 3000$], b) B_{00c} [$Re = 1000$], c) A_{00c} [$Re = 500$].

8.2.2 Influence of coefficients on error varying the pitching amplitude

Cases with $\theta_m = 0°$ and $Re = 1000$

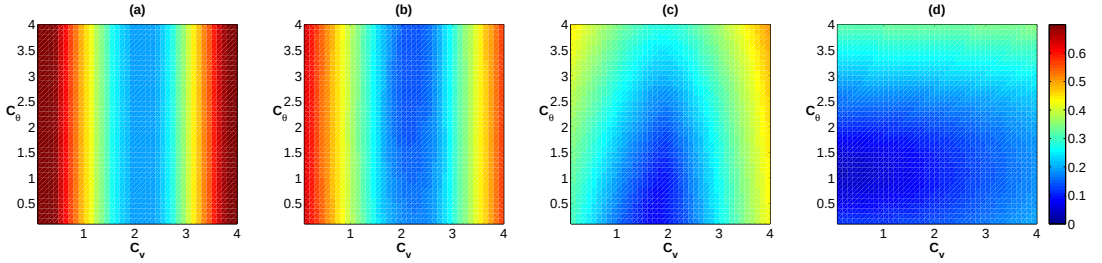

Figure 8.15: Influence of C_v and C_θ values on the total magnitude error between the results of DNS and model (ϵ_T) for cases with different θ_0 at fixed $Re = 1000$ and $\theta_m = 0°$.
a) B_{00a} [$\theta_0 = 0°$], b) B_{00b} [$\theta_0 = 10°$], c) B_{00c} [$\theta_0 = 20°$], d) B_{00d} [$\theta_0 = 30°$].

Cases with $\theta_m = 10°$ and $Re = 1000$

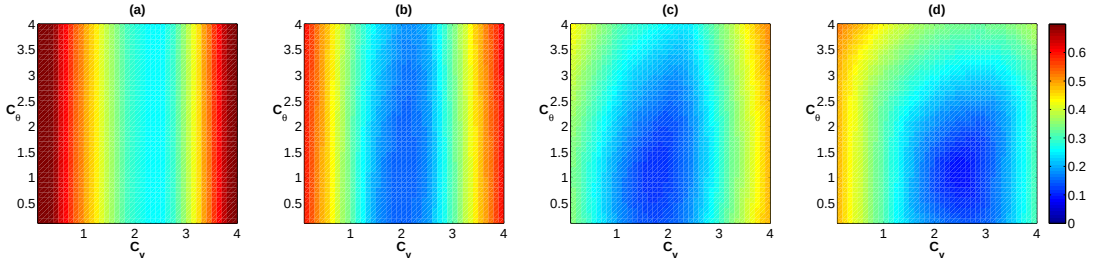

Figure 8.16: Influence of C_v and C_θ values on the total magnitude error between the results of DNS and model (ϵ_T) for cases with different θ_0 at fixed $Re = 1000$ and $\theta_m = 10°$.
a) B_{10a} [$\theta_0 = 0°$], b) B_{10b} [$\theta_0 = 10°$], c) B_{10c} [$\theta_0 = 20°$], d) B_{10d} [$\theta_0 = 30°$].

8.2.3 Comparison varying the Reynolds number

Cases with $\theta_m = 10°$ and $\theta_0 = 20°$

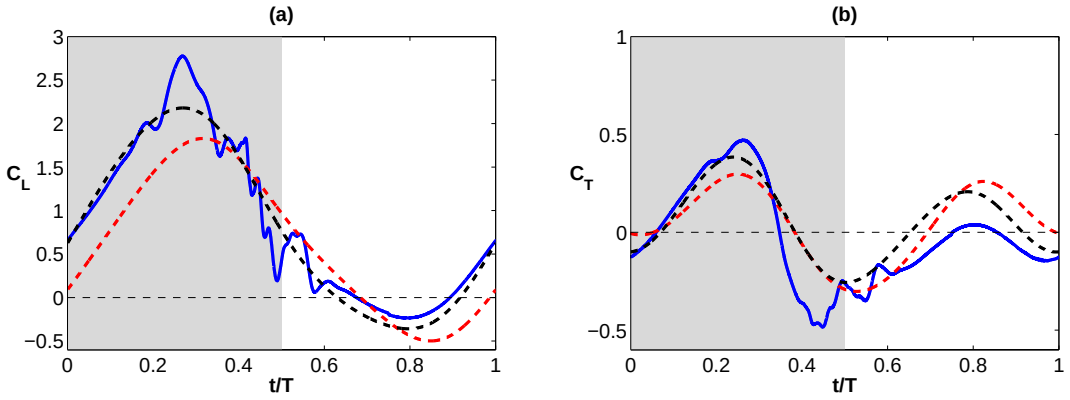

Figure 8.17: Results in one period of a) C_L b) C_T for case $C_{10c,1}$ [$Re = 3000$, $\theta_m = 10°$, $\theta_0 = 20°$]. — $\vec{F}_{DNS}$, - - - $\vec{F}_{mod}$, - - - $\vec{F}_{opt}$

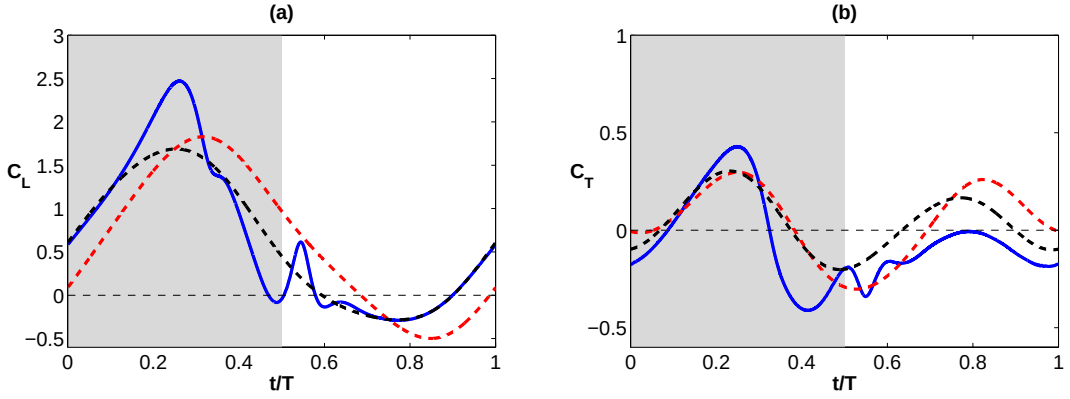

Figure 8.18: Results in one period of a) C_L b) C_T for case B_{10c} [$Re = 1000$, $\theta_m = 10°$, $\theta_0 = 20°$]. — $\vec{F}_{DNS}$, - - - $\vec{F}_{mod}$, - - - $\vec{F}_{opt}$

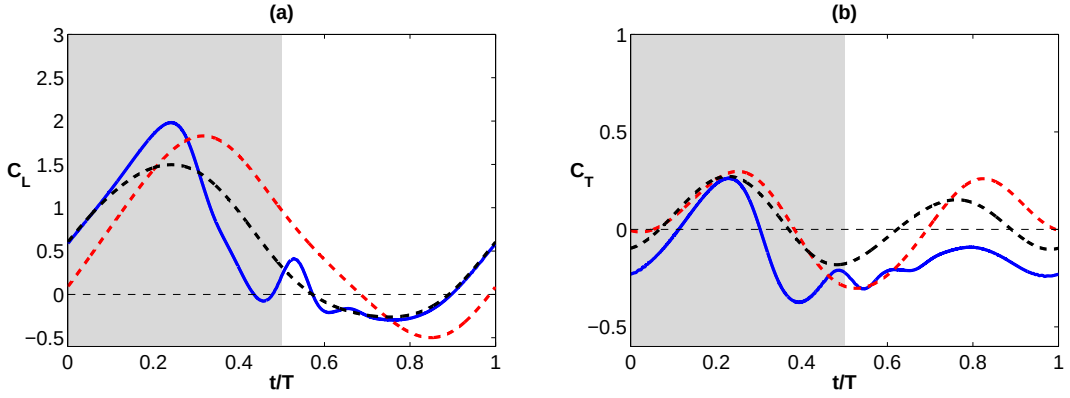

Figure 8.19: Results in one period of a) C_L b) C_T for case A_{10c} [$Re = 500$, $\theta_m = 10°$, $\theta_0 = 20°$]. — $\vec{F}_{DNS}$, - - - $\vec{F}_{mod}$, - - - $\vec{F}_{opt}$

Cases with $\theta_m = 10°$ and $\theta_0 = 0°$

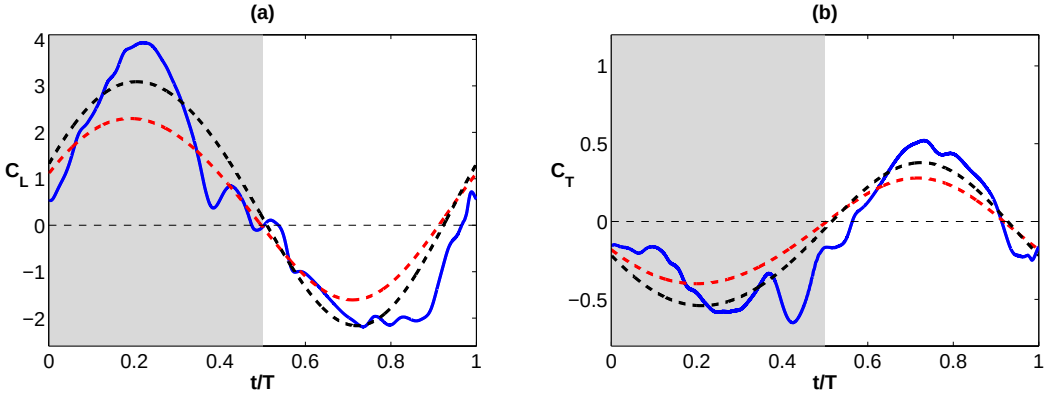

Figure 8.20: Results in one period of a) C_L b) C_T for case C_{10a} [$Re = 3000$, $\theta_m = 10°$, $\theta_0 = 0°$]. —— $\vec{F}_{DNS}$, - - - $\vec{F}_{mod}$, - - - $\vec{F}_{opt}$

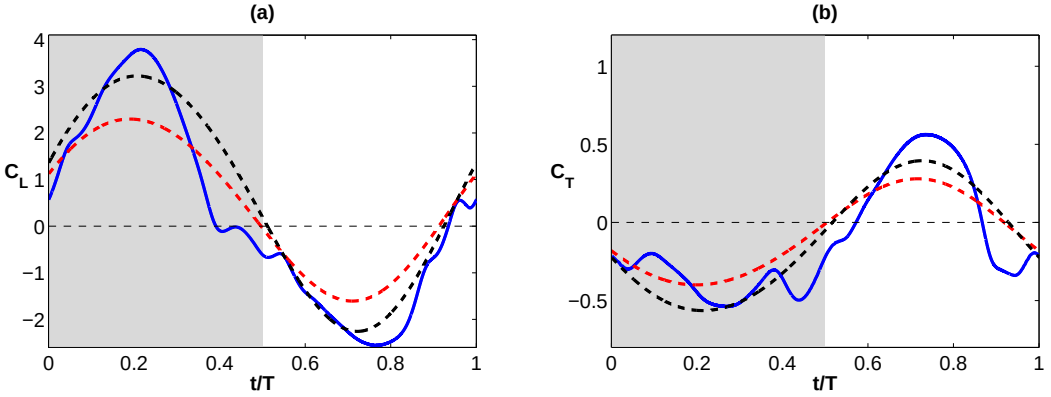

Figure 8.21: Results in one period of a) C_L b) C_T for case B_{10a} [$Re = 1000$, $\theta_m = 10°$, $\theta_0 = 0°$]. —— $\vec{F}_{DNS}$, - - - $\vec{F}_{mod}$, - - - $\vec{F}_{opt}$

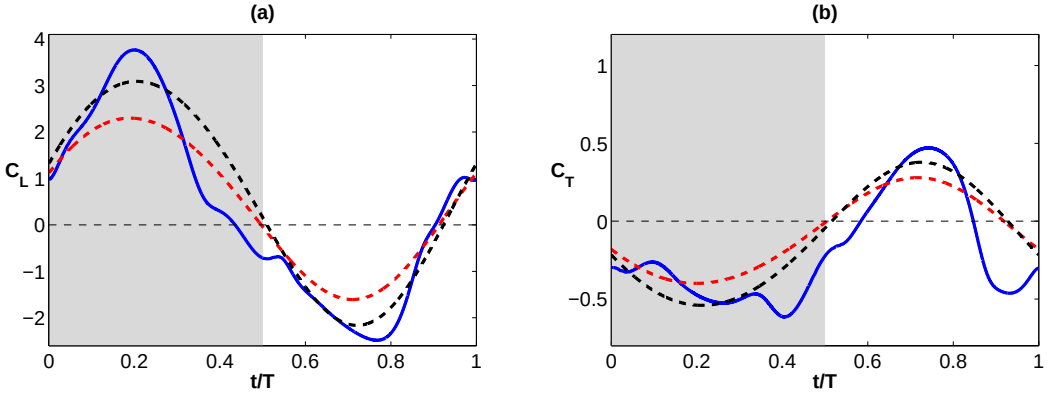

Figure 8.22: Results in one period of a) C_L b) C_T for case A_{10a} [$Re = 500$, $\theta_m = 10°$, $\theta_0 = 0°$]. —— $\vec{F}_{DNS}$, - - - $\vec{F}_{mod}$, - - - $\vec{F}_{opt}$

Cases with $\theta_m = 0°$ and $\theta_0 = 20°$

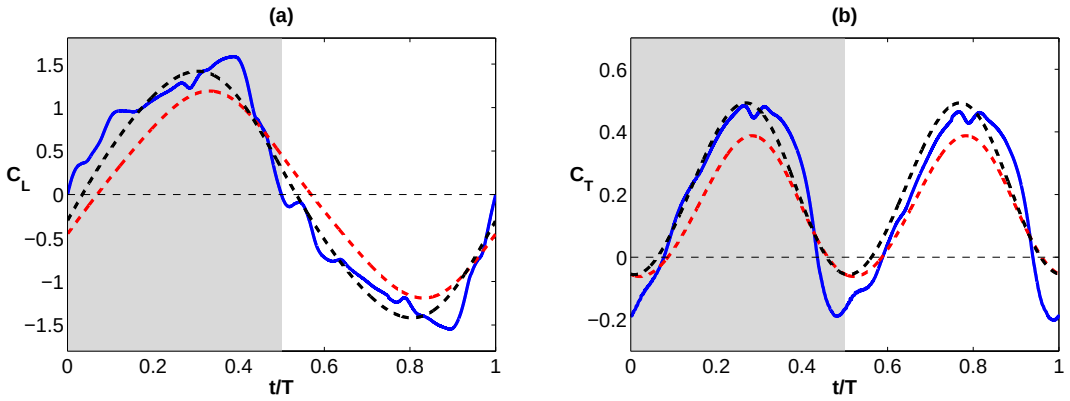

Figure 8.23: Results in one period of a) C_L b) C_T for case C_{00c} [$Re = 3000$, $\theta_m = 0°$, $\theta_0 = 20°$]. —— $\vec{F}_{DNS}$, - - - $\vec{F}_{mod}$, - - - $\vec{F}_{opt}$

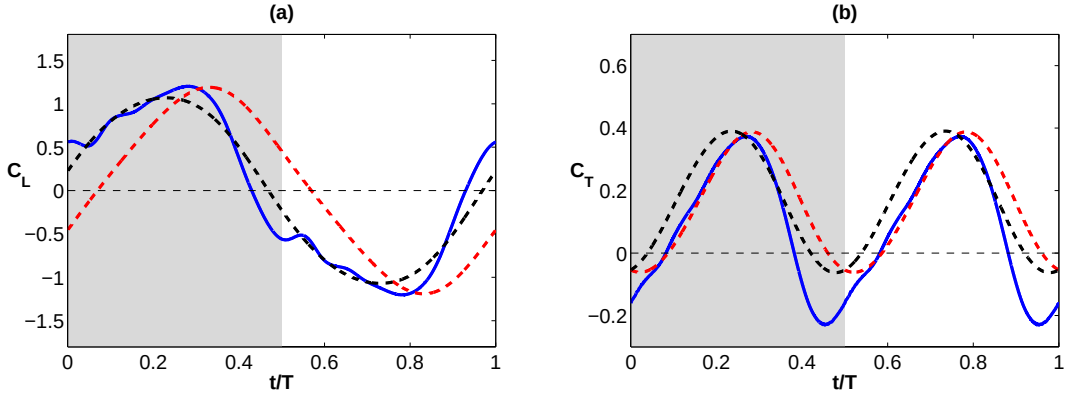

Figure 8.24: Results in one period of a) C_L b) C_T for case B_{00c} [$Re = 1000$, $\theta_m = 0°$, $\theta_0 = 20°$]. —— $\vec{F}_{DNS}$, - - - $\vec{F}_{mod}$, - - - $\vec{F}_{opt}$

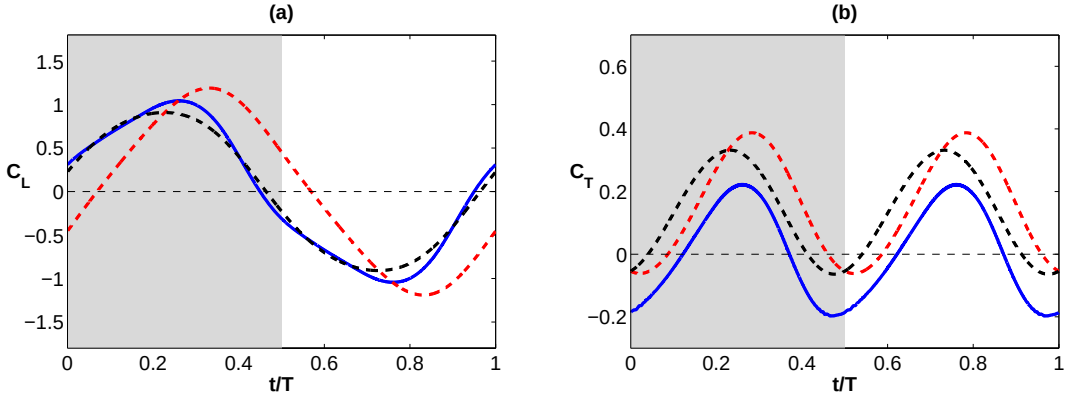

Figure 8.25: Results in one period of a) C_L b) C_T for case A_{00c} [$Re = 500$, $\theta_m = 0°$, $\theta_0 = 20°$]. —— $\vec{F}_{DNS}$, - - - $\vec{F}_{mod}$, - - - $\vec{F}_{opt}$

8.2.4 Comparison varying the pitching amplitude

Cases with $\theta_m = 0°$ and $Re = 1000$

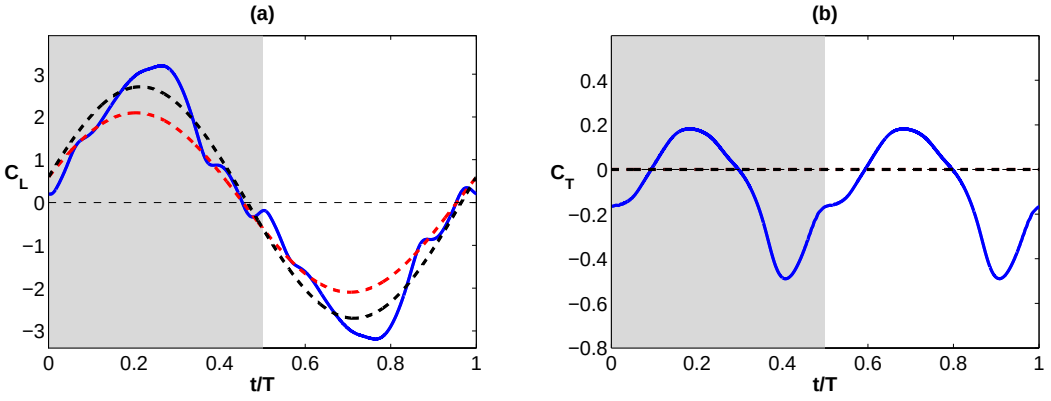

Figure 8.26: Results in one period of a) C_L b) C_T for case B_{00a} [$Re = 1000$, $\theta_m = 0°$, $\theta_0 = 0°$]. —— $\vec{F}_{DNS}$, - - - $\vec{F}_{mod}$, - - - $\vec{F}_{opt}$

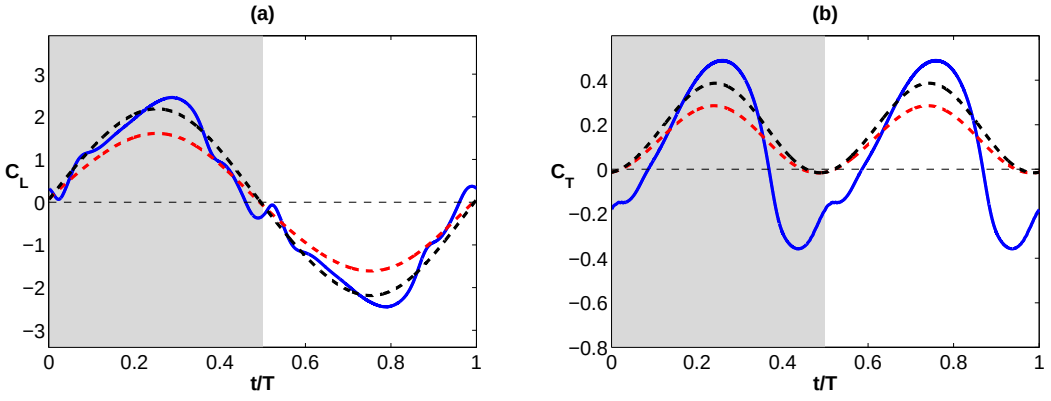

Figure 8.27: Results in one period of a) C_L b) C_T for case B_{00b} [$Re = 1000$, $\theta_m = 0°$, $\theta_0 = 10°$]. —— $\vec{F}_{DNS}$, - - - $\vec{F}_{mod}$, - - - $\vec{F}_{opt}$

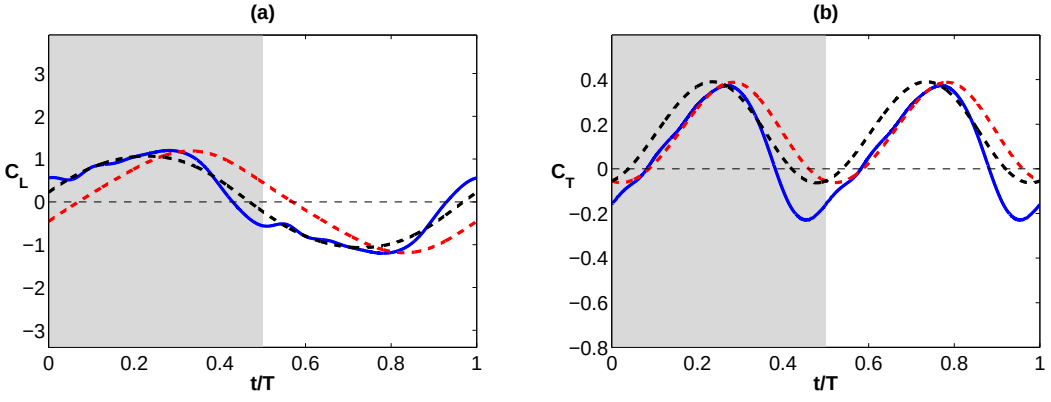

Figure 8.28: Results in one period of a) C_L b) C_T for case B_{00c} [$Re = 1000$, $\theta_m = 0°$, $\theta_0 = 20°$]. —— $\vec{F}_{DNS}$, - - - $\vec{F}_{mod}$, - - - $\vec{F}_{opt}$

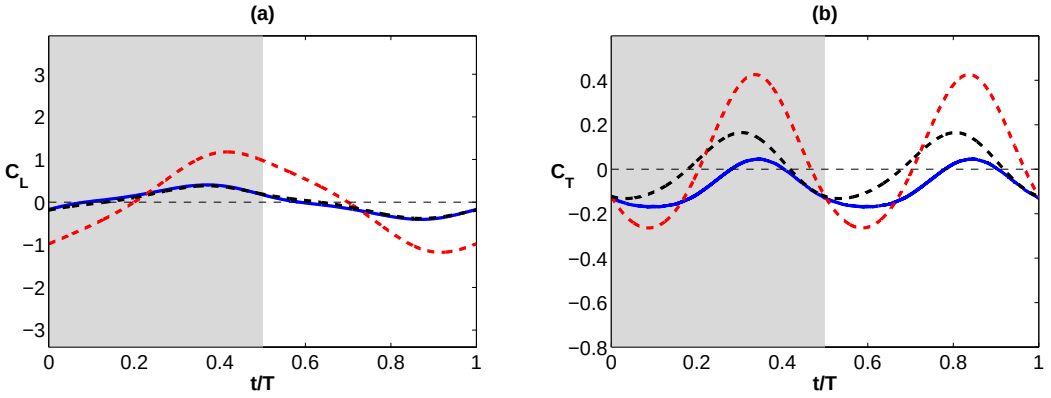

Figure 8.29: Results in one period of a) C_L b) C_T for case B_{00d} [$Re = 1000$, $\theta_m = 0°$, $\theta_0 = 30°$]. —— $\vec{F}_{DNS}$, - - - $\vec{F}_{mod}$, - - - $\vec{F}_{opt}$

Cases with $\theta_m = 10°$ and $Re = 1000$

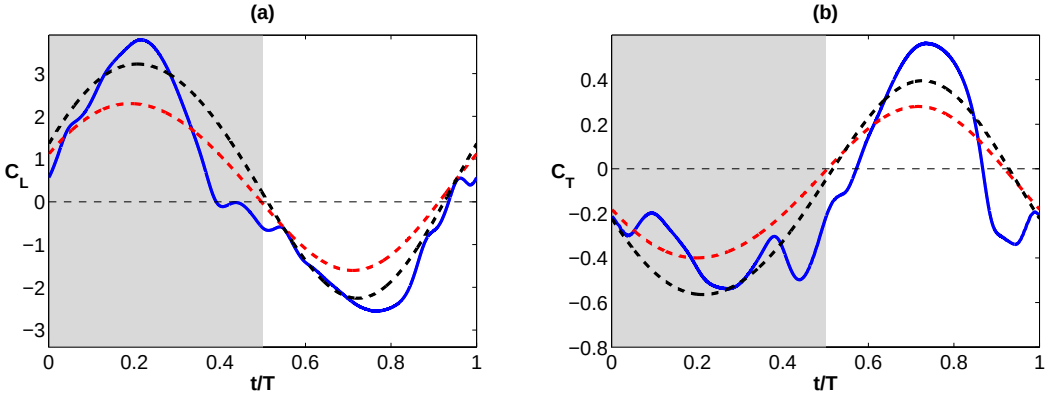

Figure 8.30: Results in one period of a) C_L b) C_T for case B_{10a} [$Re = 1000$, $\theta_m = 10°$, $\theta_0 = 0°$]. —— $\vec{F}_{DNS}$, - - - $\vec{F}_{mod}$, - - - $\vec{F}_{opt}$

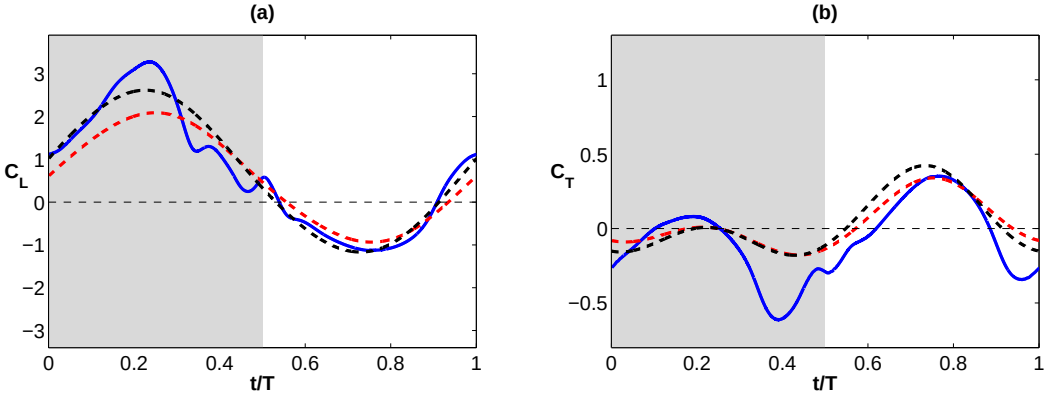

Figure 8.31: Results in one period of a) C_L b) C_T for case B_{10b} [$Re = 1000$, $\theta_m = 10°$, $\theta_0 = 10°$]. —— $\vec{F}_{DNS}$, - - - $\vec{F}_{mod}$, - - - $\vec{F}_{opt}$

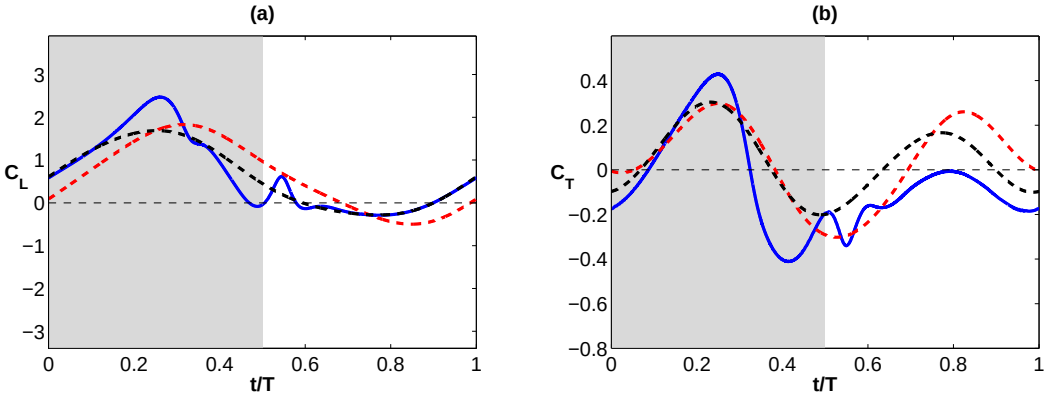

Figure 8.32: Results in one period of a) C_L b) C_T for case B_{10c} [$Re = 1000$, $\theta_m = 10°$, $\theta_0 = 20°$]. —— $\vec{F}_{DNS}$, - - - $\vec{F}_{mod}$, - - - $\vec{F}_{opt}$

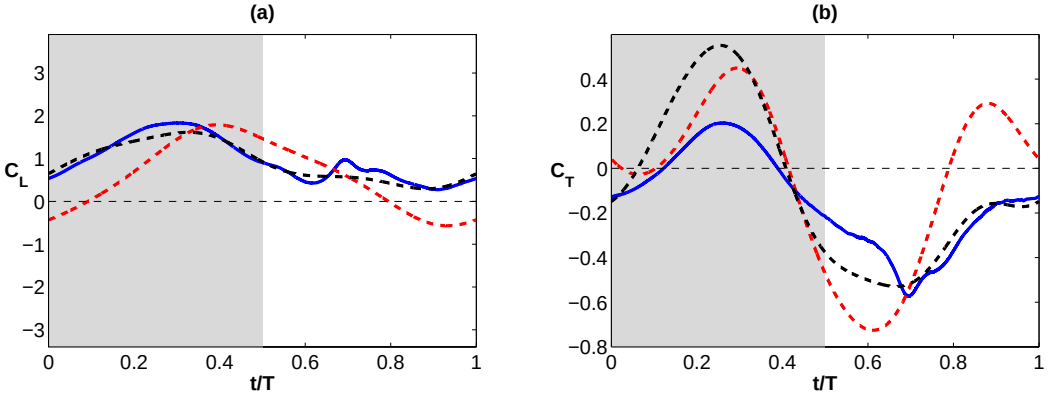

Figure 8.33: Results in one period of a) C_L b) C_T for case B_{10d} [$Re = 1000$, $\theta_m = 10°$, $\theta_0 = 30°$]. —— $\vec{F}_{DNS}$, - - - $\vec{F}_{mod}$, - - - $\vec{F}_{opt}$

Bibliography

[Anderson et al., 1998] Anderson, J. M., Stritlien, K., Barrett, D. S., and Triantafyllou, M. (1998). Oscillating foils of high propulsive efficiency. *Journal of Fluid Mechanics*, 360:41–72.

[Ashraf et al., 2011] Ashraf, M. A., Young, J., and Lai, J. C. S. (2011). Reynolds number, thickness and camber effects on flapping airfoil propulsion. *Journal of Fluids and Structures*, 27(2):145–160.

[Brown et al., 2001] Brown, D. L., Cortez, R., and Minion, M. L. (2001). Accurate projection methods for the incompressible navier–stokes equations. *Journal of Computational Physics*, 168(2):464–499.

[CESGA] CESGA. Cesga - Horas de Cálculo. https://www.cesga.es/es/servicios/computacion/horas-calculo#Tarifas. Accessed: 2016-06-18.

[Ellington et al., 1996] Ellington, C., Van Den Berg, C., Willmott, A. P., and Thomas, A. L. R. (1996). Leading-edge vortices in insect flight.

[Fenercioglu and Cetiner, 2012] Fenercioglu, I. and Cetiner, O. (2012). Categorization of flow structures around a pitching and plunging airfoil. *Journal of Fluids and Structures*, 31:92–102.

[Ford and Babinsky, 2013] Ford, C. W. P. and Babinsky, H. (2013). Lift and the leading-edge vortex. *Journal of Fluid Mechanics*, 720:280–313.

[Freymuth, 1988] Freymuth, P. (1988). Propulsive vortical signature of plunging and pitching airfoils. *AIAA Journal*, 26(7):881–883.

[Gonzalo, 2016] Gonzalo, A. (2016). Private communication.

[Heathcote et al., 2008] Heathcote, S., Wang, Z., and Gursul, I. (2008). Effect of spanwise flexibility on flapping wing propulsion. *Journal of Fluids and Structures*, 24(2):183–199.

[Isogai et al., 1999] Isogai, K., Shinmoto, Y., and Watanabe, Y. (1999). Effects of dynamic stall on propulsive efficiency and thrust of flapping airfoil. *AIAA Journal*, 37(10):1145–1151.

[Koochesfahani, 1989] Koochesfahani, M. M. (1989). Vortical patterns in the wake of an oscillating airfoil. *AIAA Journal*, 27(9):1200–1205.

[Lai and Platzer, 1999] Lai, J. C. S. and Platzer, M. F. (1999). Jet characteristics of a plunging airfoil. *AIAA Journal*, 37(12):1529–1537.

[Lewin and Haj-Hariri, 2003] Lewin, G. C. and Haj-Hariri, H. (2003). Modelling thrust generation of a two-dimensional heaving airfoil in a viscous flow. *Journal of Fluid Mechanics*, 492:339–362.

[Lua et al., 2007] Lua, K. B., Lim, T. T., Yeo, K. S., and Oo, G. Y. (2007). Wake-structure formation of a heaving two-dimensional elliptic airfoil. *AIAA Journal*, 45(7):1571–1583.

[Martín-Alcántara et al., 2015] Martín-Alcántara, A., Fernandez-Feria, R., and Sanmiguel-Rojas, E. (2015). Vortex flow structures and interactions for the optimum thrust efficiency of a heaving airfoil at different mean angles of attack. *Physics of Fluids*, 27(7):073602.

[MATLAB] MATLAB. Pricing and Licensing - MathWorks España. http://es.mathworks.com/pricing-licensing/index.html?intendeduse=edu&prodcode=ML. Accessed: 2016-06-18.

[Miao and Ho, 2006] Miao, J. M. and Ho, M. H. (2006). Effect of flexure on aerodynamic propulsive efficiency of flapping flexible airfoil. *Journal of Fluids and Structures*, 22(3):401–419.

[Moriche, 2016] Moriche, M. (2016). Private communication.

[Moriche et al., 2016] Moriche, M., Flores, O., and García-Villalba, M. (2016). On the aerodynamic forces on heaving and pitching airfoils at low reynolds number. (In preparation).

[Pesavento and Wang, 2004] Pesavento, U. and Wang, Z. J. (2004). Falling paper: Navier-stokes solutions, model of fluid forces, and center of mass elevation. *Physical Review Letters*, 93(14):144501.

[Roma et al., 1999] Roma, A. M., Peskin, C. S., and Berger, M. J. (1999). An adaptive version of the immersed boundary method. *Journal of Computational Physics*, 153(2):509–534.

[Sane and Dickinson, 2002] Sane, S. P. and Dickinson, M. H. (2002). The aerodynamic effects of wing rotation and a revised quasi-steady model of flapping flight. *Journal of Experimental Biology*, 205(8):1087–1096.

[Sedov et al., 1965] Sedov, L. I., Chu, C. K., Cohen, H., Seckler, B., and Gillis, J. (1965). Two-dimensional problems in hydrodynamics and aerodynamics. *Physics Today*, 18:62.

[Uhlmann, 2005] Uhlmann, M. (2005). An immersed boundary method with direct forcing for the simulation of particulate flows. *Journal of Computational Physics*, 209(2):448–476.

[Walker et al., 1985] Walker, J., Helin, H., and Chou, D. (1985). Unsteady surface pressure measurements on a pitching airfoil. Technical report, DTIC Document.

[Wang, 2000] Wang, Z. J. (2000). Vortex shedding and frequency selection in flapping flight. *Journal of Fluid Mechanics*, 410:323–341.

[Widmann and Tropea, 2015] Widmann, A. and Tropea, C. (2015). Parameters influencing vortex growth and detachment on unsteady aerodynamic profiles. *Journal of Fluid Mechanics*, 773:432–459.

[Young and Lai, 2004] Young, J. and Lai, J. C. S. (2004). Oscillation frequency and amplitude effects on the wake of a plunging airfoil. *AIAA Journal*, 42(10):2042–2052.